Development of novel image-based computational and artificial intelligence (AI) technologies for real time monitoring and event detection during *in vitro* dissolution testing

by

Alexandra Rumenova Taseva

Being a thesis submitted for the degree of

Doctor of Philosophy in Pharmaceutics

At

Trinity College Dublin, the University of Dublin

Under the supervision and direction of

Deirdre D'Arcy, Assoc. Prof, M. Pharm., Ph.D., M.P.S.I

and

Tim Persoons, Assoc. Prof M. Eng, Ph.D.

2025

Declaration

I declare that this thesis has not been submitted as an exercise for a degree at this or any other university and it is entirely my own work.

I agree to deposit this thesis in the University's open access institutional repository or allow the Library to do so on my behalf, subject to Irish Copyright Legislation and Trinity College Library conditions of use and acknowledgement.

I consent to the examiner retaining a copy of the thesis beyond the examining period, should they so wish.

X

Alexandra Rumenova Taseva

Covid-19 impact statement

Due to the Covid-19 pandemic, the work was delayed and spans a 4.5-year timeframe. The restricted access to laboratories influenced the accusation of lab work. During this period (March 2020 to September 2020), some literature research and computational work was carried out. Shutdown mostly interrupted planned training, as it occurred at the beginning of the project, delaying the start of laboratory data generation for the project. However, the impact of this disruption on results and interpretation was minimised through planning.

Summary

To ensure safe and effective medications, in recent years the ever-evolving pharmaceutical industry started to transform and to adopt novel technologies for continuous manufacturing, real time monitoring and quality control. From a development perspective, *in vitro* dissolution testing remains a vital drug-performance test used to predict *in vivo* outcome. Strategies such as *in silico* simulations and animal models have been researched and applied in multiple situations and discussed broadly in the literature and were found suitable for early-stage drug development. However, despite such promising results, their applicability for continuous manufacturing and process monitoring remains unknown.

On the other hand, advances of imaging technologies like development of micro-lens systems and non-invasive imaging methods allow the implementation of such systems in routine manufacturing. They have been used as monitoring tools to ensure robust processing and medicinal products of high quality. The studies in this thesis were focused on development and application of image-based analysis techniques to be used with standard dissolution apparatuses. The primary focus was on a non-invasive imaging method for shadowgraph and direct imaging in the flow-through apparatus and some preliminary studies conducted using a commercially available imaging system in an alternative set-up (paddle apparatus). Two imaging approaches were used with the non-invasive system – a) shadowgraph imaging to characterise particulate behaviour in the images, and b) analysis of a whole frame using AI classification methods to characterise the dissolution process. Phenomena such as drug precipitation and agglomeration were observed and used for further analysis.

A weakly acidic (pKa = 4.5) drug, ibuprofen, was used as a model drug to perform dissolution testing by variation of the sample mass and crystal habit of the drug powder. In the last part of this project, two brands of commercially available ibuprofen-containing suspension formulations were used for dissolution in the flow-through apparatus. Imaging and image analysis were used to capture differences in the dissolution rate, particle motion and suspension behaviour during testing.

Imaging systems' ability to detect deviations in the dissolution rate caused by changes in the environment such as addition of surfactant, change in the flow rate/paddle rotation speed, occurrence of drug precipitation, and the effect of excipients in the formulation, as well as changes related to the drug crystal habit and sample mass used for dissolution were tested.

The work of D'Arcy and Persoons[1], [2] on image analysis based on in-house written code for shadowgraph imaging was expanded to investigate particle behaviour of sieved and un-sieved particles with needle- and plate-like shapes and their agglomeration tendency. Agglomerates could have a negative impact on product stability, resulting in inaccurate dosing of formulations, *e.g.*, oral, or parenteral suspensions. Such unfortunate events could require a recall of the drug product from the market and a withdrawal of the registration approval. As a proof-of-concept and by using the outputs of the image analysis, an automated agglomeration identification method was created. Such method showed potential to be further developed and utilized as an in-line quality control tool as it was able to accurately capture agglomerates formed during dissolution testing.

With the emergence of artificial intelligence (AI) smart monitoring of production lines could become a standard procedure. The United States Food and Drug Administration (FDA) recognizes the potential to apply AI in many areas of the pharmaceutical industry – from compound screening, through non-clinical and clinical research, to post-approval monitoring.[3] In this present work, an AI model for image analysis created and exploited for tablet surface defect detection was adapted for events detection in a dynamic environment, *i.e.*, dissolution and precipitation processes. The method was successfully developed to provide quantitative and qualitative information that contributes to the general understanding of process and compound changes, which may affect the dissolution process. A recommended apparatus for dissolution testing of oral suspensions is the paddle apparatus[4], [5]. Although dissolution testing in the flow-through apparatus showed a much slower dissolution rate compared to the recommended dissolution time in the paddle apparatus, the obtained results provided good discrimination between the two brands of suspensions. The image analysis of the dissolution tests identified differences in

sample dispersal during testing which impacted on the dissolution profile. The analysis also showed notable differences in the suspensions' dissolution behaviour, which could suggest different hydrophilicity or polarity of the excipients used in the formulation, or their impact on the balance between cohesion and adhesion between the formulation and the test vessel. Specific dissolution patterns were observed from each formulation. These product specifics could contribute towards the development of an AI tool able to distinguish between process and content changes, to assure batch-to-batch consistency in routine quality control, or even to participate in biowaiver decision-making by providing high discrimination power and formulation related insights.

All imaging and analysis approaches presented in this thesis provided additional insight into the dissolution process and drug behaviour, which could contribute to the general knowledge in the field. The imaging systems showed to be suitable to be used in combination with standard apparatuses in real time or for an offline image analysis. The shadowgraph imaging agglomerate identification method built during this project showed a potential to be further developed to recognize objects of interest. The AI-based classification model was useful to provide qualitative information by using the pre-trained settings. However, understanding of the AI process and opening the "black box" allowed further exploration of the system and the development of a quantitative classification method able to better describe the dissolution process. Thus, it could be suggested that there is unrealized AI potential remaining to be explored in the future.

Table of contents

Acknowledgements

Completing a PhD is a challenging journey. Even more challenging when you decide to do it in a foreign country and in the middle of a world pandemic. Covid-19 marked the first two years of my journey and left me struggling away from home and the people I love. Meeting new people was hardly possible due to the social distancing. Workflow was highly disturbed, and I missed a big part of the PhD social life in Trinity, which I deeply regret. The “great” Irish weather did not help either about how I was feeling here. However, I believe these obstacles only made me stronger and the pleasure of finishing my PhD is even bigger.

I would like to thank my supervisors Prof. Deirdre D’Arcy and Prof. Tim Persoons for their guidance, patience, and support over these years. Especially during my most difficult moments when I was complaining a lot and about everything. I would like to thank the first person who helped me here and gave me a nice and safe place to live - my landlord John Lovatt for his kindness and who was always there to cheer me up with a funny story or a cup of tea. I would like to thank my PhD fellows, all visiting researchers and Erasmus students who crossed my way in the last 4 years for making my stay in college much better, for all the nights out, laughs and shared moments. A big thank you to Jay Jadav for preparing the ibuprofen crystals used in some of my studies, which resulted in two poster presentations and a future publication, and J.M. Canty and Ciaran who provided the Canty™ imaging system and trained me how to use it. I would also thank my thesis committee - Prof. Anne-Marie Healy and Prof. Lidia Tajber, along with Prof. Carsten Ehrhardt for their guidance, support, and mentoring through the years. I would like to acknowledge all other professors, lab and administrative staff for all hours which we spent together during demonstrations and other events – it was a pleasure to work with you all.

I would like to acknowledge Trinity’s Provost, Science Foundation Ireland (SFI) and the SFI Research Centre for Pharmaceuticals (SSPC), for providing the financial support which was essential to complete this project and for all opportunities to present my work and develop myself. I would also like to acknowledge my colleagues and mentors from FD department in Alkermes – Cathy, Kris, Zelalem, Beatrice, Fiona, Vamsi and

Renato for the time and the knowledge they shared with me during my industrial placement. A special thank you to my friend Emanuele, who was supporting me through these years and even more during the writing of this thesis.

Nevertheless, I want to thank my family. My mom for the support and all the efforts to travel during the pandemic to visit me. My best friends - Maria and Niki who always belied in me and who were there for me even in the darkest of times. To my friends and mentors in Bulgaria and abroad – thank you kindly for everything you have done for me, for your wisdom, support, for all extensive phone calls and amazing trips and collaborations. A special thank you to Khaleesi and my partner Cass for making sure I will sit down and finish this thesis (on time), for their kindness, warmth, love, and support. I am lucky to have all of you in my life.

I would like to finish my acknowledgments with one favourite quote – “now, Dobby is a free elf”.

Thank you!

Publications associated with this thesis

Publications:

- Taseva A.R., Persoons T., D'Arcy D.M. (2023) Application of an AI image analysis and classification approach to characterise dissolution and precipitation events in the flow through apparatus. Eur J Pharm Biopharm. 2023 Aug; 189:36-47. doi: 10.1016/j.ejpb.2023.04.020
- Taseva, A., Persoons, T. & D'Arcy, D. M., (2022) "Challenges and considerations of automated agglomeration detection method development with image analysis in dissolution testing", *British Journal of Pharmacy* 7(2). doi: https://doi.org/10.5920/bjpharm.1139
- The results, discussion, and conclusion of Chapter 3 of this thesis, along with relevant methods and introductory information, were submitted for publication in the International Journal of Pharmaceutics (IJP).
- The results, discussion, and conclusion of Chapter 5 of this thesis, along with relevant methods and introductory information, have being prepared for publication with the intention to submit to Pharmaceutical Research Journal.

Posters and oral presentations:

- Taseva A.R., Persoons T., D'Arcy D.M. Investigation of optimal conditions for the implementation of Shadowgraph imaging (SGI) as a real-time monitoring tool in dissolution testing (poster) *in the* European Federation for Pharmaceutical Sciences (EUFEPS) Annual Meeting, Virtual meeting, June 7th - 9th, 2021.
- Taseva A.R., Persoons T., Yadav J., Healy A.M., D'Arcy D.M. Dissolution of different crystal habits of an API powder using shadowgraph imaging as a real time monitoring tool (poster) *in the* American Association of Pharmaceutical Sciences (AAPS) PharmSci 360 meeting, Virtual meeting, October 17th - 20th, 2021.

- Taseva A.R., Persoons T., D'Arcy D.M. Challenges and considerations of automated agglomeration detection method development with image analysis in dissolution testing (poster) *in the* Academy of Pharmaceutical Sciences (APS) PharmSci Conference, Belfast, United Kingdom, September 7th - 9th, 2022.
- Taseva A.R., Persoons T., Healy A.M., D'Arcy D.M. Automated online agglomeration detection using shadowgraph imaging analysis during dissolution testing of ibuprofen powder in USP 4 flow-through apparatus *in the* AAPS PharmSci 360 meeting, Boston, USA, October 16th - 19th, 2022.
- Taseva A.R., Persoons T., Healy A.M., D'Arcy D.M. An AI and imaging approach for improved insight into paediatric oral suspension dissolution behaviour in the flow-through apparatus (FTA) (poster, oral presentation, and Award for young scientist) *in the* 15th Annual EuPFI Conference 2023, Glasgow, United Kingdom, September 19th – 21st, 2023
- Taseva A.R., Persoons T., Healy A.M., D'Arcy D.M. Investigation of pH dependent drug precipitation and crystal growth in the paddle apparatus by in-situ micro-imaging (abstract) *in the* DRPI competition 2024, Virtual meeting, September, 2024.

List of Figures

Chapter 1:

Chapter 2:

Chapter 3:

Chapter 4:

Chapter 5:

Chapter 6:

Appendix 1:

Appendix 2:

Abbreviations

%avgATS – percent average anomaly threshold score

%FwA – percent frames without anomalies

AI – artificial intelligence

AIM – agglomeration identification method

ANN – artificial neural network

API – active pharmaceutical ingredient

ATS - anomaly threshold score

avgATSmax – maximum average anomaly threshold score

avgATSn – average anomaly threshold score per dissolution time point

B100 – Brupro commercially available ibuprofen oral suspension, dose 100 mg in 5 mL

B200 – Brupro commercially available ibuprofen oral suspension, dose 200 mg in 5 mL

BCS - Biopharmaceutics classification system

cATS – calibration anomaly threshold score

CCM – cooling crystallization method

CE1 – a Sotax flow-through apparatus with a single cell

CE7 – a Sotax flow-through apparatus with seven cells

CNN – convolutional neural network

CVIA – CANTYVISION intelligent analysis software

DCS – Developability classification system

DL – deep learning

Dp – particle diameter distribution

Dv50 – particle size volume distribution under 50%

Dv90 - particle size volume distribution under 90%

EMA – European medicines agency

Eur. Ph. – European pharmacopoeia

FBRM – Focused beam reflectance measurement

FDA – Food and Drug Administration

FR – flow rate

Fps – frames per second

FTA – flow-through dissolution apparatus

FTIR - Fourier-transform infrared

GI – gastrointestinal

HCl – hydrochloric acid

HPLC – high performance liquid chromatography

HPMC – hydroxypropyl methylcellulose

ICH - International council for harmonisation of technical requirements for pharmaceuticals for human use

Ibu-nd – ibuprofen needle-shaped crystals un-sieved (as received)

Ibu-nd-S – ibuprofen needle-shaped crystals sieved fraction

Ibu-pl – ibuprofen plate-shaped crystals un-sieved

Ibu-pl-S – ibuprofen plate-shaped crystals sieved fraction

MLP – multilayer perceptron

NIR – near infra-red

LED – light-emitting diode

LOD – limit of detection

LOQ – limit of quantification

ML – machine learning

MRI – magnetic resonance imaging

N100 – Nurofen commercially available ibuprofen oral suspension, dose 100 mg in 5 mL

N200 – Nurofen commercially available ibuprofen oral suspension, dose 200 mg in 5 mL

NIR – near infrared

NN – neural network

Npd – number of particle detections

PAT – process analytical technology

PB – phosphate buffer

PBPK – physiologically based pharmacokinetics

Pr – percentile

QbD – quality by design

RNN – recurrent neural network

SGI – shadowgraph imaging

TPI – terahertz pulsed imaging

USP – United States pharmacopoeia

VGG-16 - visual geometry group 16 network

Chapter 1: Introduction

Some of the parts presented in Chapter 1 were presented in: 1) Taseva A.R., Persoons T., D'Arcy D.M. Application of an AI image analysis and classification approach to characterise dissolution and precipitation events in the flow through apparatus. Eur J Pharm Biopharm. 2023 Aug; 189:36-47. doi: 10.1016/j.ejpb.2023.04.020. Epub 2023 Apr 27. PMID: 37120067 and 2) Taseva A.R., Persoons T, Healy AM, D'Arcy D.M. Application of shadowgraph imaging (SGI) particle characterisation data to interpret the impact of varying test conditions on powder dissolution and to develop an automated agglomeration identification method (AIM) in the USP flow-through apparatus. Int J Pharm. 2024 Dec 5; 666:124778. doi: https://doi.org/10.1016/j.ijpharm.2024.124778. Epub 2024 Sep 28. PMID: 39349225.

1.1. Dissolution

1.1.1. Dissolution as a process

To guarantee drug product safety and efficacy, pharmaceutical companies are trying to develop optimal new drugs and drug formulations. To support successful oral drug development and post-approval monitoring, along with generic drug development, *in vitro* dissolution testing has become a preferred method for assessment of potential new molecules and formulations, and further quality control. Dissolution could be defined as a process in which a certain quantity of an active pharmaceutical ingredient (API) forms a solution in a specified time. Dissolution testing is an important quality control tool, and it plays a vital role in several stages of pharmaceutical manufacturing. During the early-stage drug development, dissolution testing is used for the evaluation of physicochemical properties of target molecules and to determine the most suitable form for further formulation development.[6] It could be used to guide the toxicology and pre-clinical formulation assessment in animals and humans as well as a biowaiver

in a bioequivalence study, to demonstrate similarity between formulations and as a basis for selecting appropriate batches for an *in vivo* study.[7] During late-stage product development, dissolution testing could be used to evaluate product performance, elucidate the drug release mechanism, ensure the safe release of the drug from the formulation, or as an indicator for the stability of the formulation and the robustness of the manufacturing process.[8]–[14] Dissolution profiles can guide the choice of formulation when dealing with poorly soluble drugs, where solubility- and dissolution-limited absorption phenomena can be observed. Dissolution could be used to predict product release and behaviour *in vivo*, if a direct correlation could be made.[15], [16] To improve the predictions of *in vivo* drug behaviour, the *in vitro* dissolution methods have to reflect the gastrointestinal (GI) environment as closely as possible. Therefore, physiologically based dissolution media such as fasted state and fed state simulated intestinal fluids have been proposed.[17]–[19] Despite media complexity, high price and the inconvenience to be freshly prepared on the day of the dissolution test, they are well established in many dissolution laboratories. Attempts have been made to develop simplified biorelevant media which are easier to make and stable for longer without compromising the predictability of the *in vivo* performance.[20] To face some of the limitations of the traditional dissolution testing in large volumes (*e.g.*, 900 mL), especially in early-stage development when the available amount of test material is scarce, for low dose products, or due to lack of analytical sensitivity, the dissolution test should ideally mimic the GI environment as well as the physiological volumes.[21], [22] Thus, the development of small-volume dissolution which requires smaller sample size and smaller medium volumes become necessary to overcome these problems.[23], [24]

1.1.2. Brief history of the dissolution testing

According to Siepmann[25], drug dissolution performs characterization through 5 physical phenomena – 1) wetting of the surface, 2) breaking down of the solid state bonds inside the drug particle, 3) solvation of single drug molecules, atoms or ions, 4)

diffusion from the particle surface, through the boundary layer (a layer of high drug concentration formed around the particle) to the bulk fluid and 5) homogenization of the solution if the bulk fluid is well stirred. Back in 1897, Noyes-Whitney[26] explained the dissolution rate and pointed out the importance of the layer of saturated solution around the drug particle to the dissolution rate. Their equation (Equation 1.1) describes the dissolution rate (*dC/dt*, kg m^{-3} s^{-1}) of a perfect sphere as the change in the concentration of the dissolved drug in time and considering the dissolution constant (k). Thus, dissolution of drug from a solid-state formulation would depend on two consecutive steps – liberation of the drug from the matrix (disintegration) and drug dissolution in the medium according to Noyes-Whitney equation (Equation 1.1). The dissolution rate would depend on whichever is the slower of these two steps.[14]

Equation 1.1: Noyes-Whitney equation

$$\frac{dC}{dt} = k * (Css - Cx)$$

Later, in 1904 Nernst and Brunner investigated the relation between the dissolution constant and the diffusion coefficient of the solute based on the Noyes-Whitney equation (Equation 1.1) and Fick's laws of diffusion.[25] In the 1930s steps were made towards *in vitro-in vivo correlation*, bioavailability studies and explaining the role of the surface area on the dissolution rate.[27] The interest in modified release formulations and coated tablets grew in the 1960s when Higuchi[28] first published his mathematical model and simulation of drug release process called "*Rate of release of solid drugs dispersed in solid matrices*". Therefore, it was found that controlled-release delivery systems are affected by phenomena such as water penetration into the system, polymer swelling, the drug diffusion through the polymeric matrix and the dissolution process.[29], [30]

After the dissolution test was established as an important tool in the process of drug development, in the 1960s, the rotating basket was developed by Pernarowski and the "paddle method" – by Poole in accordance with the Food and Drug

Administration (FDA) requirements for drug testing.[27] The circulating flow-through cell was developed in Europe shortly after the introduction of the basket and paddle methods in the United States Pharmacopoeia (USP).[27] Between the 1970s and the 1990s the number of monographs in the USP and the European pharmacopoeia (Eur. Ph.) relating to the dissolution testing increased. More dissolution methods for transdermal and extended-release formulations were introduced. This forced the International council for harmonisation of technical requirements for pharmaceuticals for human use (ICH) to harmonize the methods and requirements of the largest pharmacopoeias (USP, Eur. Ph. and Japanese Ph.) in the early 2000s.[31] In 1997, after Amidon *et al.*[32] published their biopharmaceutic drug classification, known today as biopharmaceutics classification system (BCS), the FDA first started to require drug dissolution profiles rather than a single dissolution value.[33] The BCS divides the drugs in four classes: Class I – drugs with a high solubility and high permeability; Class II – low solubility, but high permeability; Class III – high solubility, but low permeability and Class IV – low solubility and low permeability. Over the years, dissolution testing became a critical tool, as it is the only *in vitro* test that investigates the extent and rate of *in vivo* drug product release. This was acknowledged mainly for modified-release products and BCS Class II and IV where assuring consistent *in vivo* drug product performance could be challenging.[34]

Ibuprofen (Ibu-nd) is a non-steroidal anti-inflammatory drug and a weak acid. It falls under Class II according to the BCS due to its pH dependant poor aqueous solubility and high cell permeability.[32] Due to its typical needle shape crystal habit, it shows poor flow properties, low compressibility and a tendency to stick to the die and the punch during compression.[35] However, as it is relatively safe for manual handling a small molecule and widely investigated[1], [36]–[42] well known drug, it is a suitable choice for the purpose of this current work.

In the last two decades, new initiatives including quality by design (QbD) and in-line testing to monitor and ensure process control were presented. QbD is a systematic approach meant to provide robust manufacturing by using control-based manipulation of process parameters, statistical algorithms, design of experiment and quality risk management.[43], [44] QbD aims to define the critical material attributes and the

critical process parameters that relate to the release mechanism, thus creating a link between *in vitro* methods and *in vivo* drug performance.[45] Physiologically based pharmacokinetic modelling and simulation also showed a potential to explain the *in vitro-in vivo* relationships, thus to improve drug product understanding and development.[34] In 2017, the FDA recognized the dissolution testing as a critical tool for establishing biowaivers for immediate-release solid oral dosage forms based on highly soluble drugs Class I and III.[46] Ibuprofen is classified as a Class I drug according to the developability classification system (DCS)[47] due to its high solubility in the intestine where the main part of the absorption occurs, thus there are suggestions that for this drug a biowaiver could be granted.[48]

1.1.3. Factors affecting the dissolution rate

Kapoor *et al.*[27] divides the factors affecting the dissolution rate in six groups depending on the part of the process they relate to.

1) Factors related to the physicochemical properties of the API – solubility, salt formation, polymorphism, and particle size.
2) Factors related to the solid-state characteristics - crystallinity, polymorphic structures, amorphicity, and state of hydration of the drug (hydrates and anhydrates).
3) Formulation factors – effect of all excipients added to the formulation on the dissolution rate, *e.g.*, surfactants, disintegrants, coating agents.
4) Processing factors – compression force, storage conditions, drug-excipient interactions.
5) Factors related to the dissolution test – temperature, pH, medium composition, sink conditions, and others.
6) Factors related to the dissolution apparatus – agitation/flow rate, sampling probe position, filtering, coning, and others.

Dressman[49] reports some other important physicochemical parameters such as surface area, boundary layer thickness, diffusion coefficient along with some physiological (*in vivo*) parameters like GI volume, viscosity of the GI content, motility, permeability, buffer capacity and administered food and fluids.

Thus, understanding and control of the release mechanism is a key element of the drug product development process as immediate-release formulations are more affected by the API properties, while modified-release formulations mainly by the formulation factors.[14]

1.1.4. Dissolution apparatuses

Many companies manufacture and use dissolution apparatuses that serve the purpose of dissolution testing. However, two of the regulatory authorities – the American FDA and the European medicines agency (EMA) accept four types of apparatuses as a standard based on the USP and Eur. Ph. – USP 1 basket and USP 2 paddle apparatuses, used for large medium volumes (500 – 900 mL), and USP 3 reciprocating cylinder and USP 4 flow-through (USP 4 FTA) apparatuses, used for small volumes (100 – 200 mL).[50]–[52] In addition, there are three apparatuses described in the USP which are not included in the Eur. Ph. - USP 5 paddle over disc, USP 6 rotating cylinder and USP 7 reciprocating holder, mostly used for transdermal formulations.[8] Other non-compendial apparatuses also find application during many stages of drug development.[23], [53], [54] In this work, USP 2 paddle and USP 4 FTA apparatuses were used, therefore their specifics are going to be discussed in more detail.

1.1.4.1. USP 2 paddle apparatus

The USP 2 paddle apparatus[50], [51] consists of dissolution vessels placed in a water bath at 37°C and a paddle in each vessel which rotates on its axis. The drug is placed directly inside the vessel typically with 500 to 900 mL of dissolution medium.

This type of apparatus allows a probe for imaging or *in situ* UV analysis to be inserted in the vessel and kept there during the process. However, addition of probes would affect the hydrodynamics in the vessel.[55]

1.1.4.2. USP 4 flow-through apparatus

The USP 4 FTA[50], [51] is a closed system that includes a test cell (12 mm (small) and 22.6 mm (large) inner diameter), a reservoir containing the dissolution medium and a pump (Figure 1.1). The conical base of the flow-through cell is filled with glass beads (1 mm diameter) to maintain a uniform flow, and a ruby bead (5 mm of diameter) at the bottom apex to prevent backflow. This dissolution apparatus is designed to hold the test sample trapped in the test cell, on top of which a filter is placed to prevent undissolved particles escaping. The pump forces the dissolution medium upwards through the cell with standard flow rates (FR) of 4, 8 and 16 mL/min. The consistency of the FR must be within ±5% of the nominal FR with a sinusoidal pulsation of 120 ± 10 pulses/min or a constant flow through the cell has to be maintained.[52] The pump can circulate the fluid from the reservoir through the cell in two operational modes - an open or a closed loop. Designed like this, the system does not facilitate a probe to be inserted into the cell. It is possible to visualize the process inside the test cell by positioning an external camera outside of the cell as described by D'Arcy *et al*[1].

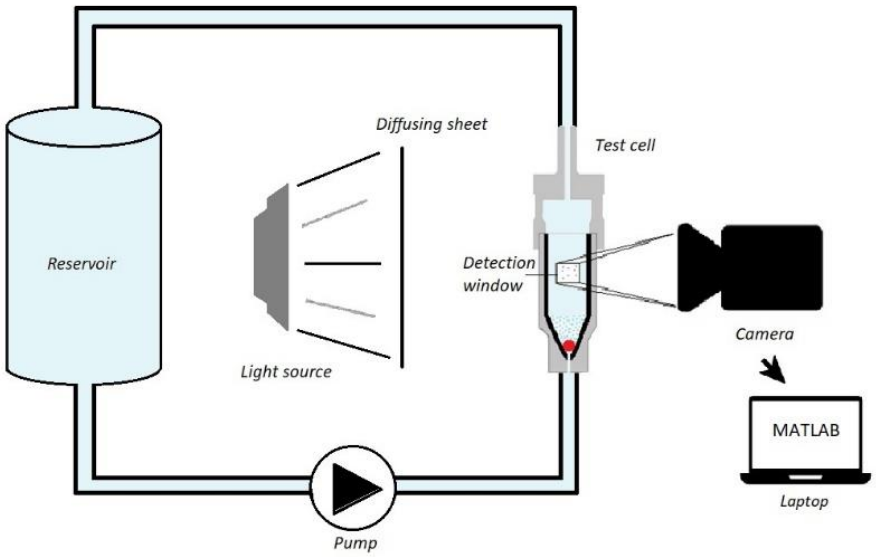

Figure 1.1: USP 4 FTA set up - a test cell, a reservoir, and a pump. Additional shadowgraph imaging (SGI) system consisted of a camera connected to a computer and an LED source. The imaging window was located at the height of the middle of the test cell.

1.1.5. Precipitation of drug particles

Precipitation behaviour of molecularly dissolved drugs is important to predict oral absorption and improve formulation strategies.[42], [56] For example, precipitation and crystal growth are of interest during crystallization[57] and amorphous solid dispersion preparation[58]. Drug precipitation can be observed *in vivo* after dissolution due to physiological pH change in the GI tract[59], [60]. This phenomenon is typical for pH dependant molecules, *e.g.*, theophylline.[61] Precipitation in the GI tract can cause an insufficient, subtherapeutic dose to be delivered to the site of action in the body.

1.1.6. Particle agglomeration

1.1.6.1. Terms and definitions used in the literature

Since 1961 attempts have been made to define and distinguish the terms ‘‘agglomerate’’, ‘‘aggregate’’ and “clump”.[62] The USP describes an agglomerate as “fused or cemented particles” and an aggregate as a “mass of adhered particles”.[63] In this work, the terms “agglomerate” and “aggregate” are used interchangeably, although the author lean towards the term “agglomerate”, to describe two or more particles attached together at their tips (specifically for needle-shaped particles), lying on top of each other or loose clusters of many particles that move together in the dissolution cell. Particle agglomeration can affect the dissolution rate by limiting the surface area of the particles. Agglomeration during a drug crystallization process could influence the properties of the final product.[57] Furthermore, agglomerate formation could become a reason for a product failure due to physical instability, for example, in injectable formulations[64].

1.1.6.2. Drug agglomeration effect on the dissolution process

Advances in pharmaceutical sciences have led to the establishment of several approaches for addressing issues of low aqueous solubility and dissolution rate. These strategies for improving and maximizing dissolution rate include preparation of micro-[65], [66] and nano-[67], [68] particles to increase surface area for dissolution, the use of salt forms[69], [70], amorphous forms[52], amorphous solid dispersions[71], [72] and co-crystals[69], [73]. Particle agglomeration during processing decreases the surface area and can have a negative impact on dissolution performance.[74] For example, micronized particles of poorly-water soluble APIs are prone to agglomeration during processing[65] such as granulation and powder densification via pressure, which can affect the dissolution when used in formulations.

1.1.7. Dissolution of formulations

1.1.7.1. Paediatric oral suspensions

Suspensions are a biphasic system consisting of poorly soluble solid particles dispersed in a liquid phase.[75] The liquid phase usually contains excipients, *e.g.*, suspending agents, matrix/gelling agents (polymers), wetting agents (surfactants) and taste correctors (sweeteners) for oral suspensions particularly containing bitter drugs like most antipyretics and painkillers. Oral liquid forms are a common alternative to tablets and capsules mainly for geriatric and paediatric patients, or patients who cannot swallow solid oral dosage forms. Oral solutions and suspensions allow non-invasive and precise dosing in patients of many different ages and weights. An oral solution can be prepared from highly soluble drugs, class I and III of the BCS, while poorly water-soluble drugs BSC class II (ibuprofen) and IV, where the rate limiting step for bioavailability is their solubility in the GI fluids, have to be formulated as an oral suspension.[76]

Undissolved solid particles in suspensions are similar to the disintegrated form of solid oral dosage forms when they are exposed to aqueous fluids, thus they may share dissolution as a rate-limiting step for absorption and bioavailability.[77], [78] Although the number of monographs regarding oral suspensions has increased in the last two decades, only few of them have recommendations for suitable dissolution conditions.[4], [79], [80] One of the most commonly used and recommended dissolution apparatuses for suspension testing is the USP 2 paddle apparatus with a rotation speed of the paddle between 25 and 50 rpm.[4] A speed of 100 rpm is acceptable for highly viscous formulations to prevent sedimentation.[81] However, issues like correct sample volume measurement and proper introduction of the dose into the vessel remain questionable. A few common practices are 1) weighing of the syringe before and after the dose is delivered to the test vessel to determine the exact weight of the formulation used for dissolution and 2) introduction of the sample to the bottom or to the top of the dissolution vessel to prevent variability related to the position of sample introduction in the apparatus. Regarding sampling position during

dissolution, there are three commonly used locations – top, middle and bottom of the dissolution vessel.[36], [79], [82], [83] USP 2 apparatuses with automated samplers partly solve this problem by taking the sample from the same place every time (middle of the vessel, approximately 1 cm away from the paddle and the wall). An alternative apparatus is the USP 4 FTA, which eliminates the issues of dosage introduction inconsistency as the formulation is added directly on top of glass beads in the test cell immediately before the beginning of the test and samples are taken from the reservoir, where a constant stirring maintains the uniformity of the solute concentration. Media composition with pH in the physiological range also could represent a challenge. Hydrochloric acid (HCl) medium (pH 1 – 2), acetate buffer (pH 3.5 – 5.5) or phosphate buffer (PB) (pH 6.8 – 7.2) may not be suitable to dissolve some of the poorly water-soluble drugs. In this case, addition of enzymes or surfactants could be needed. Frequently, a single dose of the product (*e.g.*, 5 mL) is chosen as a test dose. However, in the case of low drug solubility to dissolve a single dose a higher medium volume may be needed than the standard volume for USP 2 apparatus (500 – 900 mL). Issues related to coning in the "dead zone" under the paddle of the USP 2 apparatus mainly occurring during dissolution of formulations containing insoluble excipients that form a compact mass which surround the API have been reported.[82], [84] A clump formation on the bottom of the dissolution vessel was observed by Rivera-Leyva *et al.*[36] during the dissolution of ibuprofen suspension in acidic medium. Several key parameters have to be considered during suspension development such as API particle size, particle growth, agglomeration, sedimentation an re-dispersal of particles.[85] Addition of viscosity enhancing agents would improve formulation stability, however, formulations with higher viscosity would require a faster rotation speed during testing[5] which could negatively affect the discriminatory power of the method.[81], [82], [84] Although oral suspensions of any viscosity would be exposed to similar conditions in the body, an agitation rate *in vitro* should be chosen to ensure sufficient discrimination between batches or different drug products.[5] An insufficient discriminatory power might result in a false positive bioequivalence decision which could increase the risk for patients. On the other hand, overly discriminative tests would impact negatively the pharmaceutical industry if products are rejected due to over discrimination when they are in fact bioequivalent,

especially in the case of BCS II-containing drug products.[84] Authors express excitement regarding the possibility of extending the biowaivers for BCS class I and III to BCS class II compounds in the future.[48], [61], [86]

Some more challenging drugs require specific dissolution conditions and apparatuses to maintain sink conditions. Addition of solubility enhancers to the aqueous medium (surfactants, co-solvents, or inorganic salts) could be essential. Another approach could be the use of biphasic dissolution media (aqueous-organic system) or changing the medium during the experiment to mimic the GI pH transition (acidic to more basic environment).[76] This transition between media is easier in the USP 4 FTA. While the sample is "trapped" in the test cell, the reservoir containing the medium is held outside, thus, the medium in the reservoir can be easily changed without interrupting the dissolution process. The open configuration mode of the USP 4 FTA allows large volumes of medium to pass through the cell maintaining sink conditions when a poorly water-soluble drug is tested.[87]–[89]

Different phenomena could be observed during dissolution testing of highly viscous formulations, *e.g.*, viscous fingering. Viscous fingering refers to instabilities that occur during mixing between phases of different viscosities.[90] The phenomenon is observed only when a less viscous fluid displaces more viscous one[91], which is the situation in the USP 4 FTA when the medium passes through the oral suspension placed for dissolution. Jha *et al.*[92] describe two competing effects which are a consequence of the viscous fingering. First, a mixing enhancement due to induced mixing disturbance and increased contact area between the fluids, and second, channel formation used as a mainstream by the lower viscosity fluid, thus decreasing the overall mixing efficacy.

1.1.7.2. Challenges related to dissolution in the USP 4 FTA – from API to formulations

Traditional dissolution testing is a well-accepted test in pharmaceutics, however, not everything happening in the test cell/vessel can be explained based only on the

dissolution profile. Differences in the dissolution profile could appear due to inconsistency of the formulation, presence of or a change in the excipients, a change in the API manufacturing process, *e.g.*, the API crystal shape depends on the antisolvent used during the crystallization process.[35], [93] Dissolution testing used on its own cannot show particle behaviour during dissolution such as powder wetting, position in the cell during dissolution, agglomeration tendency[94] and reduction of the contact area, or viscous fingering and channel formation during suspension dissolution[90], [92]. Agitation and sample mixing with the dissolution medium are important factors of the dissolution testing. Mixing disturbances or limited contact area between the fluid and the formulation could result in a change in the dissolution rate. In the case of oral suspensions, if a specific channel formation or a fingering pattern is known for a certain formulation, there is a potential for an analytical quality control tool to be developed and used to monitor product consistency. Imaging analysis has the potential to give a greater insight into some of these issues by using real time monitoring and image analysis, however, comparing images of extended dissolution testing would remain a challenging and time-consuming task.

1.2. Imaging

Over the last two decades, the FDA has released process analytical technology (PAT) guidelines to facilitate the introduction of new technologies for the pharmaceutical industry.[95] PAT involves systems for analysis and control of manufacturing processes to assure acceptable end-product quality. Nowadays, PATs suitable for in-line measurements include vibrational spectroscopy methods, like near-infrared[96], [97], Fourier-transform infrared (FTIR) [98] and Raman spectroscopy[99], [100]. Although not required from a regulatory perspective, visual observations as part of PAT are suggested for development and validation of dissolution methods from USP guidance[8]. From 2010 onwards imaging technologies became more frequently used to observe phenomena such as solid oral dosage forms swelling, disintegration[37], [101]–[104], a single particle dissolution[105], crystal growth[96], [106], [107], particle

sizing and object recognition[1], [108]. While other analytical methods such as UV and IR are used to determine the API quantitatively or chemically, the aim of imaging is to give an insight into the process.[109], [110] For example, magnetic resonance imaging (MRI) was used to quantify the dosage form matrix evolution by three-dimensional *in situ* characterization of the dissolution process in a standard USP 4 FTA.[111], [112] Another visual technique applied to the dynamic conditions in the USP 4 FTA is an x-ray microtomography used to visualize the external and internal structure of a solid dosage form.[113] Although in a customized flow-through cell, UV imaging has also been used to characterize *in vitro* drug dissolution, release and precipitation testing.[114]–[117] Other examples for imaging application include quality control monitoring of insoluble particles present in injectable formulations during preparation[64], [118], and monitoring during fluidized-bed granulation[119].

1.2.1. Application of imaging in dissolution

1.2.1.1. Shadowgraph imaging (SGI)

SGI is a non-invasive, optical technique, which uses a diffuse backward illumination system to capture the shadow image of focused particles.[120] The shadow is obtained as a result of the light beam being refracted by an object of different density, hence the position on the recording plane where the deflected ray would arrive remains dark, while the position where the deflected ray arrives appears brighter (Figure 1.2).[107], [121]–[123] SGI has been described in the literature since the 17th century[124] mainly in the field of fluid dynamics[125] and crystal growth[107], [121], [126]. It has been applied to map convection and concentration during fluid flow processes, to investigate heat and mass transfer and in particle tracking velocimetry studies.[107] SGI can be used for visualization and quantification of particle shape, size and velocity in fluids.[1], [55], [127]–[130] It has been used to show the initial dissolution of a single crystal introduced into a solution. The abrupt change in the solute concentration around the crystal changed the refractive index around the crystal, thus a visualization by SGI was possible.[121]

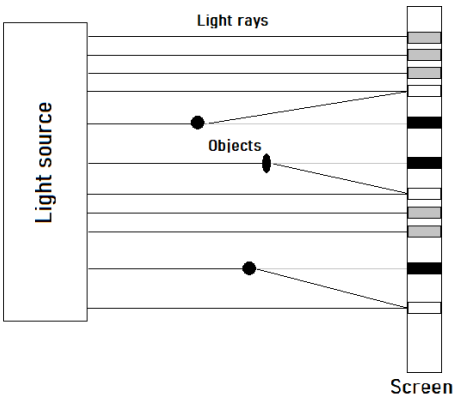

Figure 1.2: Schematic of imaging by a shadowgraph – ray refraction.

An advantage of this method is that insertion of a probe is not required. This makes it compatible with the USP 4 FTA (Figure 1.1). Instead, the data is recorded externally by a recording device, *i.e.*, a camera. D'Arcy *et al.*[1] investigated the accuracy of a mechanistic modelling to simulate the dissolution process in the USP 4 FTA by using real time monitoring to provide information of the particle motion, number and total dissolution time. It was found that the SGI can successfully determine the total dissolution time and decreasing particle numbers over time. It was also suggested that a combination of simulation and real time monitoring would give valuable information about the dissolution process mechanisms and dissolution environment.[1] The same group investigated the particle size change of co-crystals during dissolution in the USP 4 FTA by SGI and compared the data with an offline particle size dispersal measurement based on laser diffraction.[129] They found that the co-crystals are prone to agglomerate in the offline test vessel as it is a closed system, *i.e.*, the limited space could promote increased aggregation behaviour, which was not observed in the flow-through cell when it was used in an open loop. According to their study, SGI could be a promising approach to explore the relationship between particle size, aggregation and dissolution behaviour.[129] SGI has also been applied to visualize the pulsing nature of the particle movement in the flow-through cell[1] and to investigate the behaviour of suspended particles in viscous medium[131].

Two main limitations of this method are the 2D image obtained due to the use of a single camera and the depth of focus. Attempts were made to overcome these limitations by 3D image reconstruction[132] or by installation of two cameras merging particle size information[133]. Legrand *et al.* [120] reported that the focus loss is less obvious for larger objects when they move away from the focus plane. The camera magnification allows micron-sized particles to be captured. However, sizing of the particle could be inaccurate depending on the position of that particle in the test cell. A particle in front or behind the focus plane would result in a blurred image of a larger shadow, while the same particle positioned inside the focus plane would result in a clear image of the particle and more accurate sizing. The sizing of particles depends not only on their position in the test cell, but also on a precise internal size calibration standard. For SGI calibration a grid with known dimensions is used to set the imaging window size before the performing of the test. Based on the size of the imaging window, the system can calculate the particle size by converting pixels into µm.[129]

A recent study investigated crystal size distributions by an SGI in-line probe and compared the results with another optic imaging technique (online microscopy) and a traditional offline method for particle sizing (sieving analysis).[126] In this study, the SGI probe measured continuously the crystal size of the newly formed crystals in the crystallization tank, then a sample was passed to the online microscope during cooling crystallization. It was found that both techniques provide similar results of the crystal size distribution, except at higher temperatures where the microscope transporting system tends to get blocked. SGI successfully detected the evolution of transparent needle-shaped particles under a variety of test conditions. The authors suggest that an industrial application of this method could be possible if the range of test conditions could be extended to suspension density, temperature, pressure, and chemical resistance. Furthermore, they suggest that mathematical algorithms (*e.g.*, neuronal networks) could be used to avoid image analysis failure due to high sample solid content typical for industrial conditions.[126]

1.2.1.2. Other optical techniques

Although Schlieren is also considered a form of shadowgraph imaging, the Schlieren set-up is slightly more complicated than the SGI. It consists of a light source, collimating and condensing lenses, Schlieren head, knife-edge, recording device and post-processing analytical system. The knife-edge is introduced halfway into the focal point to decrease the direct illumination around an opaque object by reduction of any undeflected rays[107], thus to produce a sharp and clear image.[134] In favour of the SGI, neither a knife-edge nor other cut-off is required.

Focused beam reflectance measurement (FBRM) is an *in situ*, commercially marketed particle characterization technique for use in dissolution and disintegration testing.[1] The set-up is simple and similar to that of the SGI. It consists of a probe which is placed directly into the dissolution vessel[135] or the process stream, an electronic unit and a computer for data acquisition and analysis.[136] A laser beam is generated in an electronic unit and reaches the probe through an optical system. Inside the probe, via a set of lenses, the beam is focused on a focal point. When a particle is present in the probe, the light of the laser beam is reflected back to the sensor.[137] There, the light energy is converted into an electric signal. The duration and frequency of signals are indications of particle number and cord length.[136] A cord length is considered the length between two edges of a particle which the emitted laser beam crosses. This technique provides information on the number of particles present in the vessel and one-dimensional information on their size as a function of time.[137] It has been applied in dissolution testing as a real time monitoring tool to monitor disintegration and dissolution of solid oral dosage forms[137], [138], in preclinical development of liquid oral forms, such as suspensions[139], for characterization of amorphous particle populations[140], during wet granulation[141] and particle dispersal. FBRM is a reasonably accurate technique and provides reproducible results for opaque particles with high refractive index. The method is not that sensitive when it comes to characterization of fine transparent

objects such as oil droplets.[142] SGI, Schlieren and FBRM provide non-specific detection of particles suspended/disintegrated in the dissolution medium and give insight about the particle size and the shape based on their projection on a plane. However, methods that provide only one-dimensional characteristic length distribution such as FBRM, are difficult for interpretation and prone to errors and misleading effects when they are used for non-spherical particles.[133] Multi-projection imaging systems have been developed to address shape-related problems mostly during crystallization.[106], [143], [144]

Laser-based and non-photo-optical methods have been used for image analysis workflows and single feature extractions from the images in real time to measure particle size, shape and number of detections (particle concentration).[145] Another study[146] compares some of the commercially available flow imaging microscopy systems for biopharmaceuticals by using protein imaging analysis. One of the findings was that the usefulness of the system strongly depends on the parameters of interest. Some of these systems can be used in combination with the USP 2 paddle apparatus by directly placing a probe inside the dissolution vessel. This application of an imaging system was used to link tablet disintegration and dissolution by measuring in real time the number and size of particles which are generated during tablet disintegration in the dissolution vessel.[101] UV-based imaging was first described in a study by Østergaard *et al.*[147] in 2010. He investigated nicotine release from a transdermal patch and successfully visualized and quantified nicotine concentration gradients by UV imaging in real time. UV imaging is based on the drug UV absorbance to create spatial, temporary analyte concentration maps.[24] Ye *et al.*[148] used this method to investigate the medium diffusion in hydrogels. Other authors utilised UV imaging to determine intrinsic dissolution rates of APIs, dissolution and precipitation drug behaviour, for salts, co-crystals and solid dispersions characterization and a control.[37], [38], [104], [116], [117]

FTIR and terahertz pulsed imaging (TPI) spectroscopy are techniques used to obtain spectrums of absorption or emission of a solid, liquid or gas in the infrared and the terahertz region of the electromagnetic spectrum, respectively. The terahertz region is between the infrared and the microwave range (far infrared).[98], [149], [150] Both

methods have been applied to dissolution and release testing[98], [151], mainly to distinguish APIs and excipients, to give insight into thickness and uniformity of tablet coatings[150], [152], to discriminate polymorphic drug forms[150], [153] and to characterize drug delivery systems[109]. The spectral interpretation and the basic instrumentation are analogous for both methods.[153] They give information on low-frequency intermolecular vibrations, thus they give information related to the functional groups of the substances. Attenuated total reflection-FTIR was used with the USP 4 FTA and USP 1 basket apparatuses to visualize the dissolution and interaction between two layers of bilayer tablets.[151] The TPI measurement is based on many points over the surface of a sample to map it. Each pixel is recorded as a function of optical time delay of the signal. Thus, TPI combines three-dimensional data where the x- and y- axes describe the height and width (horizontal and vertical dimensions) of the sample and the z-axis is the time-delay shows the depth of the sample.[149] This allows thicker samples to be imaged. The TPI uses the refractive index to describe objects, which may be opaque to terahertz radiation, *e.g.*, most excipients used for solid oral dosage forms.[150], [154] An advantage of both methods is that there is no probe to be placed in the test vessel, which makes them potentially suitable to be used in dissolution testing in the USP 4 FTA. However, by using spectroscopy imaging no information related to a single particle such as behaviour, shape or size can be acquired.

Recently, Raman imaging was utilized in the prediction of dissolution profiles of extended- and controlled-release tablets.[155], [156] Raman imaging is a non-destructive technique which collects chemical spectra between 200 and 1800 cm^{-1}. The collected spectra could be used to map the surface of tablets before or during dissolution. Later, these images could be converted to concentration maps of hydroxypropyl methylcellulose (HPMC) responsible for the dissolution rate of controlled-release tablets.[156]

1.2.2. Image analysis

Imaging provides visualization of objects and processes, however for object characterization, *e.g.*, particle sizing, further image analysis is required. Platforms such as Matlab™ provide multiple toolboxes with reference-standard algorithms for image processing, analysis, and visualization. They allow image enhancement, segmentation, noise reduction, investigation of morphology, statistical analysis, size measurement, interactive image and video exploration, plot creation and manipulation of regions of interest.[157] Some imaging systems come with built-in software for image analysis with a broad spectrum of analytical features,[101], [141] while others could be used only offline[158]. Dissolution process could be investigated offline. However, an in-line imaging analysis would provide real time data about the process. [145]

Image analysis was used to analyse images during dissolution and solubility studies, as a monitoring tool of surface amorphous phase separation in amorphous solid dispersions, to describe the dissolution kinetics of a single particle and to measure particle size distribution.[54], [126], [137], [159], [160] In combination with MRI, image analysis was also used for evaluation of controlled-released dosage forms in the USP 4 FTA.[161] Historically, for particle sizing a laser light scattering method was used. Image-based methods were not that popular due to their insufficient development. In the last decade, an increasing trend towards the use of imaging systems is observed.[145], [158], [162] A reason for this could be the improved computational power and systems ability to rapidly calculate statistically reliable data without subjective biases.[162] Nowadays, the evolving systems have less limitations like low memory and the necessity of time-consuming manual particle measurement and filtering. On the other hand, there is a higher demand for imaging tools able to not only measure particle size but to provide valuable information about particle population distributions and particle shape characteristics. The introduction of new complementary technologies equipped with more computational power or low-level early-stage developed artificial intelligence (AI) allowed faster image processing and computer modelling.[1], [129], [163]–[165] However, there is a gap remaining in this field to be fulfilled related to image and AI analysis.[57], [166]–[168]

1.3. Artificial intelligence (AI)

The ability of a computer to recognize objects from an image or to be able to compute variables, find hidden patterns and thus to make suggestions or make decisions is known as AI. Nowadays, AI finds many applications in the everyday life – from spam emails, to face recognition and autopilots. Computer vision and machine learning (ML) methods are implemented in many areas related to pharmaceutics and medicine to provide faster processes and overall better health care.[169]–[173]

1.3.1. History of AI

One of the first publications related to the AI concept in 1943 describes a computer model capable of learning similarly to human neurons. It was named MCP neuron after its creators Warren McCulloch and Walter Pitts.[174] MCP was using logical inputs known as Boolean logic (a specific branch of algebra) which uses true and false statements.[175] The results were based on a threshold score. If the processed value exceeded the pre-set threshold the neuron is considered active, thus it will give as an output a value. With the limitations of just binary outputs and the need of fixed weight and threshold values, this model was the starting point for other scientists to improve this concept.

AI emerged as a term in 1950s after John McCarthy used it during a workshop in England[176] and the Turing test[177] called “The imitation game” by Alan Turing was developed. The game was used to test if machines can exhibit human-like behaviour. During the test people were asked to communicate via computer with someone they cannot see. Then they had to decide if they were talking to another human or a computer. If the person is unable to distinguish the machine from the human, it is considered that the machine passed the test.

In 1958 the MCP neuron concept was improved by processing non-Boolean inputs, scaling of weights and the addition of a nonlinear function for processing the input

values.[178] All these features improved the model flexibility. This model was considered to be the first building block needed for the creation of modern neural networks (NN).[175]

1.3.2. Neural networks (NNs)

The concept of AI combines all computational models and mathematical algorithms able to "learn" from experience and to imitate human brain processes.[169] ML is a collection of techniques which uses algorithms to extract information from data and adaptively improve model performance based on the newly acquired information.[179] To compute more complex tasks, deep learning (DL) as a branch of ML (Figure 1.3), uses NNs based on multiple interconnected layers able to "communicate" with each other and operating in parallel to create a virtual structure performing processes similar to those in the brain, *e.g.*, face recognition, object classification, decision-making, speech/language recognition and movement control.[180]

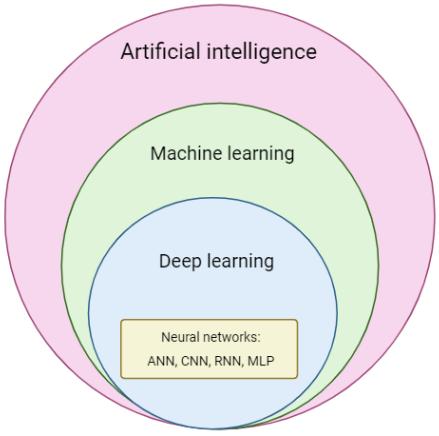

Figure 1.3: Schematic representation of the artificial intelligence (AI) concept. Layers of system development.

NNs (Figure 1.4) are virtual structures consisting of hundreds of single units called neurons, connected with coefficients (weights) and organized into multiple interconnected layers to form a neural structure similar to the human brain. This structure can use output information from one layer as an input to another layer multiple times in a loop until the system "learn" how to recognize the information and minimize the classification mistakes. This type of learning could be supervised, which requires a big amount of pre-labelled data and more or less interaction by a supervisor, or unsupervised – where the data is unstructured (unlabelled), then the system finds its own way to solve the problem by finding patterns without prior training.[181] AI and ML approaches are close to traditional statistical modelling (especially in the case of linear regression), however, they take a different approach to the problem and aim to minimize the human bias in parameter selection.[182] Generally, AI has four functions based on the type of learning – 1) classification of data into categories, 2) regression, where the system is trying to understand the relationship between dependant and independent variables (supervised learning), 3) clustering of unlabelled data based on similarities or differences and 4) association where AI is looking for different ways to find relationships between variables in a given data set, *e.g.*, "you like this – you may also like this" suggestions.

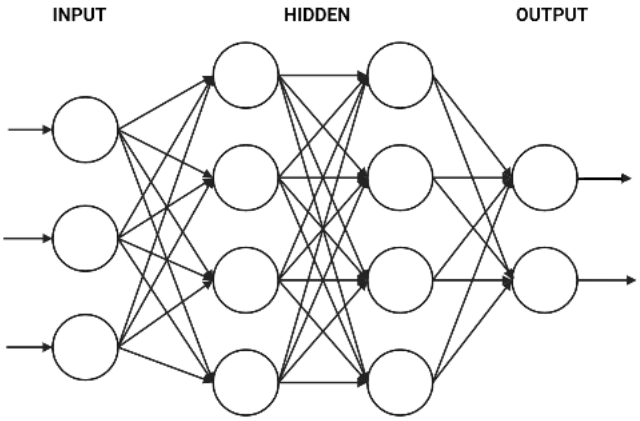

Figure 1.4: Schematic structure of artificial neural network (ANN) architecture.

Some of the commonly used NN are artificial NN (ANN)[167], convolutional NN (CNN)[183], [184], multilayer perceptron (MLP), recurrent neural networks (RNN), k-means clustering, k-nearest neighbour, autoencoder NN and sequence to sequence. In this introduction, a brief description of ANN and CNN is presented as background knowledge regarding the NN used in this work. For deeper understanding of ML and AI concepts the author would refer the readers to Joshi *et al.* and other recent articles for more information.[185]

Nowadays, ANN is used as a general term for any NN, then specific features related to that specific NN are mentioned. However, ANNs are a class of NNs with their own specifics. ANNs were the first and simplest NNs to be created. They pass the information only in one direction and are known as "feed-forward" NNs.[186] It is useful for big tabular and text data sets. It has fault tolerance, and it can operate in a supervised or unsupervised mode. In recent years, the use of ANNs drew attention to their possible application in pharmaceutical development.[187] They were recognized as promising modelling techniques mostly in relation to processing big data sets and data with non-linear relationships common in pharmaceutical processes. Compared with conventional statistical methods, NNs are able to easily detect complex relationships between related or unrelated variables. They can make use of incomplete data, they can use multiple algorithms and hidden layers without complicated equations, and they can use literature and experimental data in the decision-making process.[163], [167] Since their creation, ANNs have been used in drug formulation development[188] and evaluation[165], for data analysis and decision-making in many areas of pharmaceutical research[189], and for prediction of drug dissolution profiles[190].

CNNs are more complex than ANNs and contain one or more convolutional layers, which can be connected or pooled. CNNs use non-linear processing. They show high accuracy when used for image recognition, and they can detect important features when unsupervised. This type of NNs is considered more powerful than ANNs and RNNs and it is mostly used for image data. The system does not encode the position and the orientation of the image, which could be used as an advantage or seen as disadvantage of the NN. However, a main disadvantage is the need of large training

data set. It has been generally applied to face recognition, text digitalization and natural language processing. In pharmaceutics some of the applications include formulation surface defect detection, prediction of particle packing density and flowability, object detection and classification.[183], [184], [186], [191]

RNNs are more complex than ANNs and CNNs as an RNN passes the information in multiple directions, not only forward. This gives the opportunity to predict the outcome of another layer. In this system each neuron unit acts as a memory cell. In the case of a wrong prediction, the system self-improves and continues the computation and implementation of operations towards the correct prediction. RNNs are powerful dynamic systems, which makes their training problematic due to backpropagated gradients which are known to explode or vanish. RNN is useful for sequence data and has been applied into text-to-speech operations, to predict the next character in a word or a word in a sentence, text translation and autocorrect.[186], [191] Although in pharmaceutics RNNs are not widely applied, attempts were made to use them to predict drug dissolution profiles.[192]

A combination of SGI and CNN have been applied to detect particles and bubbles, and for size and shape characterization.[130], [193]–[195] Both Ilonen *et al.* and Poletaev *et al.* applied single bubble pre-trained CNN model to a bubble image and used it to extract each individual bubble.[193], [195] Ilonen's method required manually labelled data for model training and testing, which could be highly time-consuming task and it is prone to human errors even for a small data set. Poletaev *et al.* managed to improve the accuracy of the system by connecting three consecutive CNNs and a bubble detector CNN. Although, this system showed more than 90% accuracy, it has an extensive processing time due to the usage of multiple CNNs able to extract only one bubble at a time.[130] Li *et al.* developed a shadow image characterization method based on a single modified U-net CNN with improved detection rate (compared to systems based on three CNNs), which also provides particle size and shape measurement. Although this method has some advantages over other methods, it suffers from loss of particle information due to overlapping particles in agglomerates, which needs further development.[130]

1.4. Introduction summary

In summary, dissolution testing evolved over the last century and became a widely accepted procedure during drug discovery, routine manufacturing, approval of generics, new dosage forms and for post-approval monitoring. Nowadays, there are multiple compendial and non-compendial apparatuses, biorelevant media and better understanding of physiological phenomena which could occur in the GI tract.[17], [82], [196] However, there are remaining challenges which needs to be faced such as describing particle behaviour during dissolution, detection of agglomeration and precipitation tendencies, finding proper test conditions for more challenging drugs, *e.g.*, BCS class II and IV, understanding the effect of addition of surfactants, co-solvents and enzymes to the medium and how to guarantee the *in vitro-in vivo* relationship.[81] Imaging and computer simulations came as supportive tools able to describe the dissolution process and even to predict an experiment outcome. Simulations give insight regarding *in vivo* events and could be used as a prediction tool, while imaging gives real time information and the possibility for further image analysis. Imaging systems which require a probe are suitable for open systems such as the paddle apparatus, although they could affect the hydrodynamics in the vessel.[55] MRI and UV imaging do not require a probe to be inserted and are helpful for visualizing, *e.g.*, tablet swelling. However, they are not satisfactory in the study of agglomerates or single particulates. SGI could be used in a closed system such as the USP 4 FTA. A limitation of this technique is the small depth of focus. Nevertheless, image analysis could be extremely time-consuming, it could be affected by overlapping particles, background noise, low resolution of the image and lack of comparable data – in the case of particle sizing a precise calibration is needed. Another limitation is the processing power available and the storage space. High resolution cameras record large size images and videos which could be difficult to process.

The emergence of AI, more specifically ML and NN raise hopes for faster and more precise image processing exceeding human interpretation. NNs have been applied in several studies and show great potential, although most of them still need training

with manually labelled data, which is also time-consuming step as well as the time for training which may vary depending on the processing power.

1.5. Aims and objectives

The aims of this work were to investigate particle and formulation dispersal in the USP 4 FTA test cell, to explore the application of real time monitoring and AI-based image analysis to describe the dissolution process and to observe the effect of the environment changes related to the dissolution apparatus, medium composition, and crystal habit on the dissolution process.

These aims were achieved by 1) studying the effect of adding different concentrations of surfactant, changes in the FR, different initial drug mass used for dissolution and different crystal habits (plates and needles); 2) exploring the potential to develop and apply an automated agglomeration identification method (AIM) through real time dissolution imaging analysis as a proof of concept of development of a tool for automatic identification of phenomena in dissolution images in order to build a training image set for future AI event analysis; 3) visualizing events occurring in the test cell (*e.g.*, precipitation, bubbles) and using them to create a NN-based classification method for event detection in real time; 4) deepening the understanding of the oral suspension behaviour during dissolution and applying two CNN approaches were applied to support the interpretation of the dissolution profiles and to identify possible ways to distinguish between test products, and finally, 5) researching the application of alternative dissolution/imaging system (paddle apparatus and Canty™ imaging and analysis system) for characterization and prediction of the dissolution and precipitation process of API was explored.

Chapter 2: Materials and methods

Some of the methods presented in this Chapter were presented in: Taseva A.R., Persoons T., D'Arcy D.M. Application of an AI image analysis and classification approach to characterise dissolution and precipitation events in the flow through apparatus. Eur J Pharm Biopharm. 2023 Aug; 189:36-47. doi: 10.1016/j.ejpb.2023.04.020. Epub 2023 Apr 27. PMID: 37120067 and 2) Taseva A.R., Persoons T, Healy AM, D'Arcy D.M. Application of shadowgraph imaging (SGI) particle characterisation data to interpret the impact of varying test conditions on powder dissolution and to develop an automated agglomeration identification method (AIM) in the USP flow-through apparatus. Int J Pharm. 2024 Dec 5; 666:124778. doi: 10.1016/j.ijpharm.2024.124778. Epub 2024 Sep 28. PMID: 39349225.

2.1. Materials

Ibuprofen raw material powder was purchased from Glentham Life Sciences Ltd. and was used un-sieved (as received) (Ibu-nd) and in sieved fraction (Ibu-nd-S). This raw material (Ibu-nd) was also used for the preparation of ibuprofen plate-shaped crystals (Ibu-pl), which sieved fraction (Ibu-pl-S) was used for dissolution. Commercially available ibuprofen-containing paediatric oral suspensions Nurofen (Reckitt Benckiser Healthcare International Ltd, UK) and Brupro (Pharmachemie B.V., The Netherlands) 100 mg in 5 mL (N100 and B100, respectively) and 200 mg in 5 mL (N200 and B200, respectively) were purchased from a local pharmacy.

Potassium phosphate and HCl were obtained from Honeywell Fluka (Fluorochem Ltd), sodium hydroxide was obtained from VWR chemicals (Part of AvantorTM), polysorbate (Tween) 20, deionised water, acetonitrile, trifluoroacetic acid and hydrophilic polytetrafluoroethylene membrane filters (pore size 45 µm) (Fisher Scientific) were obtained from Sigma-Aldrich (Merck KGaA), and 2.7 µm glass microfiber filters (GF/D) were received by GE Healthcare Life Sciences (Whatman™).

2.2. Methods

2.2.1. Experimental methods

2.2.1.1. Media preparation

2.2.1.1.1. Phosphate buffer (PB) pH 6.8

The dissolution media were prepared in accordance with the guidelines provided in the USP and the Ph. Eur.[51], [197] To prepare 1 L of 0.2 M PB, 6.8 g of potassium phosphate monobasic were dissolved and mixed with 112 mL of a 0.2 M sodium hydroxide solution and Millipore Elix 3 deionised water . The pH was measured and adjusted to 6.80 ± 0.05 by adding a few drops of 0.2 M NaOH, if needed, and made up to 1 L with Millipore Elix 3 deionised water. Tween 20 at different concentrations (0.003, 0.005, 0.01, 0.05% w/v) was added during the media preparation, as relevant. Prior to the dissolution test, the medium was gently heated up to 41°C and degassed by vacuum filtration through a hydrophilic polytetrafluoroethylene membrane filter with pore size of 0.45 µm under continuous stirring, then cooled down to 37°C before use.[197]

2.2.1.1.2. Hydrochloric acid solution (HCl)

Two HCl solutions (0.1 N and 0.2 N) were used as precipitating agent for the precipitation experiments. These solutions were prepared by diluting 8.3 mL and 16.6 mL of 37% HCl respectively with Millipore Elix 3 deionized water up to 1 L. The solution was degassed according to the pharmacopoeia as described in section 2.1.1.1[197].

2.2.1.2. API and formulation characterization

2.2.1.2.1. Solubility study

The solubility of ibuprofen was measured by the shake flask method.[198] Saturated solutions were prepared by adding 160 mg ibuprofen to 13 mL of PB with and without Tween 20 in a screw cap test tube. Solutions were prepared in triplicate and placed in a shaking water bath at 37°C and 100 cycles per minute (Precision Reciprocal Shaking Bath Model 25). Samples were withdrawn after 1, 3, 5, 24 and 26 hours, with the stated solubility being the 26-hour value. They were filtered through a 0.45 µm hydrophilic polytetrafluoroethylene filter and analysed by UV-Vis spectrophotometry (PharmaSpec 1700, Shimadzu) undiluted at 222 nm and/or 264 nm.

2.2.1.2.2. Sieving

Fractions from Ibu-nd and Ibu-pl with particle size of 106 – 300 µm were collected by using a set of sieves and sieve shaker (Precision Reciprocal Shaking Bath Model 25, Retsch GmbH, Germany).

2.2.1.2.3. Particle size analysis

The particle size and distribution of Ibu-nd were measured by using the laser diffraction method (Mastersizer 3000, Malvern Inc, UK) at room temperature (20°C) in wet mode.

2.2.1.2.4. Optical microscopy

All suspensions and ibuprofen crystals (Ibu-nd and Ibu-pl) were visualized by optical light microscopy at room temperature. Small amount of the API powders or a drop of each suspension was placed on a glass tile and covered by a covering glass. Images of the ibuprofen crystals were taken by using an Olympus BX53 optical microscope (Mason Technologies) with a 20x magnification.

2.2.1.2.5. Density

To measure the density of the suspensions, 50 mL volumetric flasks were used (n = 3) as recommended in the USP[80]. The density of all suspensions was measured at 20°C and 37°C. Suspensions were well shaken as directed in the manufacturing instructions, then transferred into the flasks up to the mark. The density was calculated from the observed weight.

2.2.1.2.6. Viscosity

The dynamic viscosity of the oral suspensions was measured at 20°C and 37°C using a tuning fork vibro viscometer (A&D Instruments, Ltd., UK) (n = 3). The apparatus was calibrated with Millipore Elix 3 deionized water at 20°C and 37°C. The suspensions were kept at room temperature or pre-heated up to 37°C before measurement. The bottles were shaken well before use as per the manufacturer recommendations. The average value of the three measurements was divided by the density to calculate the real suspension viscosity in mPa.s.

2.2.1.3. Dissolution testing

2.2.1.3.1. Dissolution in the USP 4 FTA

Dissolution testing was performed in the USP 4 FTA single cell (CE1) (n = 1) and commercially available seven cells (CE7) (n = 3) apparatus (Sotax AG, Aesch, Switzerland). Both set-ups were equipped with large (22.6 mm inner diameter) and small (12 mm inner diameter) test cells. Each cell had one 5 mm ruby bead at the bottom apex of the cell and glass beads filling the conical part of the cell (Figure 1.1).[89] Samples were placed directly on top of the bed of glass beads. A 2.7 µm glass microfiber filter was placed at the outlet of the cell to retain undissolved particles. A 200 mL reservoir kept at 37°C in a closed-loop configuration, sealed with parafilm and with constant stirring of 200 rpm was connected to each test cell. A pulsing flow of 8 or 16 mL/min ± 5% was used to circulate the medium upwards through the test cell.

Ibu-nd, Ibu-nd-S and Ibu-pl-S were tested in USP 4 FTA CE1 and CE7 under various conditions (Table 2.1). The sampling time points were at 2, 4, 6, 8, 10, 15, 20, 25, 30, 40, 50, 60, 80, 100 and 120 minutes in CE7 for all tests, up to 60 minutes for Ibu-nd and up to 120 minutes for Ibu-nd-S and Ibu-pl-S in CE1. Results from the dissolution tests in the USP 4 FTA CE1 are presented in Appendix 2. Undiluted samples were analysed by UV-Vis spectrophotometry at wavelengths 222 nm or 264 nm.

The suspensions were tested only in USP 4 FTA CE7 at FR 16 mL/min with sampling time points at 5, 15, 30, 45, 60, 75, 90 minute of the test and then every half an hour up to 150 min for N100 and N200 and up to 270 min for B100 and B200. Samples were filtrated through a 0.45 µm hydrophilic polytetrafluoroethylene filter and analysed by a high-performance liquid chromatography system (HPLC) with an UV–Vis detector (λ_{max} = 254 nm). Sample volumes were immediately replaced with fresh medium at 37°C.

Table 2.1: Dissolution conditions used in the USP 4 FTA. Abbr.: AIM – agglomeration identification method, Ibu nd (S) – needle shaped ibuprofen crystals (sieved), Ibu pl(S) – plate shape ibuprofen crystals (sieved), PB – phosphate buffer, FR – flow rate.

Drug	Drug weight (mg)	PB medium with Tween concentration (% w/v)	FR (mL/min)	AIM step**
Ibu-nd	**4, 20, 100**	**0**	**8, 16**	
	40	**0.003**	**8, 16**	**Step 4**
	4, 20, 100*	**0.005**	**8, 16**	**Step 3**
	50	**0.01**	**8, 16**	**Step 4**
	4, 20, 100	**0.05**	**8, 16**	
Sieved size 106 – 300 µm				
Ibu-nd-S	**20**	**0.005**	**8, 16**	**Step 2**
Ibu-pl-S	**20**	**0.005**	**8, 16**	**Step 2**

* Only 100 mg Ibu-nd was used in step 3 of AIM.

** All videos used in steps 2,3 and 4 of AIM were manually investigated in step 1.

2.2.1.3.2. Dissolution in the USP 2 paddle apparatus

Dissolution tests of Ibu-nd 250 mg in 500 mL PB 0.005% and 0.05% w/v Tween 20 were carried out in USP 2 paddle apparatus (Agilent Technologies 708-DS, Santa Clara, CA, USA) at 50 and 100 rpm (n = 3). The drug was added on the top of the medium, immediately before the beginning of the test. Samples were withdrawn at 2, 4, 6, 8, 10, 15, 20, 25, 30, 40, 50, 60, 80, 100 and 120 minutes and volumes were replaced with fresh medium at 37°C. All samples were filtrated through a 0.45 µm hydrophilic polytetrafluoroethylene filter before UV analysis.

2.2.1.4. Precipitation experiments

2.2.1.4.1. Precipitation in the USP 4 FTA

Precipitation tests were conducted under 5 different conditions and 3 initial ibuprofen concentrations (0 mg/mL (control), 0.5 mg/mL and 2 mg/mL, Table 2.2) to generate different precipitation conditions and kinetics. A control test was conducted by filling the test cell and the related tubes with PB 0.05% w/v Tween 20 then connecting it to a reservoir with HCl. A HCl solution (0.1 N or 0.2 N) was used as a precipitating agent to reduce the pH of the medium hence to reduce the solubility of the ibuprofen and to cause its precipitation in the test cell. The medium was circulated as explained in Table 2.2. In 3 of the 4 cases containing ibuprofen, a solution of Ibu-nd dissolved in PB 0.05% w/v Tween 20 at 37°C was prepared prior to the precipitation test. For the remaining test, a dissolution study using 100 mg of ibuprofen was conducted and after 160 minutes when no particles were observed to be present in the test cell the medium was changed to HCl. The control test without an API was conducted to confirm that the reformed particles and plume observed after the medium change in the other tests related to ibuprofen.

Table 2.2: Precipitation conditions used for acquisition of plume, particles and empty images.

Initial drug concentration in PB 0.05% w/v Tween 20	Solution added into the test cell (mL)	Concentration of HCl	Volume of HCl used (mL)	Ratio solution/HCl	Flow rate (mL/min)	Loop configuration	Comment
0 mg/mL	25	0.2 N HCL	25	1 to 1	2	closed	The flow rate was changed to 8 mL/min after 180 min of the test.
0.5 mg/mL	10	0.1 N HCL	100	1 to 10	2	closed	Solution added directly to the test cell, HCl kept in the reservoir. Plume appeared immediately. Particle reformation was seen after 20 minutes.
0.5 mg/mL	25	0.2 N HCL	25	1 to 1	2	closed	Solution filled in the test cell and the tubes (in/out flow), HCl kept in the reservoir. The first contact between the two media was in the inflow tube. A few particles were detected in the beginning of the test, then plume was formed when more HCl entered in the test cell. Single particles were visible again after 160 minutes.

Initial drug concentration in PB 0.05% w/v Tween 20	Solution added into the test cell (mL)	Concentration of HCl	Volume of HCl used (mL)	Ratio solution/HCl	Flow rate (mL/min)	Loop configuration	Comment
2 mg/mL	25	0.2 N HCL	25	1 to 1	2	closed	Solution filled in the test cell and the tubes (in/out flow), HCl kept in the reservoir. The first contact between the two media was in the inflow tube. Plume appeared immediately. Single particles were visible after 180 minutes.
0.5 mg/mL	25	0.1 N HCL	35	1 to 1.4	8	closed and open	A dissolution test was conducted followed by medium change. Images of the solution without the presence of particles were recorded. Open loop was used for 4 minutes to let HCl into the test cell. The system was left without circulation for 2 minutes. Then the medium was recirculated for 10 more minutes in a closed loop. Both particles and plume formation were observed immediately after the medium change.

2.2.1.4.2. Precipitation in the USP 2 paddle apparatus

For the precipitation tests in the USP 2 paddle apparatus, 4 initial ibuprofen concentrations were prepared – 0 mg/mL (control), 0.5 mg/mL, 1 mg/mL and 2 mg/mL in PB 0.05% w/v Tween 20 prior to the experiment. Equal volumes of the drug solution and 0.2 N HCl were mixed directly in the dissolution vessel to a total volume of 500 mL (n = 1). Although samples were not taken, videos of the process were recorded.

2.2.1.5. Analysis

2.2.1.5.1. UV analysis

Samples were measured directly at 222 nm and 264 nm depending on the concentration. The system was calibrated by preparing a calibration curve from Stock solutions (n = 3). The concentration ranges of the calibration curves were as follows: 0.125 – 20 mg/mL at 222 nm and 5 – 600 mg/mL at 264 nm. The calibration curves used to determine the concentration of ibuprofen are presented in Appendix 1.

2.2.1.5.2. High-performance liquid chromatography (HPLC)

Samples were filtered through a 0.45 µm hydrophilic polytetrafluoroethylene filter and analysed by a HPLC system (Alliance, Waters, Santry, Ireland) with a UV–Vis detector (λ_{max} = 254 nm). The HPLC method consisted of an isocratic system with an e2695 HPLC separations model, 2489 dual absorbance detector (Waters, Santry, Ireland), autosampler and temperature control module. The column used was a reverse phase Thermo Scientific Hypersil™ BDS C18 column (4.6 mm × 250 mm, 5 µm). The mobile phase was 70:30 acetonitrile/0.1% v/v trifluoroacetic acid. The flow rate was 1 mL/min, injection volume 10 µL, temperature of the column 30°C. The running time for analysis was 10 min. Data were obtained by using Empower 3 software (LOD =

10.15 µg/mL; LOQ = 30.77 µg/mL). The calibration curves used to determine the concentration of ibuprofen are presented in Appendix 1.

2.2.1.6. Imaging

2.2.1.6.1. Imaging set-up used with the USP 4 FTA

A schematic of the experimental imaging set-up used for direct imaging and SGI analysis is presented in Figure 1.1.[1], [129] It consists of a standard USP 4 FTA test cell positioned in a customised water jacket with flat sides, to ensure light beam transition between the light source and the camera, and connected to a reservoir kept at 37°C during the test. A high-speed CMOS Grasshopper 3 (Teledyne FLIR / Point Grey Research) GS3-U3-23S6C-C camera (1920 x 1200 pixel, 24-bit) was focused on the centre of the test cell above the glass beads. A Nikon 105-mm lens is mounted on a 150-mm long extension tube, resulting in an imaging window approx. 7x11 mm² for the API tests and approx. 5x8 mm² for the suspension tests. An LED light source with diffuser plate is positioned opposite of the camera. Videos at 15 s length and 10 frames per second (fps) were recorded at every dissolution sampling time point for the dissolution tests, with the recording acquired every minute in the first 5 minutes, then every few minutes as appropriate up to 180 min for the control and 1 mg/mL API, and up to 330 minutes for 0.5 mg/mL and 2 mg/mL API for the precipitation experiments.

Shadowgraph imaging and analysis were conducted in the USP 4 FTA CE1 (n = 1) apparatus for the API dissolution and precipitation tests. Imaging of the dissolution of suspensions was conducted in the USP 4 FTA CE7. The dissolution testing was done in triplicate, while the camera was attached to only one of the test cells (n = 1).

2.2.1.6.2. Canty imaging in USP 2 paddle apparatus

A Mini-cell LED Inflow Canty™ (JM Canty, Ltd., Ireland) set-up was connected to one of the dissolution vessels in the USP 2 paddle apparatus. Mini-cell LED Inflow Canty™

consists of a Canty™ particle size analyser with a high-resolution camera with microscopic optics (0.7 µm to 1 mm), a cool LED visible light source and a pump. The system is equipped with CANTYVISION intelligent analysis software (CVIA), and a Canty™ vector control module to analyse the recorded videos. The pump circulates samples between the dissolution vessel and the camera. The system can operate in an open or closed loop (similar to the USP 4 FTA). Thus, to collect the samples in a separate reservoir or to returns them back to the dissolution vessel. In this current work, only the closed loop mode was used. Videos of the dissolution experiments were taken at every sampling time point (2, 4, 6, 8, 10, 15, 20, 25, 30, 40, 50, 60, 80, 100 and 120 min) with a lens distance of 100 µm. To investigate the effect of the lens distance, distances in the range 25 to 250 µm were used during the precipitation of 1 mg/mL ibuprofen for a short time (12^{th} to 17^{th} minute of the test). During the precipitation experiments, 15s videos were recorded as appropriate – more frequently in the beginning of the test and less often after 30 minutes up to 330 minutes for drug solutions and up to 210 minutes for the control.

2.2.2. Computational methods

2.2.2.1. Shadowgraph imaging

2.2.2.1.1. Particle detection and sizing

Videos from the dissolution testing of Ibu-nd in the USP 4 FTA CE1 were analysed in Matlab™ using an in-house written code[131] provided by Prof. Tim Persoons. Based on predefined settings, the software uses a grey scale to distinguish particulates (shadows) from the background and to characterize them resulting in an output video with the detected particles highlighted and sized (Figure 2.1), and a particle parameter data sheet. The following is a non-exhaustive list of the parameters collected for each particle detection (Npd): time of detection (s), particle diameter (mm), and solidity. The latter is a dimensionless parameter defined as the area fraction of the particle region divided by its convex hull area. The convex hull can be visualised as the 2D shape enclosed by a rubber band stretched around the particle region (Figure 2.2). This

parameter was used to develop the automated AIM described in the following section. The detectable particle size range was between 10^{-6} m and 10^{-3} m.

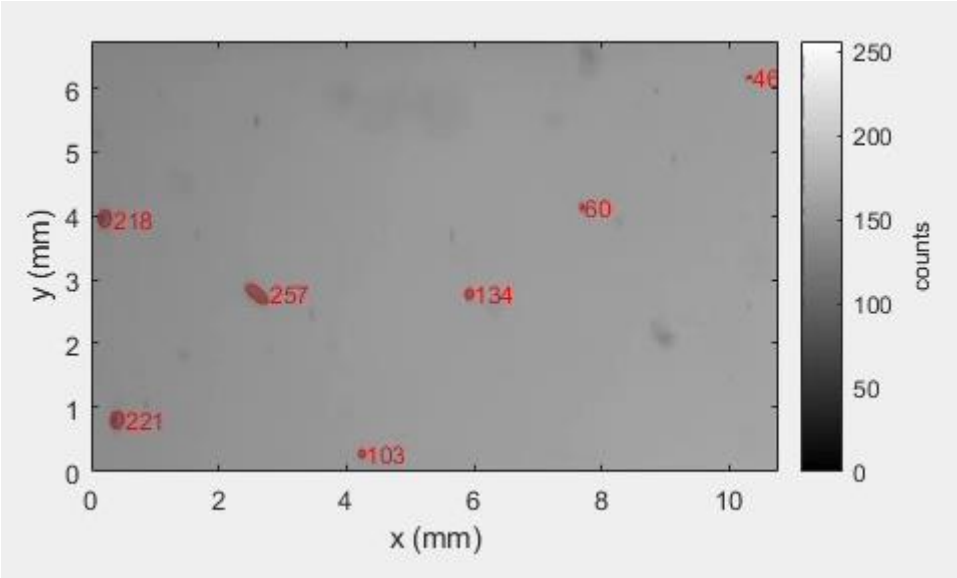

Figure 2.1: SGI imaging window with detected particles outlined in red and their diameter in (µm), a grey contrast scale on the right axis and imaging window dimensions x and y (mm).

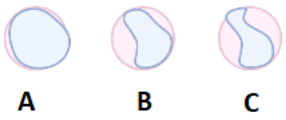

Figure 2.2: Schematic presentation of approximate particle solidity – >95% (A), 70% (B) and 60% (C). Note: The percentages given in this figure are only illustrative.

2.2.2.1.2. Automated agglomeration identification method (AIM) development

The AIM (code provided in Appendix 3) was developed in four steps (Figure 2.3):

1) Manual video observation and creation of a reference image data set including all agglomerates and their occurrence time; 2) Selection of parameters and parameter

combinations (Table 2.1) describing the agglomerates of both sieved particle types (sieved fraction of ibuprofen needle (Ibu-nd-S) and plate-shaped crystals (Ibu-pl-S), mass used for dissolution – 20 mg); 3) Selection of the three best performing parameter combinations from step 2 and testing on particles of unknown size range and higher mass used for dissolution (unprocessed ibuprofen un-sieved fraction (Ibu-nd), mass used for dissolution – 100 mg); 4) External validation of the best performing parameter combination on unknown size particles (Ibu-nd) in new test conditions (Table 2.2). A logical flag function was used to create an array containing detections that meet (= 1) and do not meet (= 0) the combination of pre-set criteria. When plotted, these flags point out the time of a potential agglomerate appearance. For clarity, the terms "signals" and "flagged" particles/detections are used for detections that meet a pre-set criteria combination, for example, diameter below mean and solidity above 96%, as described in Table 2.3.

- **Step 1**, Reference Image Data Set: All videos from the dissolution tests in CE1 in PB 0.005% w/v Tween 20 were manually analysed. Videos from early time points of the dissolution tests (2 – 10 min) of the Ibu-pl-S, Ibu-nd-S and Ibu-nd were selected for further manual analysis and agglomerate occurrence times were noted. Two videos with Npd < 400 and Npd ≤ 50 with size > 300 µm for each particle type (Ibu-pl-S and Ibu-nd-S) (step 2) and 4 videos with Npd < 1000 for Ibu-nd (step 3) were analysed to create the relevant reference image data sets.

- **Step 2**, Performance Evaluation (Sensitivity): As the particle size range was known for Ibu-nd-S and Ibu-pl-S, particle diameter was one of the two parameters used for agglomerate description. The solidity was the second parameter to be considered. Previous observations of the particle parameters suggested lower solidity (approx. < 85%) for agglomerates typical for Ibu-nd. By using the in-house written codes, flexible values (*e.g.*, mean, percentile) of diameter and solidity relevant for each test video were calculated and plotted. In total, nine parameter combinations were tested (Table 2.3). When a particle met both criteria from a specific combination, a

signal was generated. In step 2, the criteria combination performance was assessed based on the highest agglomerate detection rate.

- **Step 3**, Refined Performance Evaluation (Specificity): The three best performing parameter combinations (highlighted in Table 2.3) from Step 2 were further assessed on images from dissolution testing of Ibu-nd. The assessment was based on the lowest false positive signal rate without compromising the agglomerate detection ability. When the Ibu-nd signals were < 100, the percentage of false positive signals was calculated.

- **Step 4**, External Validation: The new test conditions were as follow (Table 2.2): 40 mg (at FR 8 and 16 mL/min) and 50 mg (at FR 8 and 16 mL/min) un-sieved Ibu-nd dissolved in PB with 0.003% w/v and 0.01% w/v Tween 20, respectively, at 37°C for 2 h. Videos were taken as described in Chapter 2, section 2.2.1.6.1 (Imaging set-up). The performance of the method was assessed by comparing the results with a reference data set created after manual video observation (as described in step 1).

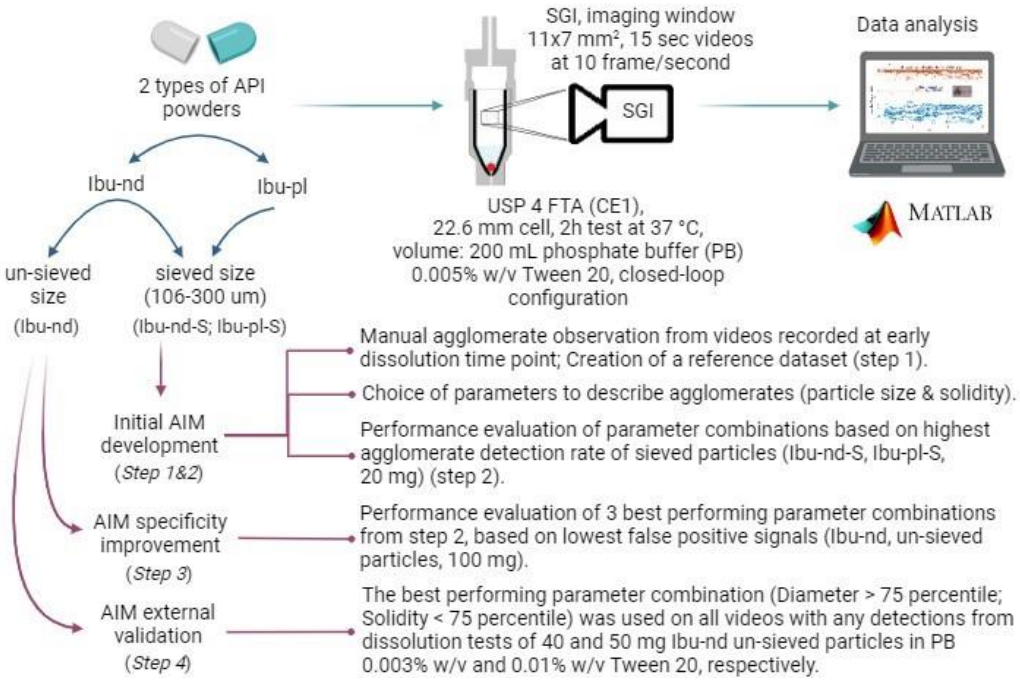

Figure 2.3: Schematic presentation of the methods used for dissolution, SGI and AIM development. Abbr.: SGI – shadowgraph imaging, API – active pharm. ingredient, USP – United States Pharm., FTA – flow through apparatus, CE1 – single cell, Ibu nd/pl(S) – ibuprofen needle/plate-shaped particles (sieved), AIM – aggl. ident. method.

Table 2.3: AIM parameter combinations tested to detect agglomerates. Diameter above and solidity below the specified value. Abbr.: Pr – percentile; D – diameter; S – solidity. The three best performing combinations in step 2 are highlighted.

Diameter criterion	Solidity criterion
D > 300 µm	**S < 85%**
D > Mean	**S < PrS10**
D > Mean	**S < 96%**
D > PrD75	**S < 96%**
D > PrD75	**S < PrS10**
D > PrD75	**S < PrS75**
D > PrD80	**S < PrS30**
D > PrD90	**S < PrS10**
D > PrD90	**S < PrS30**

2.2.2.2. Artificial intelligence (AI) CNN classification and event detection model

2.2.2.2.1. One-class anomaly detection model overview

A comprehensive description of the method adapted for use in the current work is available via Matlab™ (https://uk.mathworks.com/help/vision/ug/detect-image-anomalies-using-explainable-one-class-classification-neural-network.html), in the following section a brief higher-level overview is provided.

A transfer learning technique[180], [199] was used in the current work to develop an anomaly analysis method by using an available Matlab™ code, as a base. This code, used to classify images showing whole (normal), or chipped or dirty tablets (anomalous), is provided in the Matlab™ example "Detect image anomalies using explainable one-class classification neural network" and involves training an anomaly detector for visual inspection of tablet images. This exemplar code explores the possibility to create effective anomaly detectors based on a heatmap mean anomaly score value. This anomaly score value gives the probability that each pixel in the image is anomalous. The example contains a data set with 149 normal tablet images, 43 chipped tablet images, and 138 dirty tablet images divided in 3 folders, where both chipped and dirty tablet images are considered anomalous. To simulate a more typical semi-supervised workflow, the data is partitioned into training, calibration, and test data sets.

The system uses a fully convolutional data description model to train a CNN to produce a heatmap from an input image. The neural architecture is based on a visual geometry group 16 network (VGG-16), trained on ImageNet (an image database) (https://www.image-net.org). VGG-16 is a standard deep CNN architecture with multiple layers, where 16 stands for a network which is 16 layers deep. The image input layer is replaced with a new layer that performs zero-centre normalization and set the input image size to match the image data set. The final convolutional stage consists of randomly initialized and trainable convolutional layers. The output results are compressed into a one-channel anomaly score heatmap. An anomaly score is

calculated by a global averaging pooling layer as the mean of the output heatmap returned by the network.[200]

Computers “see” colours by assigning digitised normalised intensity values to each pixel. The most common colour model is RGB (*i.e.*, red, green, blue), where each colour is typically represented by 8 bits per colour (or 24 bits in total). All possible combinations are taken as positive integers from 0 to $(2^8 - 1) = 255$ and the colour is specified by 3 numbers (r, g, b). In that system, *e.g.*, white has number (255, 255, 255), while black is (0, 0, 0) and red is (255, 0, 0). The anomaly score calculated by this AI model uses the contrast between each pixel from the image and assigns an overall value (anomaly threshold score (ATS)) for the image. The ATS display range was set to show values between 0 and 80, where white is presented as 0 and black has a value closer to 80. Grey colours get the numbers between 0 and 80 depending on where in the greyscale they fall (closer to the white or to the black end of the spectrum). The ATS value was dependent on the image brightness and bit depth, *e.g.*, 8-bit RGB images with 255 intensity values may well produce different anomaly values than the same images encoded as 10-bit RGB with 1023 intensity values in each of the three colour fields. A depiction of the analysis used in the ATS method is presented in Figure 2.4. The numbers in the figure are illustrative and does not represent the real ATS image analysis.

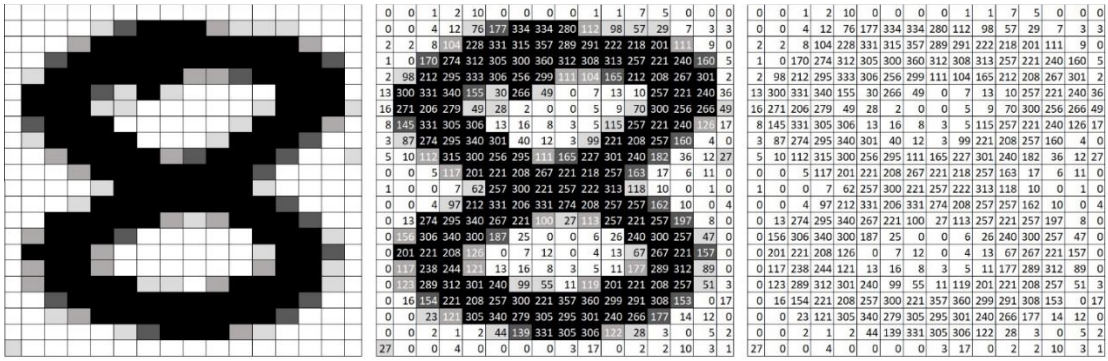

Figure 2.4: CNN image recognition based on anomaly threshold score (ATS) pixel colour intensity.

- **Training:** The model can be trained with a specific image data set, or it can be used with a predefined version of the NN. The training consists of multiple cycles of image examination. The training data set contains 70 random images from the normal class and 1 image from each anomaly class. The CNN reads all images once from the training data set. The output information about its performance is returned as an input into the system. Another 50 cycles are done, and the output is used once again to readjust the sensitivity of the method. As a final step of the training, the system does another 100 cycles. A training file with the system configuration is recorded and can be used directly in a subsequent analysis, *i.e.*, the system is pre-trained to do the anomaly detection. This is the most time-consuming part, taking up to several hours depending on the computational resources available.

- **Calibration:** The calibration set consists of 30 random normal images and 15 random images from each anomalous class. The calibration step is performed before each test. A calibration ATS (cATS) is calculated each time based on the randomly selected images from the calibration set (Equation 2.1). A histogram output chart shows the distribution of all calculated anomaly scores for the calibration set.

Equation 2.1: CNN calibration anomaly threshold score (cATS)

$$cATS = \frac{\sum 15 \text{ x } (ATS\ anomaly\ image) + 30 \text{ x } (ATS\ empty\ image)}{45}$$

- **Testing:** All images that are not used in the training and calibration steps are allocated for testing. The ATS for each image is calculated independently. Images are assigned to a certain class after comparing their ATS to the cATS. The classifier labels the images with 0 to indicate a normal image when the calculated ATS is lower than the cATS and with 1 to indicate an anomalous image when the ATS is above that score. A confusion matrix is

used to display the results, and the classification accuracy for the test set is calculated by using Equation 2.2.

Equation 2.2: CNN accuracy equation.

$$Accuracy = \sum(correctly\ predicted\ images) / \sum(all\ images)$$

The anomaly heat map (see example Figure 2.5) can be used to illustrate why an image is labelled as normal or anomalous and to identify false negative (frame with an anomaly classified as normal) and false positive (normal frame classified as anomalous) patterns. These patterns can assist the identification of strategies for increasing class balancing of the training data or improving the network performance.

Figure 2.5: Output image from the original Matlab™ tablet anomaly detection code. Original image of a chipped tablet (left) and the same image with applied heat map (right) highlighting the area of the anomaly.

2.2.2.2.2. Model development and validation – API

Several changes were made in the original code to develop a model able to identify events occurring in the USP 4 FTA test cell. 1) Images from dissolution and precipitation tests were selected, then extracted from the recorded videos (150 frames per 15 s video) and re-sized to 225 x 225 pixels by an in-house code written in Matlab™. 2)The original tablet image data sets were replaced with appropriate dissolution/precipitation related image sets. Images were divided into two groups – empty/normal (images without particles) and anomalous (images with particles present in the frame). 3) A function calculating percent of predicted empty/without anomaly frames (%FwA) was added to the code. This function was used to investigate the ability of the approach to characterise the dissolution process over time. 4) A new pathway to the data storage with dissolution test images was designed to enable image selection from 2 different sources for testing and calibration (Figure 2.6). A segmentation of the data storage was necessary in order to analyse images from separate time points of the dissolution test without interference of either training data images or images from previous time points.

A schematic presentation of all trainings and tests is shown in Figure 2.7.

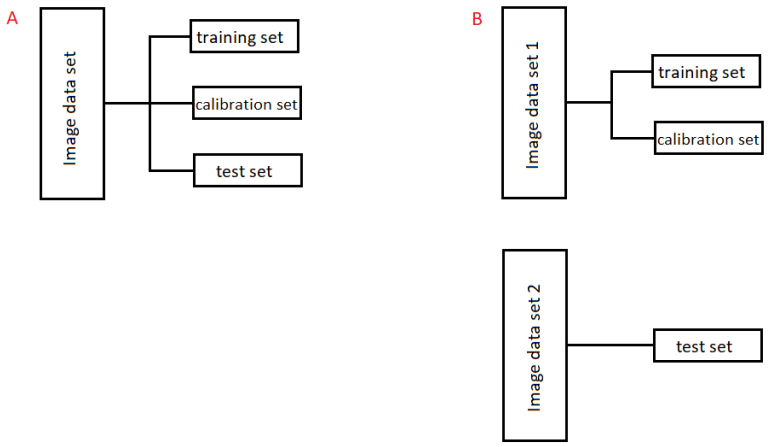

Figure 2.6: Image pathway for validation and training and assessing ability to detect precipitation events (A) and image pathway used for dissolution testing analysis (B). A: The image data set could contain dissolution or precipitation images irrespective of the performed training. B: Image data set 1 could contain dissolution or precipitation images allocated for

training and calibration before testing, while image data set 2 contains only dissolution images for testing.

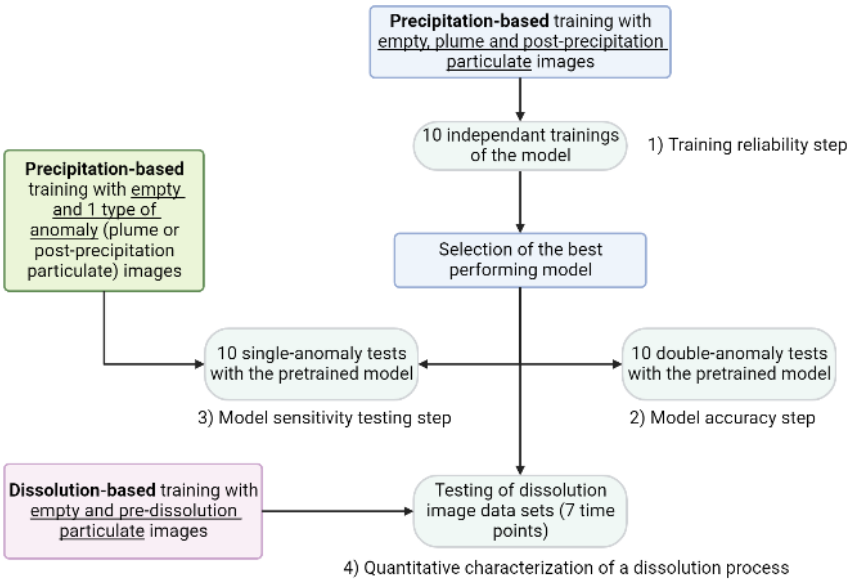

Figure 2.7: Model development and validation – schematic presentation of training and testing methods during each step of the process.

Videos from late time points of the dissolution test (Table 2.2) of ibuprofen in PB 0.05% w/v Tween 20 performed in the USP 4 FTA CE1 were used to extract empty frames (no present particles) (Figure 2.8 A) and used to generate the empty ("normal") image data set. As described in Chapter 2, section 2.2.1.4.1 (Precipitation in the USP 4 FTA), when the dissolution test was finished after 160 min the medium was changed with 0.1 N HCl solution to cause precipitation of ibuprofen. Videos from the first 5 min of the precipitation were used to extract frames with plume (Figure 2.8 B) and to generate the plume (anomaly) image data set. Later, when newly formed particles (Figure 2.8 C) were noted, videos capturing them were used to compose the particle (anomaly) data set. Images were divided into two groups – "normal" and "anomaly". The existing image sets were replaced with 132 "empty" frames, 135 images with plume and 102 images with pre-dissolution or after precipitation particles.

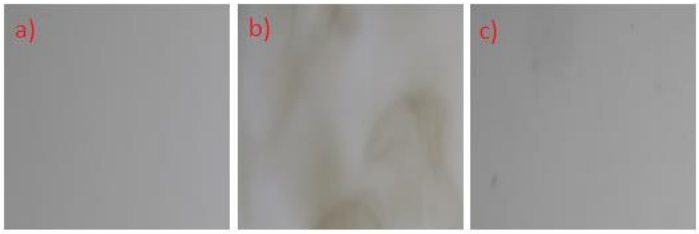

Figure 2.8: A) empty ("normal") image; B) image with plume; C) image with precipitated particulates.

Two different data sets were prepared for model training and testing to explore the influence of the data sets on the accuracy and sensitivity of the resulting models.

- **Precipitation-based data set:** The three newly created image data sets were used for model training and validation. Images from the 2 anomaly types were used in combination (double-anomaly) or separately (single-anomaly) to test the model accuracy. Small particles (Figure 2.8 C), which were slightly darker than the background, were used to train the model to detect small changes occurring in the test cell.

- **Dissolution-based data set:** The dual pathways (Figure 2.6 B) for accessing image data sets were used to allocate training images and test images. Therefore, 9 new image data sets were created from dissolution test videos – 2 for training and 7 for testing. Videos from the dissolution test of 20 mg ibuprofen in PB 0.005% w/v Tween 20 at FR 16 mL/min were used. All videos were manually investigated for presence of particles.

    - Training set: After the dissolution was completed, a video from the last time point (120 min) was used to create the new “normal” (empty) image data set. An early time point video (6 min) was used to create the training “anomaly” set, as all images contained particles.

    - Test set: The test time points were chosen to contain a) many particles present (2 and 15 min); b) mixed frames – with and without

particles (40, 50 and 60 min) and c) only empty frames (80 and 100 min).

Training and calibration steps were kept as per the original model description. Depending on the model (dissolution- or precipitation-based) the access to the test images was through single or dual pathway as described earlier (Figure 2.6). Test images in both cases were not used for training or calibration (training step was omitted when a pre-trained model was used; calibration step was performed before each test regardless of the training). When the precipitation-based model was used, images were selected from the same data set as the calibration images. On the other hand, test images represent a single dissolution time point and each set contains 150 images from a single video when the dissolution-based model was used. Therefore, the designated test images can be tested regardless of the calibration and/or the pre-trained model used. In this way the system classifies the new images (from a video taken at a new time point) without a bias from previous time points/test sets.

- **Training reliability:** To test the reliability of the training method, 10 separate trainings of the system were carried out with the same precipitation-based image data set. The remaining images unused for training and calibration from the data set were evaluated and classified based on their ATS. The model calculated the accuracy of each test. The results from all 10 tests were compared and the best performing model based on the highest accuracy was chosen for further testing.

- **Pre-trained model repeatability:** To test the repeatability of the model, ten tests were carried out with the pre-trained model chosen from the previous step and the same precipitation-based image data set. Hence, the training step was omitted. The average accuracy of all tests was calculated (Figure 2.7).

- **Model sensitivity:** To test the model sensitivity, two pre-trained models were used. One trained by using double-anomaly data (plume and particles) and another trained with a single-anomaly data where all images with either plume or particles were included or excluded as relevant. Ten tests were

conducted with each pre-trained model. The accuracy of the three pre-trained models (double-anomaly, plume single-anomaly and particle single-anomaly) was compared (Figure 2.7).

- **Model image size sensitivity:** The size sensitivity of the model, *i.e.*, the detectability of anomalies at different image resolution was tested. All images from the training data set (empty, plume and particles) were re-sized from the original 1920x1200 pixel size to 150x150; 225x225; 255x255 and 450x450 pixels. A built-in function for image rotation required images to be squares, thus the system can rotate them at 90° during testing. The model was re-trained with each resized set to test the system performance when the image quality is changed, *e.g.*, at low pixel number. Results of this test are presented in Chapter 4.

- **Quantitative characterization of a dissolution process over time:** To characterize the dissolution process, both pre-trained models (dissolution- and precipitation-based) were used. Test images from 7 dissolution time points (2, 15, 40, 50, 60, 80 and 100 min) were used. The system was trained to recognize particles and classify them as anomalies. Therefore, frames without an anomaly will be classified as "normal", *i.e.*, without particles present in the frame. The hypothesis being tested was that early in the dissolution test most or all frames would contain particulates, *i.e.*, anomalies, and later in the dissolution test when the drug is dissolved, all frames will be empty. Results from each image set tested were therefore expressed as percent frames without anomaly (%FwA) (Equation 2.3) and compared to a manual classification of the frames (empty or particulates) to confirm the model accuracy. Then the %FwA was compared with the percent dissolved drug at the current time point to assess the ability of the approach to characterise the dissolution process over time.

Equation 2.3: CNN percent frames without anomalies

$$\%FwA = \frac{\Sigma(number\ of\ predicted\ class\ empty\ images)}{\Sigma(number\ of\ test\ images)} \times 100$$

2.2.2.2.3. Model development and validation – suspension formulations

This model was trained to detect only one type of anomaly – suspension/particles. A sensitive formulation-based data set was created by assigning 200 empty images from the dissolution test after the suspension was fully dissolved and 283 images in which single particles of the suspension were still visible (late stage of the dissolution test) to be used as anomalous. As the suspension components refract the light, they appear darker than the background. Images from early dissolution time points had high ATS, thus they were easily classified as anomalous, since the images used for training and calibration had lower ATS values.

To describe the dissolution process quantitatively and qualitatively over time, two approaches were exploited – %FwA and percent average anomaly threshold score (%avgATS).

- The %FwA was calculated automatically for each dissolution time point via the build-in function described earlier. Results were compared with the related dissolution profiles.

- Each frame has a unique ATS value calculated based on the pixel brightness of an image. The average ATS value ($avgATS_x$) per dissolution time point (x) was calculated. When the dissolution test is finished and all $avgATS_x$ values are known, the highest avgATS is determined ($avgATS_{max}$). Then the %avgATS for each dissolution time point is derived by using Equation 2.4. Results were compared with the related dissolution profiles.

Equation 2.4: CNN percent average anomaly threshold score (ATS) calculated per dissolution test.

$$\%avgATS = (avgATS_{max} - avgATS_x)/avgATS_{max} \times 100\%$$

Chapter 3: Investigation of the discriminative power of shadowgraph imaging during dissolution testing under various conditions in the USP 4 flow-through apparatus and the development of an automated image-based agglomeration identification method (AIM) to detect agglomerates occurring during dissolution

Results, discussion, and conclusions presented in this Chapter have been published in: Taseva A.R., Persoons T, Healy AM, D'Arcy D.M. Application of shadowgraph imaging (SGI) particle characterisation data to interpret the impact of varying test conditions on powder dissolution and to develop an automated agglomeration identification method (AIM) in the USP flow-through apparatus. Int J Pharm. 2024 Dec 5; 666:124778. doi: 10.1016/j.ijpharm.2024.124778. Epub 2024 Sep 28. PMID: 39349225.

3.1. Introduction

Physical and chemical properties of APIs are central to dissolution performance. There are several strategies that could be used to enhance the dissolution rate such as reduction of particle size and thus increasing the surface area, replacing the API with a more soluble salt form, in the case of formulations, excipients which improve the drug

dispersal in the medium, *e.g.*, disintegrants could be added.[201] Using salt forms instead of free base/acid of poorly soluble drugs is a common practice due to their higher solubility and improved physicochemical and mechanical properties. Salt formations are a preferred alternative as they could reduce drug toxicity and could alter the absorption in the GI tract.[38], [202] However, often the salt with the highest solubility does not represent the best choice due to other factors such as stability, supersaturation and precipitation potential.[202]

Strategies such as size reduction, co-crystallization, crystal habit modifications, 3D printed formulation and changes in the dissolution medium composition (addition of co-solvents and surfactants) have been used to improve ibuprofen *in vitro* test performance and thus to ensure drug product quality and performance.[35], [40], [41], [93], [203]–[206]

Ibuprofen has poor water solubility (BCS Class II) and needle-like crystal shape. Due to its typical crystal habit, ibuprofen shows poor flow properties, low compressibility and a tendency to stick to the punches during compression.[35] Agglomeration of APIs could be beneficial during formulation development as they can improve powder flowability and compressibility.[41], [65] On the other hand, agglomerate formations during dissolution would reduce the surface area available for dissolution, hence a lower dissolution rate could be observed.[74], [94], [207] Agglomerates formed during crystallization or present in the final drug product could be considered as impurities, could have negative impact on product stability, particle dispersal and they could change dissolution behaviour as well as bioperformance.[64], [208]–[210]

In this Chapter, the aims were 1) to investigate the effect of medium composition changes such as surfactant addition and FR change and the effect of drug mass and crystal habit on the dissolution rate of ibuprofen powder through the use of an in-line SGI and analysis to capture differences in particle dispersal and behaviour which could give an insight into how these conditions impact the particle behaviour and dissolution process; 2) to develop an automated AIM to detect presence of agglomerates formed during dissolution in the USP 4 FTA by further exploit SGI analysis.

3.2. Material and methods

All materials used for this work were described in Chapter 2, section 2.1 (Materials). Dissolution medium was prepared as described in Chapter 2, section 2.2.1.1.1. To characterize the API powder methods sections 2.2.1.2.1 to 2.2.1.2.4 were used. All dissolution tests were performed in the USP 4 FTA as described in section 2.2.1.3.1. Samples were analysed by UV analysis as per section 2.2.1.5.1. Image acquisition and analysis were performed by SGI, described in section 2.2.1.6.1. Ibuprofen plate-shape crystals were prepared by Dr. J.Yadav (see acknowledgments) by cooling crystallization method (CCM) described in Chapter 3, section 3.2.1.

3.2.1. Preparation of plate-shaped ibuprofen particles (Ibu-pl)

Preparation of Ibu-pl is only briefly described here as the crystals were produced by Dr. J. Yadav by a CCM. Ibu-nd was dissolved in 100 mL of hexane at a concentration of 0.14 g/mL and heated to 75°C. Supersaturation was achieved by cooling of solutions using a glass-jacketed vessel (Reactor Ready system, Radleys, UK) with chiller unit (Huber Ministat 125 Pilot one controller, UK). Two cooling rates were used – 6.5°C/min until 10°C and 0.12°C/min between 10 and 5°C. Crystals were collected by vacuum filtration and dried at room temperature.

3.3. Results and discussion

3.3.1. Dissolution testing and SGI imaging analysis

3.3.1.1. Effect of surfactant concentration, drug quantity and flow rate on the dissolution rate

The addition of surfactant to the medium had a minor effect on the observed solubility of ibuprofen. The measured solubility was 3.69 (±0.03) mg mL^{-1} (PB + 0 % w/v Tween 20); 3.71 (±0.18) mg mL^{-1} (PB + 0.005% w/v Tween 20) and 3.95 (±0.09) mg mL^{-1} (PB + 0.05% w/v Tween 20). On the other hand, the change of the dissolution rate in the media with 0.005% w/v or 0.05% w/v Tween 20 was notable (Figure 3.1). Differences were also noted when different drug mass was used for dissolution. The lowest mass used (4 mg) dissolved within 20 minutes of the test in all conditions, except at the lowest FR in PB 0% w/v Tween 20. The other two tested masses (20 and 100 mg) resulted in slow dissolution in 0% w/v Tween 20, slightly faster at 0.005% w/v Tween 20 and very rapid (20 mg) in 0.05% w/v Tween 20.[7], [52] The 100 mg ibuprofen showed slow dissolution at FR 8 mL/min and rapid dissolution at 16 mL/min. Therefore, it was hypothesised that the impact of dissolution conditions on observed dissolution rates was due to differences in particle dispersal.

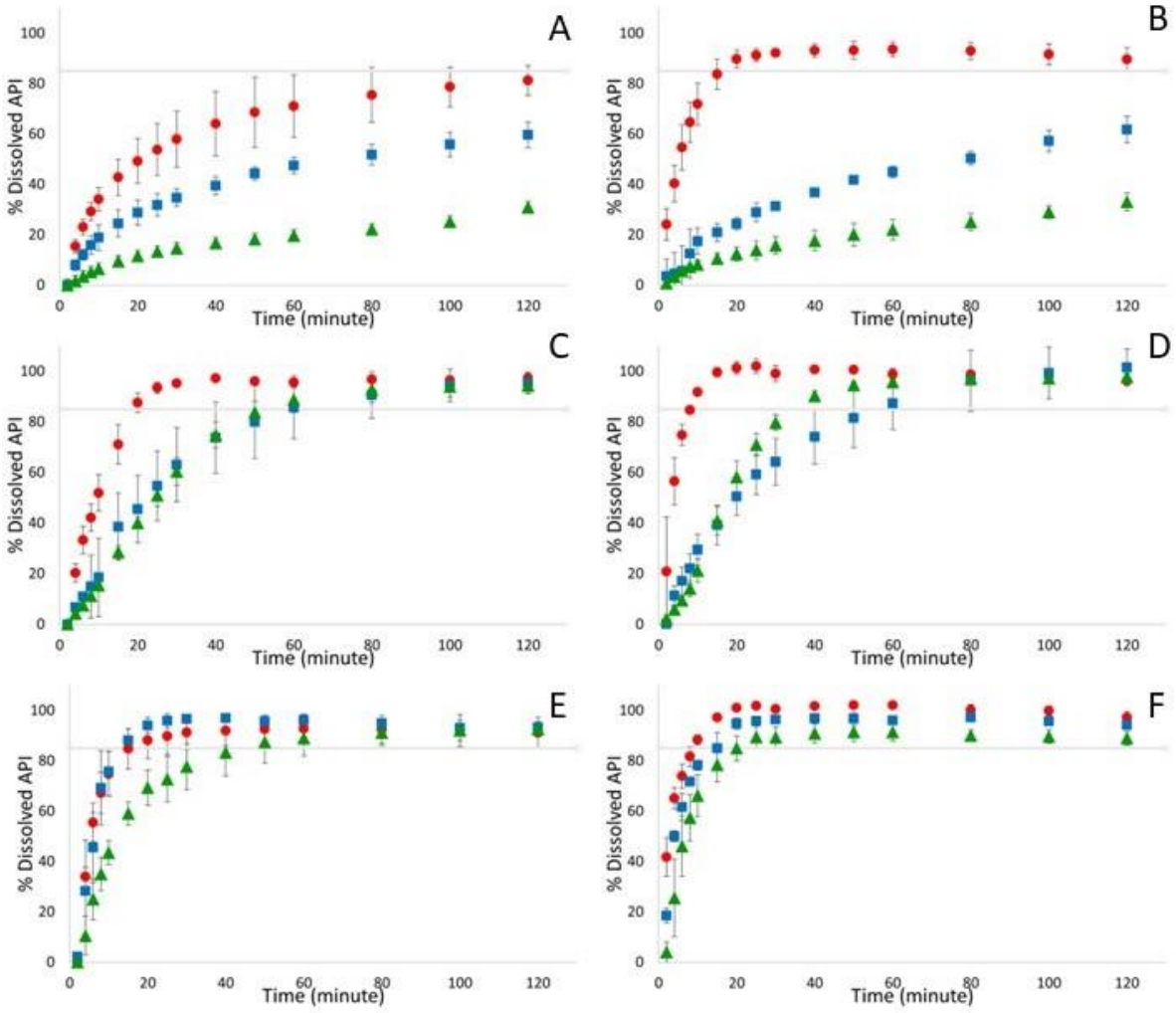

Figure 3.1: Dissolution profiles of 4 mg (red circle), 20 mg (blue square) and 100 mg (green triangle) Ibu nd powder in phosphate buffer pH 6.8 with 0% w/v (A, D), 0.005% w/v (B, E) and 0.05% w/v (C, F) Tween 20 at FR 8 (left column) and 16 (right column) mL/min in the USP 4 FTA CE7 22.6 mm diameter cell. The grey line represents the level of 85% dissolved drug.

Several factors can contribute[1], [211], [212] to the reduced dissolution when there is a higher drug loading in the cell such as reduced contact area (due to clumping), a limited instantaneous medium volume in the test cell, poor mixing and poor wetting of the drug powder. A change in the FR did not notably affect the dissolution rate. An increase was noted when a smaller drug mass of the powder (4 mg) was used and no surfactant was added to the medium (Figure 3.1 A and D, red circles), and when a higher surfactant concentration (0.05% w/v Tween 20) and drug mass (100 mg) were used (Figure 3.1 C and F, green triangles).

3.3.1.2. Application of SGI analysis to detect changes in the drug dissolution behaviour under various dissolution conditions

The SGI set-up has a small detection window (7x11 mm^2) which does not cover the whole volume of the test cell; it is positioned in the centre of the cell and therefore only dispersed particles are captured. Individual particle trends would not be accurately detected if glass beads or a bed of sedimented particles on the beads were to be included in the image, as the SGI detection is based on light contrast. Therefore, it would not be able to distinguish the sedimented particles from each other in a sedimented mass or distinguish the particles from the bed of beads. When particles were lifted from the bottom of the cell during dissolution, they crossed the imaging window, hence they were detected. The results from the dissolution tests in USP 4 FTA CE1 are presented in Appendix 2. Most of the profiles from both dissolution sets (CE1 and CE7) were broadly comparable, except for some instances of the medium containing 0.005% Tween (where generally CE1 results were slower). However, the observed dissolution rank order and trends were similar. SGI reflecting the dissolution conditions in the USP 4 FTA CE1 are presented in Figure 3.2A and B.

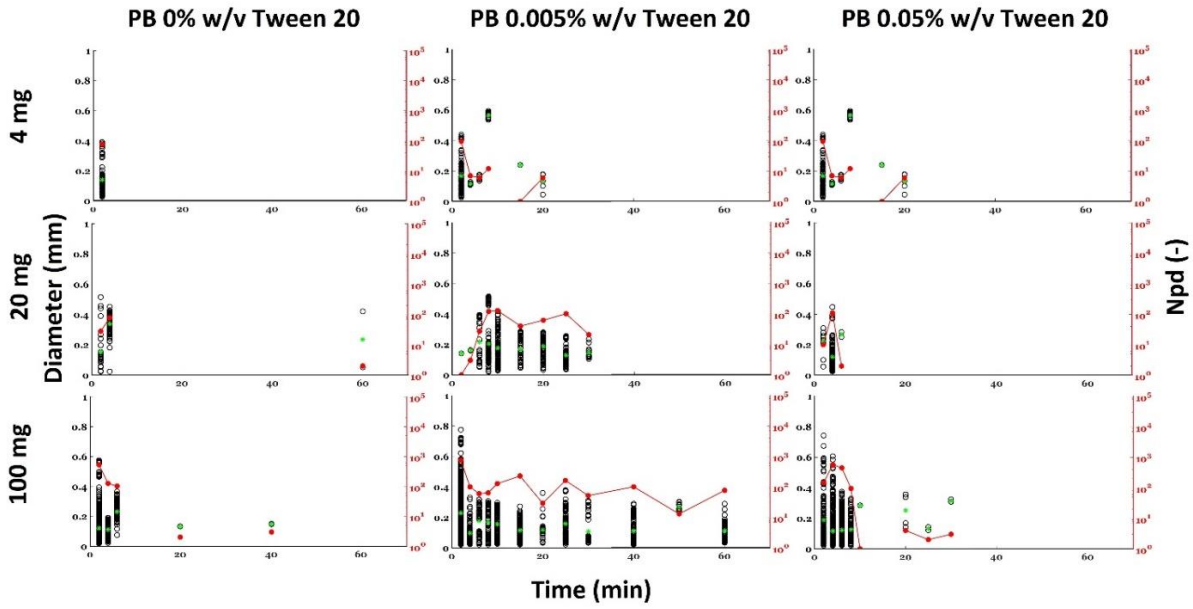

*Figure 3.2A: Number of particle detections (Npd), particle diameter distribution (black circles) and average particle diameter (green star) of ibuprofen 4 (top), 20 (middle) and 100 mg (bottom) detected by the shadowgraph imaging during dissolution testing in the USP 4 FTA (CE1) in PB with 0% (left), 0.005% (middle) and 0.05% (right) w/v Tween 20 at FR 8. O (black) – single particle size (left axis); * (green) – average size (left axis); dots and line (red) – number of particle detections (Npd) (right axis).*

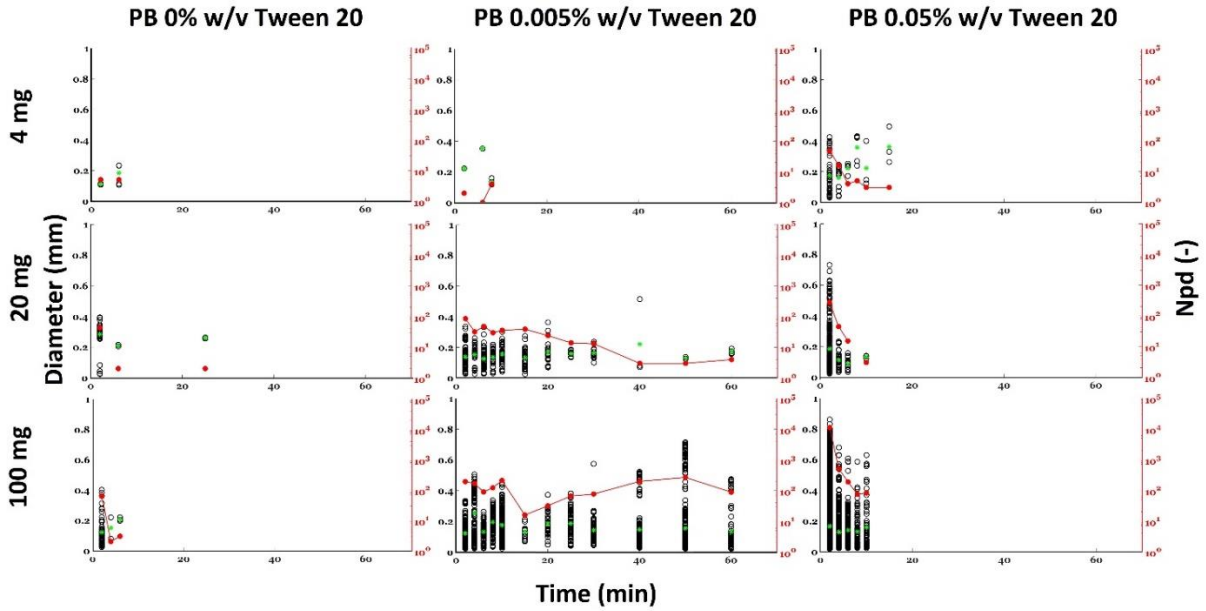

*Figure 3.2B: Number of particle detections (Npd), particle diameter distribution (black circles) and average particle diameter (green star) of ibuprofen 4 (top), 20 (middle) and 100 mg (bottom) detected by the shadowgraph imaging during dissolution testing in the USP 4 FTA (CE1) in PB with 0% (left), 0.005% (middle) and 0.05% (right) w/v Tween 20 at FR 16. O (black) – single particle size (left axis); * (green) – average size (left axis); dots and line (red) – number of particle detections (Npd) (right axis).*

In PB with 0% w/v Tween 20 few particles were detected after the early timepoints. This suggested minimal dispersal, correlating with the slowest observed dissolution results for all masses in this medium. In PB with 0.005% w/v Tween 20, particles were better dispersed and detected for longer. Results showed prolonged particle detection at the lower flow rate. In PB with 0.05% w/v Tween 20 a high number of particle detections were observed at early time points, which correlated with the very rapid dissolution in this medium. High particle detections (first 5 min) suggested better particle dispersal in this medium compared to PB with 0% w/v or 0.005% Tween 20. Particles were detected for a slightly longer time in PB 0.05% Tween 20 when the mass used for dissolution was increased, like the results in PB 0.005% w/v Tween 20. These observations supported the hypothesis of increased dispersal resulting in a higher dissolution rate in this medium, with mass present in the test cell influencing the observed trends without a major change of the solubility.

3.3.1.3. Application of SGI analysis to characterize the dissolution of different crystal forms of ibuprofen – plates and needles

Ibu-pl-S and Ibu-nd-S were observed by optical light microscopy at room temperature, which revealed two crystal shapes – plates and needles for Ibu-pl and Ibu-nd, respectively (Figure 3.3).

The same mass (20 mg) of sieved (Ibu-pl-S, Ibu-nd-S) and un-sieved (Ibu-nd) ibuprofen was used in dissolution testing. Results from the dissolution tests in the USP 4 FTA CE7 are presented in Figure 3.4. Results from the dissolution tests in USP 4 FTA CE1 are presented in the Appendix 2. Dissolution results showed similar trends and dissolution rates in both (CE1 and CE7) set ups, apart from a lower dissolution rate of Ibu-nd-S in the CE1 at the lower FR. The SGI results relating to the dissolution profiles in the USP 4 FTA CE1 are presented in Figure 3.5. The two sieved fractions showed faster dissolution rate than the un-sieved fraction of Ibu-nd. This suggested an effect of the particle size on the dissolution process. Particle size analysis of the un-sieved ibuprofen particles showed size distribution of Dv10 = 42.94 µm, Dv50 = 162.50 µm, Dv90 = 542.97 µm, while the sieved fractions had particle size ranging from 100 to 306 µm. The presence of larger or smaller particles could affect the particle dispersal and thus SGI detections. Heavier particles would settle on the bottom of the cell (under the imaging window) while lighter particles would move above the imaging window and thus, they would not be detected. In the sieved fractions, more particles potentially fall into the SGI detectable size range for these conditions and may be present in the detection window for longer at the higher flow rate. However, particle size analysis based on laser diffraction could be performed with the sieved fractions to determine differences and similarities between them and the un-sieved fractions and thus, to evaluate the potential impact of sieving on the dissolution studies. Several studies discuss the crystal habit of ibuprofen crystallized in different polar and non-polar solvents by using CCM, a solvent-evaporation method or anti-solvent crystallization method.[35], [93], [213] Both Khan *et al.* and Rasenack *et al.* reported the effect of the solvent polarity on the crystal shape.[35], [213] They showed that more polar solvents, such as methanol, form more regular shaped crystals (spherical, cubic) and less polar

solvents like acetone and hexane – form more elongated crystals (needles). Garekani *et al.* found that the needle-shaped crystals demonstrated worse flowability and compressibility compared to plate-like crystals.[93] On the other hand, Rasenack *et al.* observed that there was no significant difference in the dissolution profiles of both crystal habits.[35] In the current work, Ibu-pl-S shows the highest number of detections in the first 20 min of each test and the fastest dissolution rate when all other conditions were the same. The dissolution results suggest agreement with other publications[35], [93], [213] where a more regular crystal shape increases the dissolution rate.

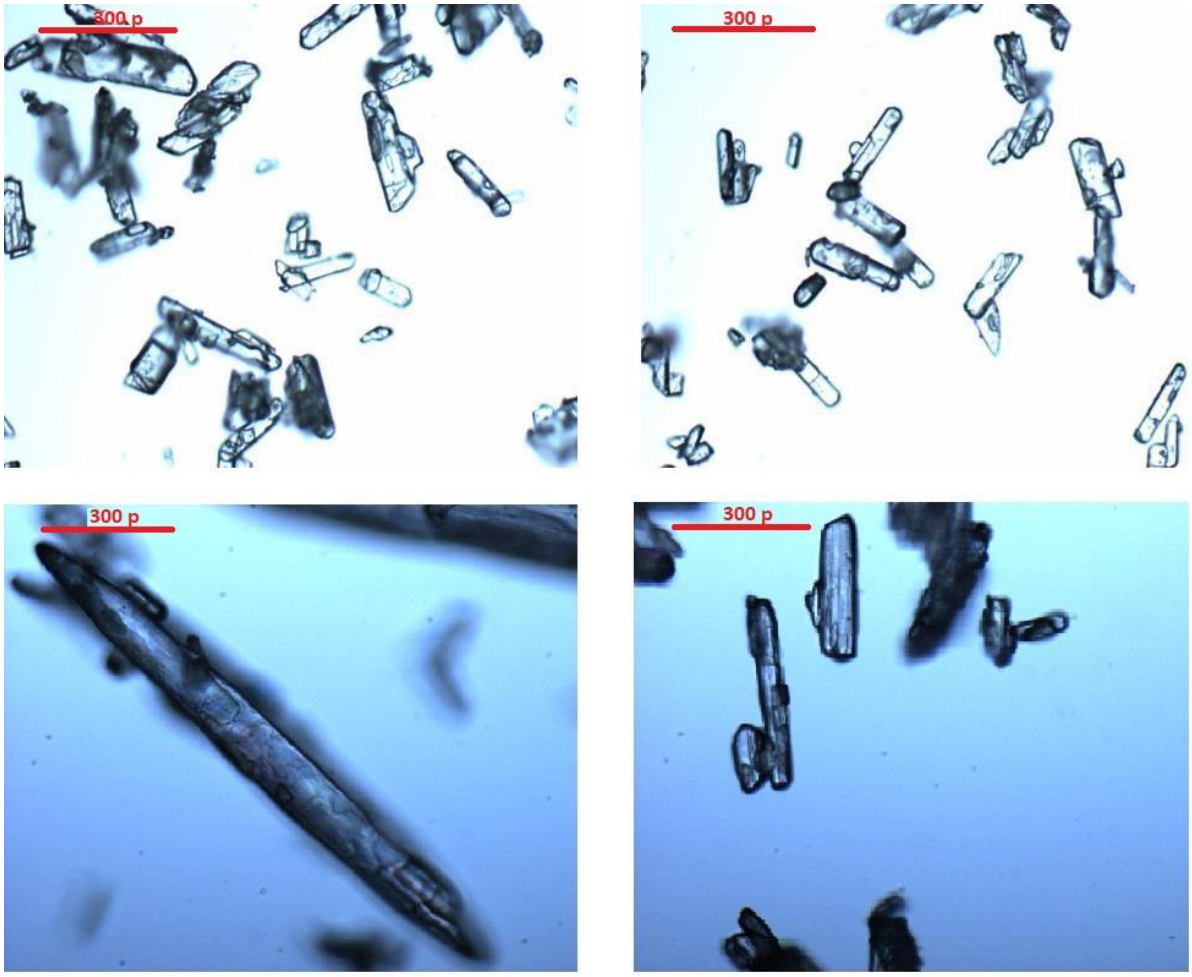

Figure 3.3: Microscopic images of Ibu pl (top) and Ibu nd (bottom) at 20X magnification.

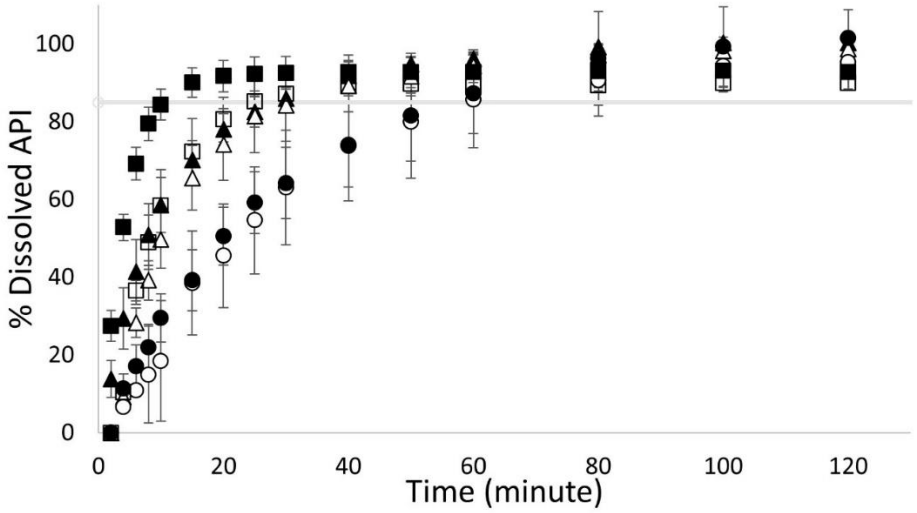

Figure 3.4: Dissolution profiles of Ibu pl S (squares, □), Ibu nd S (triangles, Δ) and Ibu nd (circles, ○) in the FTA CE7, test cell 22.6 mm diameter at FR 8 (white) and 16 (black) mL/min. Medium: phosphate buffer with 0.005% Tween 20, pH 6.8.

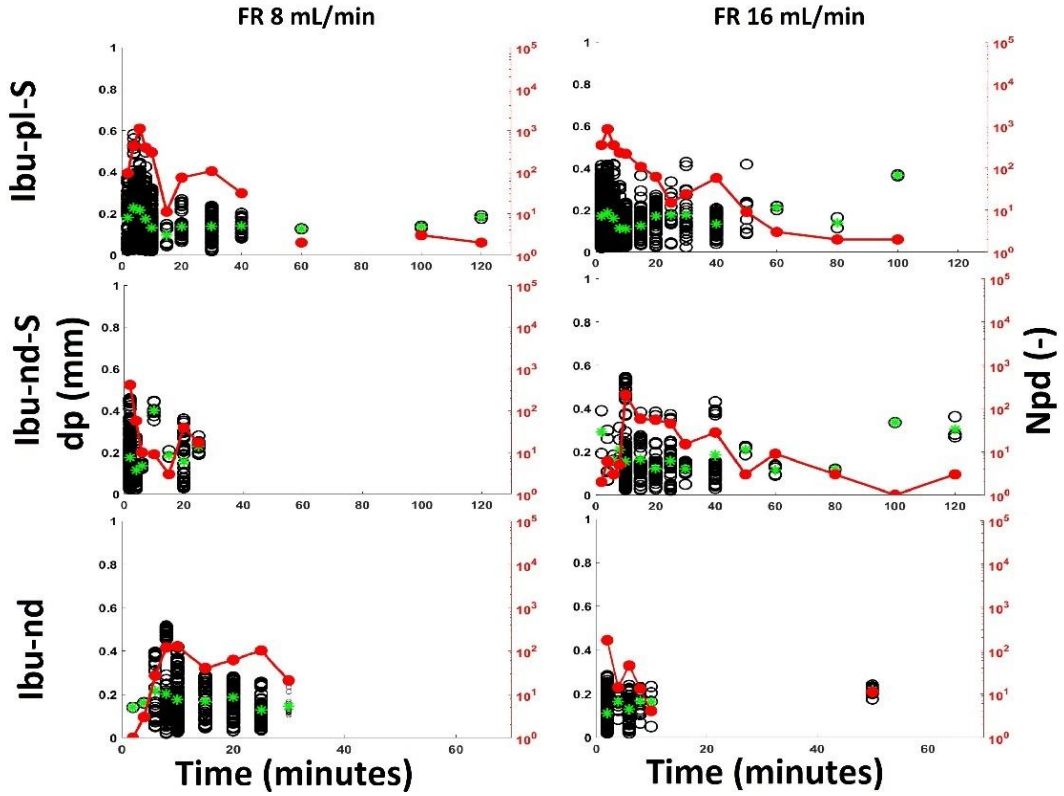

*Figure 3.5: Number of particle detections (Npd), particle diameter distribution (dp) and average diameter (green star) of Ibu pl S, Ibu nd S and Ibu nd, 20 mg detected by the shadowgraph imaging during dissolution testing in the FTA (CE1) in PB 0.005% w/v Tween 20 at FR 8 and 16 mL/min. O (black) – single particle size (left axis); * (green) – average size (left axis); dots and line (red) – number of particle detections (Npd) (right axis).*

Apart from the crystal habit, another hypothesis that could explain the differences between the dissolution profiles of Ibu-pl and Ibu-nd observed in the current work was a difference in their agglomeration tendency. Manual analysis of the videos resulted in agglomerates being found for all ibuprofen fractions (Figure 3.6). Groups of 2 or more particles moving together during the dissolution were visible at early time points for Ibu-pl-S (< 15 minutes) and even at later time points (> 40 minutes) for Ibu-nd-S. The presence of agglomerates at later time points suggested that a smaller surface area was exposed to the medium, which could slow the dissolution. Ibu-nd (needle-shape crystals) were found to form agglomerates of particles attached at their tips, frequently with a specific "V" shape. The difference in the formed agglomerates may also contribute to the lower dissolution rate observed for Ibu-nd (both sieved and un-sieved) compared to Ibu-pl-S. The particles included in the Ibu-pl-S agglomerates looked smaller and dissolved faster (they were not observed in images from later time points). Maghsoodi *et al.* also reported a negative impact of agglomerates formation during dissolution of ibuprofen-PVP co-crystals in comparison with the pure API.[203] In the current work, the negative effect of the agglomerate formation could be suggested by the slower dissolution profile of Ibu-nd-S compared to the Ibu-pl-S, especially at the higher FR (Figure 3.4).

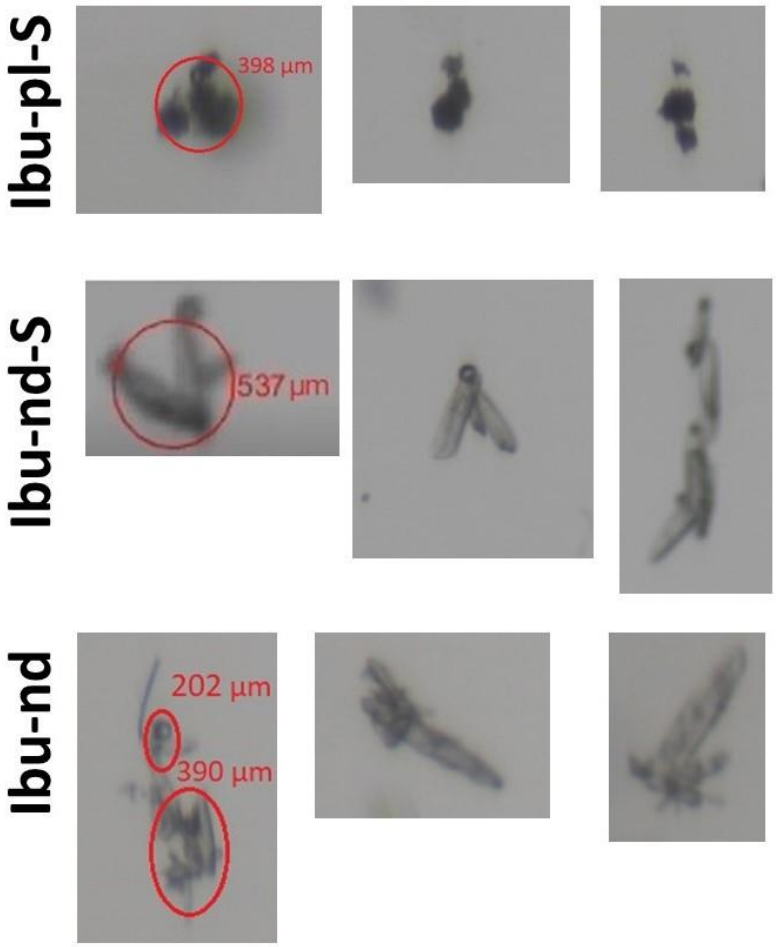

Figure 3.6: Examples of ibuprofen agglomerates found by the SGI during dissolution testing (USP 4 FTA) in PB. The red circle surrounding the particle is produced after image analysis in Matlab™ and shows the particle diameter in micrometres (red number).

Imaging could be used to observe agglomerations occurring during dissolution testing, but processes like manual recording of occurrence time for example, could result in a slow, tedious task, especially for long or multiple recordings. Therefore, the SGI could be used for further data processing. Development of an automated method for agglomerate detection could reduce the time required for manual analysis. The following section presents an approach to develop an automated computational model able to compare parameters characterising agglomerates, supporting automated image-based agglomeration detection.

3.3.2. Agglomeration Identification Method (AIM) development

The AIM was developed in 4 main steps, as described in the Methods section.

Step 1, Reference Image Data Set: Manual observation of the videos from Ibu-pl-S and Ibu-nd-S (150 frames per video) revealed up to 30 agglomerates in each video (5 – 20% of all detections per video), with many of the agglomerates present in multiple successive frames, equivalent to approximately 100 – 150 potential agglomerate detections.

Step 2, Performance Evaluation (Sensitivity): The combined criterion with exact size (> 300 µm) and solidity (< 85%) values, was successful in flagging only agglomerates with a large size and low solidity, typical for Ibu-nd-S, *e.g.*, with a "V" shape (Figure 3.6). In contrast, when the size criterion was set above the mean diameter for the current test set, it resulted in many false positive signals being generated. A very low solidity criterion (≤ 10% – ≤ 30%), failed to detect most of the agglomerates. The average solidity for Ibu-pl-S was calculated to be > 90%; hence higher solidity cut-off criteria (*i.e.*, Solidity ≤ 96% or Solidity ≤ Pr75) were more successful. The three best performing combinations that captured all agglomerates were 1) Diameter ≥ Mean / Solidity ≤ 96%; 2) Diameter ≥ Pr75 / Solidity ≤ 96% and 3) Diameter ≥ Pr75 / Solidity ≤ Pr75 as they captured all agglomerates present in the test videos. The combination of Diameter ≥ Mean and Solidity ≤ 96% flagged even small agglomerates, which were missed by other tested criteria combinations. However, a high solidity criterion (Solidity ≤ 96% or Solidity ≤ Pr75) potentially includes many single particles due to the high cut-off value. A high solidity criterion used in combination with a low size criterion (Mean diameter) leads to a high number of detections and many false positive results (up to 45%). When plotted, these overlapping flags, representing agglomeration signals (upper green stars in Figure 3.7), make it difficult to distinguish true from false signals. An important feature for both manual observation and automated detection is the number of particles per video. Videos with many particles are challenging due to particles overlapping with each other on the frame; thus the system can count them as

one bigger particle (agglomerate).[214] On the other hand, when percentiles are used as the detection criteria, there will always be false positive results with low particle numbers as, by definition, some particles must meet the agglomerate detection criteria, even if they are individual particles. In that case, if the solidity of these single particles is below the chosen limit they would be falsely classified as agglomerates. For this data set 10 – 20 particles per frame was the optimal particle number – sufficient for manual agglomerate identification to be feasible along with low detection system errors.

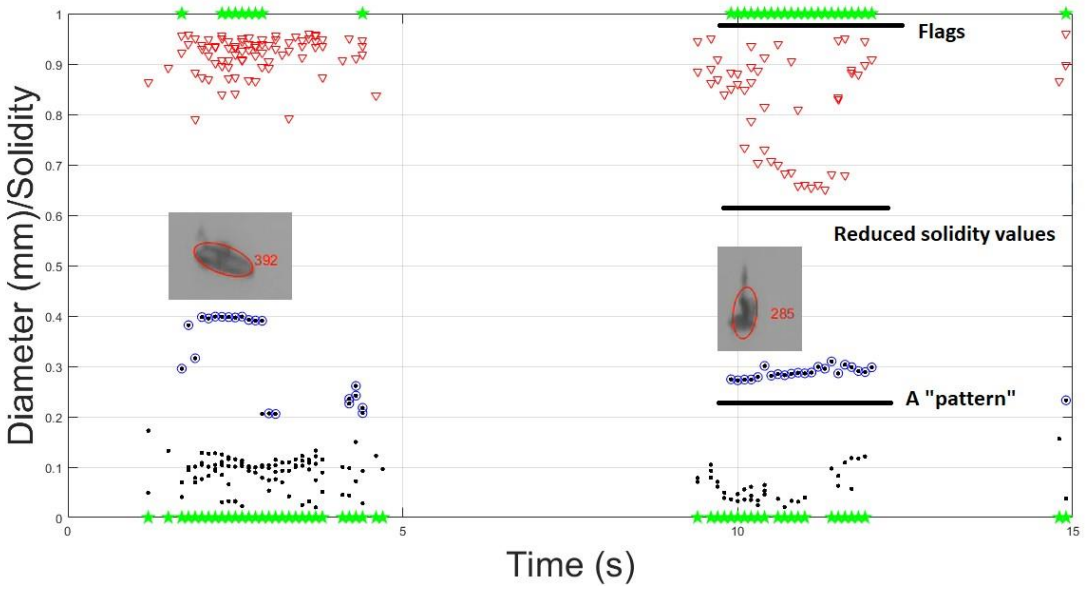

Figure 3.7: Sample particle and agglomerate detections from a 15 s video, external validation. Particle detections (black dots), particle detections that meet the size criteria (blue circles), a "pattern" – series of particle detections representing agglomerates, particle detections that meet the solidity criteria (red triangles), signals indicating timepoints when both specified criteria have been met (green stars at 1 (top of image)) and signals when only one criterion is met (green stars at 0 (bottom of image)), and agglomerates observed in the video at signalled time points with the detected diameter in µm (red circle and number on the grey image).

Step 3, Refined Performance Evaluation (Specificity): The three successful combination criteria from step 2 (highlighted in Table 2.3) were tested on a dataset from Ibu-nd. They were assessed on 1) whether they were able to capture all known agglomerates and 2) the percentage of false positive signals. The results from Diameter ≥ Pr75/ Solidity ≤ 96% and Diameter ≥ Pr75/ Solidity ≤ Pr75 were similar as the top 25 percentile solidity were in the range of 94 – 97%. Based on the generated false positive signals, the best performing combination criterion was Diameter ≥ Pr75/ Solidity ≤ Pr75, with 5 – 12% false positive signals. Diameter ≥ Pr75/ Solidity ≤ 96% showed 10 – 20% false positives and Diameter ≥ Mean and Solidity ≤ 96%, above 20%. For one of the datasets 3 agglomerates were missed by all tested combinations due to their small size (< 150 µm), which was near the average particle size for the current dataset.

Step 4, External Validation: This step involved external validation of AIM based on new Ibu-nd dissolution data. Videos were manually observed, and a reference agglomeration record was created. The combined Diameter ≥ Pr75/ Solidity ≤ Pr75 criterion successfully captured all agglomerates, except for 3 particles with size < 150 µm (particle size below the 75th percentile for the dataset). Agglomerates with certain characteristics (*e.g.* small size) were rarely undetected with this method, however, this should be considered for method development in other systems if such agglomerates might be more likely to occur. False positive results were calculated in cases when particle detections were 150 – 170 per video and the generated signals were ≤ 30. The false signals were < 10%, which correlates well with the false rate observed in step 3.

The false positive results were observed when detections were < 25 or an air bubble passed through the test cell. Air bubbles could be easily recognized during manual video observation due to their specific characteristics – a dark edge and a bright centre. They move faster than the particles and only upward through the test cell. Agglomerates on the other hand have an irregular shape. Examples are shown in Figure 3.6. Three AIM features can be used to confirm the presence of agglomerates – a raised flag (top green stars in Figure 3.7), a drop in the solidity (red triangles, Figure 3.7), and a “pattern” formed by the agglomerate. The pattern is a line of detections of a similar size as the agglomerate moves through the successive frames.

Other similar work in this field has considered the use of an automated data analysis tool for qualitative analysis or object detection and characterization during crystallization and it has been suggested that a similar optical analysis could be of significant importance for digital design approaches and could find many applications in early process development.[106], [145], [215] A broad variety of imaging techniques has been used in order to investigate particle size, shape and behaviour over the last 20 years.[64], [106], [129], [145], [160], [216] Imaging methods such as SGI and microscopy[217] can give more information when comparing different dissolution conditions and/or time points. There are several advantages of imaging methods compared with traditional analytical methods such as UV and HPLC.[217] Imaging does not require sample preparation, expensive equipment or handling chemical substances. Digital recordings of the experiments can be stored and analysed at a later time without a risk of chemical degradation or reaction. The only considerations are the storage space and processing power needed.

As presented in this work, SGI of the dissolution process could be used for dynamic imaging and does not require a probe, which makes it a suitable imaging technique to be used in combination with the USP 4 FTA to give extra visual information about particle behaviour during dissolution testing. By using video post-processing analysis important features were extracted from the videos in real time such as, but not limited to, number of detections and size. The insight provided by SGI (and AIM) is useful to explain differences in dissolution profiles obtained when different medium compositions were used. Furthermore, the appearance of unwanted phenomena such as air bubbles and agglomerates can be detected. SGI could be used for in-line, real time measurements and image analysis in routine quality control testing. It could reduce the need for acquisition of physical samples and thus reduce the time required for off-line sample analysis. Furthermore, an automated method like AIM could be useful for identifying suitable frames to create a training image database while eliminating the lengthy manual image identification steps described in Chapter 2, section 2.2.2.2.1. It is possible for AIM to be included as a pre-step into an AI-based classification model for image-based event detection such as particle detection during crystallization, detection of bubbles or precipitation formations. The same video

acquisition set-up was used to capture precipitation events and for quantitative and qualitative dissolution characterization described in detail in Chapter 4. In this case, of a frame-by-frame investigation, rather than particulate classification. Furthermore, both SGI and AIM can be used to give insight about differences into deviating results or used to confirm similar particulate behaviour in routine testing. As the AIM methodology is newly developed, further development and validation would be needed to prove its applicability in different situations, such as more complex systems or different agglomeration tendency. However, results presented in this work show undeniable potential that this technology could provide in a routine quality control set up.

A limitation of the SGI that should be noted is the single dissolution (CE1) test set-up. All dissolutions were done in parallel in the USP 4 FTA CE1 (single dissolution) and CE7 (triplicate). In future developing SGI for use directly with the CE7 would be beneficial. A further notable point is that SGI was found to be useful for investigation of particle dispersion, however, a sufficient drug mass is needed to investigate particle dispersion, as illustrated with the SGI results from the 4 mg dissolution tests in Figure 3.2 A and B (top).

3.4. Conclusion

SGI shows potential to be used as a real time monitoring tool during dissolution testing. It was able to give information about particle size and dispersal in the test cell. It was found that SGI is useful for characterisation of particle dispersion when a sufficient mass is used, and it has less value in characterising rapid dissolution. A high number of early detections corresponded to faster dissolution, and prolonged detection corresponded to slower dissolution especially with a higher mass of un-sieved particles. Addition of surfactant to the medium increased the dissolution rate (with a minimal change in solubility) and visibly improved particle dispersion observed in multiple SGI output graphs, which suggests better particle wetting. SGI

was therefore useful to interrogate the interplay of FR, mass, surfactant addition and crystal habit. Certain phenomena were observed, such as agglomerates found in all tests, which established the need for an automated online method for agglomeration identification (AIM) to be developed.

The AIM was able to accurately indicate the presence of agglomerates during dissolution. The most successful AIM criterion was a flexible combination of particle diameter and solidity (Diameter > Pr75 / Solidity < Pr75). Challenges include robust method development in the presence of very large/small number of particles, choice of parameters to describe agglomerates and suitable criteria cut-off parameters. A combination of signals, detection patterns and overall particle detections should be considered during AIM development and application. Specific AIM characteristics could be used to create an imaging training set for further ANN processing.

Chapter 4: Application of an AI image analysis and classification approach to characterise dissolution and precipitation events in the flow through apparatus

Results, discussion, and conclusions presented in this Chapter have been published in: Taseva A.R., Persoons T., D'Arcy D.M. (2023) Application of an AI image analysis and classification approach to characterise dissolution and precipitation events in the flow through apparatus. Eur J Pharm Biopharm. 2023 Aug; 189:36-47. doi: 10.1016/j.ejpb.2023.04.020

4.1. Introduction

Imaging and artificial intelligence (AI) approaches have been used with increasing frequency in pharmaceutical industry in recent years. Characterisation of processes such as drug dissolution and precipitation are vital in quality control testing and drug manufacturing. To support existing techniques like *in vitro* dissolution testing, novel PATs can give an insight into these processes.

From 2010 onwards up to this point, imaging technologies have been more frequently applied in pharmaceutical development. Phenomena such as crystal growth [96], [106], [107], particle sizing and object recognition [1], [108] and a single particle dissolution [105] were well described. In a flow-through set up, UV imaging was used to characterize *in vitro* drug dissolution, release and precipitation [114]–[116]. Imaging can be used as a real time monitoring tool to give extra visual information about the product or the process under investigation, it has the potential to speed up discovery processes and to support decision-making [8], [119], [171].

After the success of Amazon's Alexa™, Apple's Siri™ and ChatGPT™, recently, AI tools started emerging also into pharmaceutical research promising faster and more efficient data analysis. In this Chapter, a simple AI convolutional neural network (CNN) available in Matlab™ was used as a base to develop and validate an image-based anomaly classification model able to detect events occurring during dissolution and precipitation processes in a flow-through dissolution cell. The aim of this Chapter was to modify the existing model and explore its potential to identify features related to dissolution and precipitation such as plume or particles present in the test cell and to investigate its ability to characterise a dissolution process qualitatively and quantitatively over time.

4.2. Materials and methods

All materials used to conduct the work presented in this Chapter were described in Chapter 2 (Materials and methods). Dissolution and precipitation media were prepared according to section 2.2.1.1. (Media preparation). Dissolution and precipitation experiments are explained in detail in sections 2.2.1.3.1. (Dissolution in the USP 4 FTA) and 2.2.1.4.1. (Precipitation in the USP 4 FTA). An overview of the original AI model is presented in section 2.2.2.2.1. (One-class anomaly detection model overview). The API method development and validation is described in section 2.2.2.2.2. (Model development and validation – API).

4.3. Results and discussion

4.3.1. Precipitation experiments

As detailed in Table 2.2, all conditions with ibuprofen resulted in plume formation immediately after the medium change. The precipitation conditions in the case where ibuprofen was dissolved in the test cell rather than using a prepared solution resulted

in faster particulate formation, notable in the first minutes of the medium change. A possible reason is the presence of small particles under the camera detection limit, which grew faster or the presence of particles outside of the imaging window. The imaging window focuses on a small part in the centre of the test cell, thus events occurring at the bottom above the glass beads or at the top (near the filter) of the cell could be missed. It is possible that a single particle re-formation occurred earlier than it was observed, but that the plume formed in the test cell interfered with its detection. No plume or particles were observed from the control, hence all plume and particle formations in the other experiments are from ibuprofen precipitation. In summary, both approaches of conducting a dissolution test or using a previously prepared ibuprofen solution before inducing precipitation enabled sufficient visualisation of particulates, which formed at earlier or later time points, respectively.

4.3.2. Dissolution experiment

The dissolution profile is shown in Figure 4.1. For the dissolution-based training, images from the 6th minute (17.7% drug dissolved) were classified as anomalous images and images from the 120th minute (100% drug dissolved) were classified as "normal" images. The 7 test points (2nd, 15th, 40th, 50th, 60th, 80th and 100th minute) were chosen to describe the dissolution profile. The second minute represents the beginning of the test where 3% drug is dissolved and many particles are visible in every frame. At the 15th minute (40% drug dissolved) particles are still present in each frame, however, they are fewer in number and smaller in size compared with the 2nd minute. The 3 middle time points of the dissolution (40th, 50th and 60th minute where 68%, 74% and 80% drug is dissolved respectively) were chosen to challenge the system by containing very few particles in approximately 15% of the frames. The 40th minute data set was even more challenging as air bubbles found in the test cell water jacket were visible in the background and confused the system. The final 2 time points (80th and 100th minute) were chosen to mark the end of the dissolution process (93% and 100% drug dissolved respectively). There were only empty frames representing the solution

formed after the drug is dissolved or almost fully dissolved when any remaining particles are no longer visible. The 80th minute data set was chosen to challenge the system when particles are not present in the test cell, but a similar interference as in the 40th minute was present (air bubbles on the external water jacket).

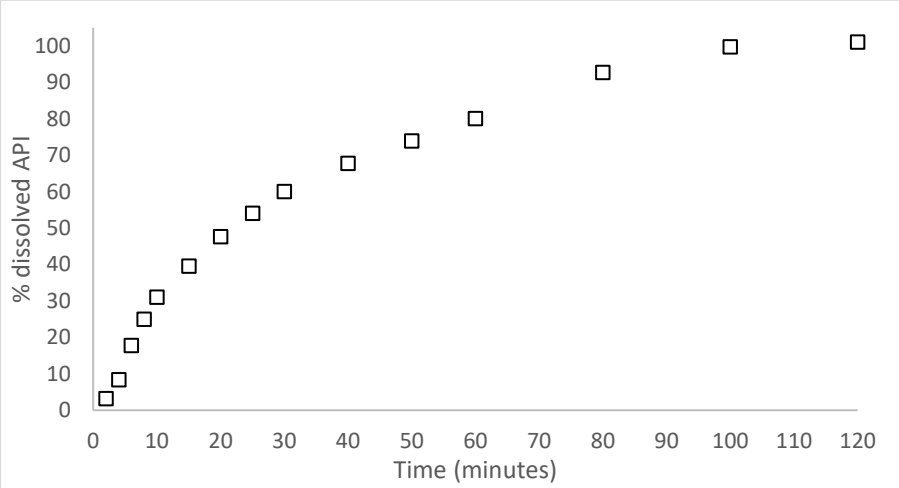

Figure 4.1: Dissolution profile of 20 mg ibuprofen in PB 0.005% w/v Tween 20 at FR 16 mL/min

4.3.3. Model validation and event detection

4.3.3.1. Training reliability

During the double-anomaly precipitation-based test step, 32 empty images, 118 plume images and 85 particle images were used. When dissolution-based test sets were performed the plume and particle images were replaced by 133 dissolution test images.

During the dissolution-based tests in which 120th minute image data set was used as a reference (“normal”), 50 empty and 133 anomalous images were used. The changed number of frames is noted when the accuracy for each test is calculated.

The ten independent precipitation-based model trainings showed an average accuracy of 97%. All false negative results (example Figure 4.2) were of images where

particles were actually detected, as is evident from the heatmap. However, the heatmap score did not reach the anomaly threshold and they were misclassified as empty. In all tests the misclassified images were images containing particles except for one, where 11 images with a plume and only 3 with particles were missed (Figure 4.2). Even the results from the worst performing training of the system resulted in an accuracy above 91%.

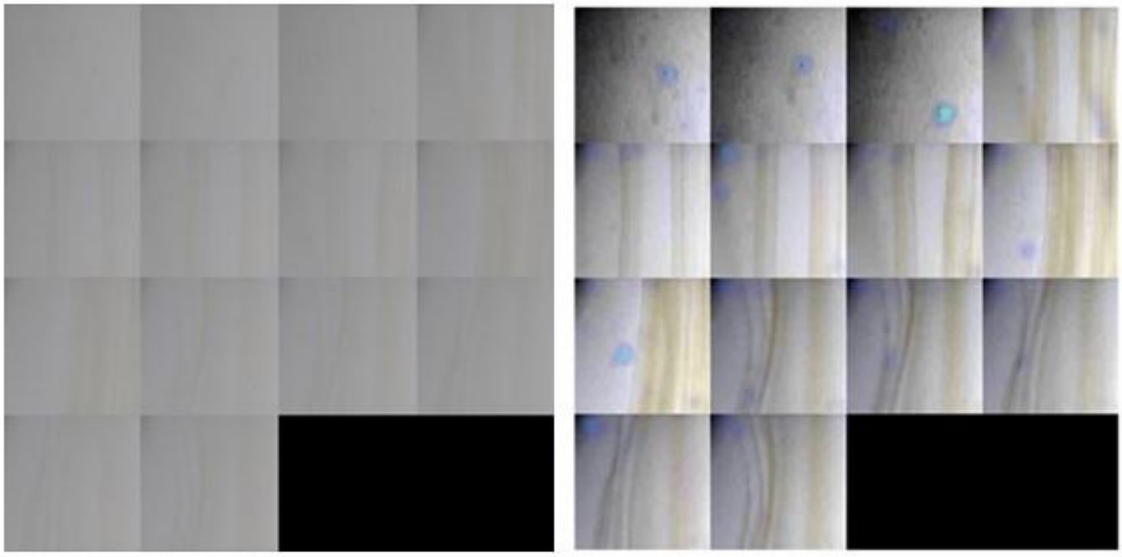

Figure 4.2: Misclassified images (top row, 3 images on the left with particles and the remaining 11 images with plume) after the training of the model. Original images (left) 225 x 225 pixels representing an imaging window of 5 x 7 mm of the dissolution test cell and the same images with heat map applied (right).

4.3.3.2. Trained model repeatability

The system ability to provide repeatable results was tested by using the best performing pre-trained model (100% accuracy during precipitation-based training) to run 10 tests on the same precipitation-based image data set. The average accuracy of the tests was again 97%. Furthermore, even the test with the lowest performance (Figure 4.3) showed an accuracy above 94%. Thus, the system showed repeatability and high accuracy irrespective of the model used (direct training and test or pre-trained model) for the precipitation-based data.

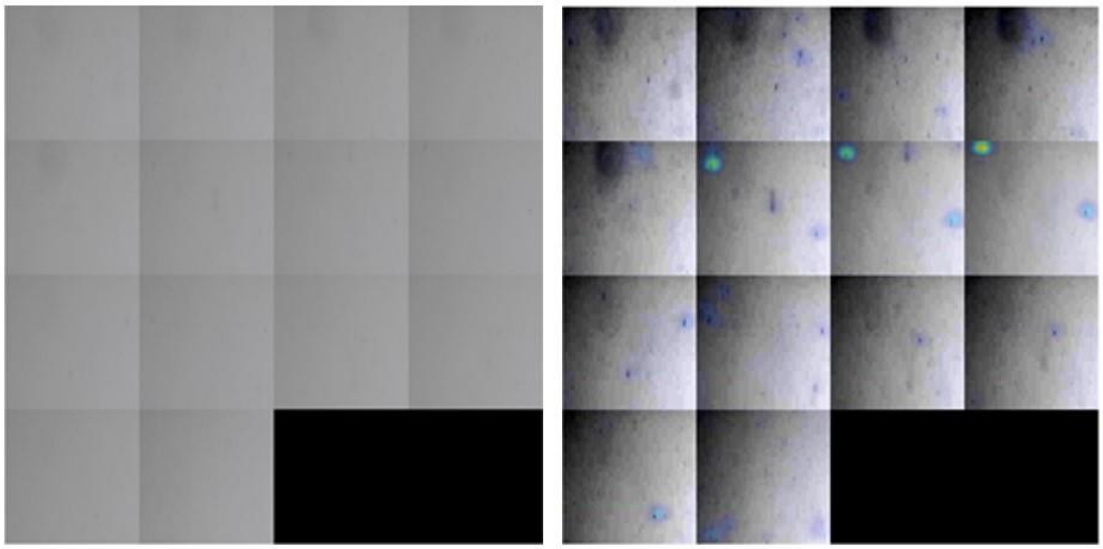

Figure 4.3: False negative results from the worst performing test when the pre trained file was used. Accuracy of the test was > 94%. Original images (left) 225 x 225 pixels representing an imaging window of 5 x 7 mm of the dissolution test cell and the same images with heat map applied (right).

4.3.3.3. Trained model sensitivity test

To test the model sensitivity the best performing precipitation-based pre-trained model described in the previous section was tested to classify only one type of anomaly. The results were compared with tests from the 2 single-anomaly precipitation-based trained models. All 3 pre-trained models showed high accuracy (Table 4.1). Furthermore, the accuracy of the system was consistently high over 10 tests with each model after single-anomaly trainings and the combined training (plume and particles) were completed (Table 4.1). The results from the tests conducted after single-anomaly trainings were similar to those generated by using the pre-trained double-anomaly model (accuracy > 91%). The test accuracy when only images with particles were used was the same for either combined or separate training. When images with a plume were tested separately the accuracy of the model was lower compared with the training where both plume and particle containing images were used. The combined double-anomaly training showed better detecting ability in both

test conditions. The presence of small anomalies like re-formed particles on the edge of the camera detection limit were beneficial to create a sensitive model with low ATS. This way the system successfully detects changes in the test cell that might be missed from a less sensitive model, *e.g.*, single-anomaly plume training.

The system variability is dependent on the images pulled for training and testing. Even when a pre-trained mode is used, the system pulls a minimum of 45 random images for calibration (when only 1 anomaly type is used) and based on them, an anomaly threshold is calculated for each test. This way the bias of specifically chosen calibration/training images is reduced without compromising with the accuracy of the model.

The self-re-adjusting of the parameters in the hidden loops of the CNN during training successfully created a very high accuracy model which could be used not only for its original purpose (tablet anomaly detection) but, with judicious use of training images, it could also be transferred to a different area of drug development. The precipitation-based data set shows potential to identify anomalous images (plume or particle) indicating that the precipitation process has or has not occurred. Furthermore, the system was able to detect early (plume formation (Figure 2.8 B)) and also late (particle re-formation (Figure 2.8 C)) stages of the process. The sensitivity test results illustrate the potential for flexibility in applying further training to an initial trained model to detect different events (in this case plume vs particle) in the dissolution test cell.

Table 4.1: Comparison of the model accuracy with single- and double-anomaly training and performance when only one type of anomaly is tested with both pre-trained (single-/ double-anomaly) models.

	Training with two types of anomalies	**Training Empty vs. Plume**	**Training Empty vs. Particles**
Model accuracy from the training:	100.00%	98.00%	94.00%
Tested anomaly type:	**Model performance: average accuracy after 10 tests**		
Plume	95.00%	91.67%	-
Particles	97.87%	-	97.00%

4.3.3.4. Effect of image size on model accuracy and training time

Comparisons of model sensitivity to image size are presented in Table 4.2. The accuracy of the model was not affected by the image size as the % accuracy was above 98% in all tested sets; the time for training, however, was notably different. Small image sizes were processed much faster than higher resolution images. The smallest image set (150x150 pixels) was processed approximately 10 times faster than the largest set (450x450 pixels) (24 minutes vs 5 hours respectively). The training time is highly affected by the computational power available. If more powerful computational resources are available, the time could be minimized and/or higher quality images could be processed. On the other hand, the model is highly accurate even at lower resolution. It can be concluded that the intermediate size used (225x225 pixels) is adequate for the current work.

Table 4.2: Effect of image size on model training.

Image size (pixels)	Total training time (h)	Accuracy (%)	Number of misclassified images	Misclassified as empty/anomaly
150x150	00:24:02	98.3	4	Empty
225x225	01:02:18	100.0	0	N/A
255x255	01:10:09	100.0	0	N/A
450x450	05:34:32	99.1	2	Empty

4.3.3.5. Characterization of events during dissolution testing

When the dissolution-based model built using the dissolution-based image data set, was used to test the dissolution test images, the resulting accuracy was 96%. These results could be compared with the accuracy of the precipitation-based model, which was 100%, when tested on precipitation-based image data set.

In terms of the application of both models to the dissolution test images, the ATS value varies depending on the pre-trained model used. It was found that the precipitation-based model has ATS values of 0.13 – 0.87 and the dissolution-based model ATS values of 0.29 – 1.38. Four of the dissolution test image sets (40th, 60th, 80th and 100th minute) were found challenging for the models and thus they were tested in triplicate.

The dissolution-based model was 100% accurate for data from the 2nd and 100th minute, where all images contained either numerous particles or no particles, respectively. The 15th min image data set was challenging for the dissolution-trained model due to a high calculated ATS value (0.53). Although the particles were still present in the test cell, they were more difficult to detect because much of the dissolution had progressed (40% dissolved drug), thus the particles were smaller and

their colour was similar to the background, which requires a sensitive model with a lower ATS value. In contrast, the precipitation-based model was 100% accurate in classifying test sets where particles were present in all images (2nd and 15th min) and less accurate when all frames were empty (100th min). When the calculated ATS value was close to that for the normal (no particles) image set (0 – 0.1), part or all frames were misclassified.

The ATS value is critical for the model accuracy. It is based on random images from the calibration data set used. In the case when the images in the calibration set are not precisely chosen to give an ATS value in a certain range, it could result in weak model performance. Even though the dissolution-based model did not classify all images from the 15th minute as anomalous, the accuracy was only 60%. On the other hand, the ATS calculated based on the precipitation data set was 0.26 – an ATS value low enough to inaccurately classify all images as anomalous, *i.e.*, images with particles.

The 50th min data set contains frames with a single particle in them and frames without particles. All images were classified with sufficient accuracy with both models (dissolution- or precipitation-based). The dissolution-based model misclassified only 3 images (accuracy 98%), while the precipitation-based model had 100% accuracy. The 60th minute data set was classified by the dissolution-based model with consistent high accuracy (85%) each time and the same number of false negative frames despite the ATS value range (0.29 – 1.18). The precipitation-based model showed lower accuracy when the ATS value was closer to that calculated from image sets with empty frames (0.16), and higher accuracy than the dissolution-based model when the ATS value was higher (0.8). It was found that for the dissolution-based model it is easier to detect a single particle in a set with many empty frames than many small/pale particles present in multiple frames (15th minute).

The most challenging were the 40th and 80th minute data sets. The 40th minute data set contained 21 frames with a single particle in the frame and an interference on the background of all images caused by the appearance of air bubbles in the water jacket surrounding the test cell. The precipitation-based model showed more false positive results, while the dissolution-based model showed more false negatives (Table 4.3). Although the dissolution-based model showed higher (above 1) ATS values in 2 out of

3 cases and it misclassified some of the frames with particulates (false negative), it has higher accuracy rate compared with the precipitation-based model which was too sensitive to the background change (bubble interference). The precipitation-based image set contains smaller particles (formed post-precipitation) compared with the dissolution image set. Re-formed particles captured in the test cell during the precipitation process have a size nearer to the detection limit of the camera (10 – 20 µm), while pre-dissolved particles captured early in the dissolution study have a median size of 162 µm (Chapter 3, section 3.3.1.3). In the 80th minute data set all frames were empty, however the interference from bubbles on the water jacket was so strong that both models misclassified all images. Overall, based on the results presented in Table 4.3, the dissolution-based model showed higher accuracy. Although it misclassified some of the frames from the 15th minute data set, the system was able to suggest that the dissolution process was still ongoing at this time. On the other hand, when it comes to event-detection, the precipitation-based model showed higher sensitivity, showing potential to capture events (even small particles) when they appear in a frame.

The system's ability to quantitatively characterise a continuous process such as particle dissolution was explored by a comparison between the dissolution profile and the percentage frames without an anomaly predicted from both models and is presented in Figure 4.4. In the beginning of the dissolution test (2nd minute) both models showed 0 frames without particles, *i.e.*, particles were present in all frames and at late time points (100th minute) when the dissolution test was over and particles were not present in the test cell, both models showed 100% empty frames. The precipitation-based model, while more accurate in identifying the presence of any particles (15th minute) was not descriptive enough to acknowledge the progression of the dissolution process, *i.e.*, the 0% frames without particles suggest that there are particles present in the test cell but cannot account for the change in their size or number, and therefore the progression of dissolution (40% dissolved drug). It underpredicted the dissolution process by suggesting more frames containing particles (false positive) even at later time points (40th minute) (Table 4.3, Figure 4.4 A). On the other hand, the false negative results from the dissolution-based model (15th minute)

overpredicted the dissolution rate by suggesting more frames without particles (> 50%) (Table 4.3) while they were still present in earlier time points. However, what presents as a reduced accuracy in particle detection from the dissolution-based model (60% accuracy at 15th minute) in fact represents the model essentially ignoring some smaller particles and classifying those frames as empty. The suggested 56% frames without particles from the dissolution-based model represent better the dissolution process at the 15th minute where 40% of the drug is dissolved, than the 0% empty frames detected by the precipitation-based model (Figure 4.4 B). The dissolution-based model therefore shows potential to be adapted for quantitative characterization of *in vitro* dissolution testing. The problematic interference from extraneous bubbles in the water jacket at the 80th minute rendering both models inaccurate at this point, points to a need to both understand the potential sources of image interference and ideally to include such interferences in model training, such that the classification accuracy will not be affected during testing. As the duration of a dissolution test can frequently extend beyond the 2 hours' time frame required in the current work, the likelihood of the presence of interfering factors at later time points in the dissolution test (air bubbles, precipitates, impurities) should be considered to ensure model training can account for any trends in such interferences.

Table 4.3: Pre trained model accuracy; Dissolution diagnostics based on the precipitation- and dissolution based pre trained models used. The tests used in Figure 2.6: Image pathway for validation and training and assessing ability to detect precipitation events (A) and image pathway used for dissolution testing analysis (B). A: The image data set could contain dissolution or precipitation images irrespective of the performed training. B: Image data set 1 could contain dissolution or precipitation images allocated for training and calibration before testing, while image data set 2 contains only dissolution images for testing. Figure 2.6 A and B for comparison with the dissolution profile are highlighted.

Type of training	**Precipitation-based**	**Dissolution-based**
Training accuracy	100%	96%

Dissolution image data set	**Accuracy (%)**	**ATS**	**Misclassified images (%)**	**Frames without anomaly (%)**	**Accuracy (%)**	**ATS**	**Misclassified images (%)**	**Frames without anomaly (%)**
2	100	0.69	0	0	100	1.38	0	0
15	100	0.26	0	0	59	0.53	56 (false negative)	56
40	32	0.50	85 (false positive)	0	90	1.18	14 (false negative)	99

	33	0.82	85 (false positive)	3	90	1.18	15 (false negative)	99
	34	0.80	82 (false positive)	3	97	0.53	6 (false negative)	92
50	100	0.87	0	86	98	0.53	0.3 (false negative)	89
60	92	0.80	10.5 (false negative)	89	85	0.29	20 (false negative)	98
	36	0.16	79 (false positive)	0	85	1.18	21 (false negative)	100
	87	0.69	16.5 (false positive)	60	85	0.53	21 (false negative)	98
80	19	0.16	100 (false positive)	0	27	0.53	100 (false positive)	0
	19	0.69	100 (false positive)	0	27	0.53	100 (false positive)	0
	19	0.17	100 (false positive)	0	27	0.53	100 (false positive)	0
100	100	0.80	0	100	100	0.53	0	100
	70	0.50	38 (false positive)	62	100	0.53	0	100
	0	0.13	100 (false positive)	0	100	0.53	0	100

An AI method for quantitative analysis of a drug release process has been presented, where an AI-based image segmentation and quantitative analysis was used to predict the *in vitro* drug release performance of long-acting parenteral implants [132]. Their model prediction was in a good agreement with the experimental results (5% and 10% differences for medium and low drug loading implants, respectively). In this current work, the AI classification system successfully detected three main stages of the dissolution process: 1) beginning of the dissolution when many particles are present in the frames, 2) ongoing dissolution when particles are still evident in the test cell but a number of predicted empty frames appear, and 3) end of the dissolution when the drug is dissolved, and all frames are "empty". A disadvantage of the method that should be considered is that the imaging window does not represent the volume of the whole test cell. There are parts that are not visible to the system, thus presence or absence of particles could not be confirmed. This limitation could be overcome by multiple camera use (3D imaging) [107]; this particular approach was used to characterize a single dissolution profile. Although this could be considered a limitation of the method, the model showed high accuracy and has a potential to be applied to other dissolution tests conducted under different conditions, *e.g.*, to test different drug masses, formulation, medium composition, flow rates or to investigate other processes like crystal growth or aggregation. Further training with a careful selection of training and calibration images could be used to improve the discriminatory power of the method and to provide a better correlation between the percent empty frames and the dissolution profile. Notwithstanding these potential improvements, the trade-off between improved accuracy and resources in terms of computational space and time for image data set creation is also a core consideration.

The precipitation-based model although more accurate than the dissolution-based model at 15th minute of the test, shows poor performance classifying the images from the 40th minute data set (30% accuracy) due to oversensitivity of the model. However, this model sensitivity contributed to the accurate event detection by the model (early and late stages of precipitation). Knowledge of image characteristics relating to different events (*e.g.* particles or plume) in combination with a sensitive model like the precipitation-based model presented in this work could be transferred for detection of

other events or parameters where a slight change in the product could be of crucial importance, *e.g.*, product stability [64] or powder consistency [168]. The transfer learning technique gives many opportunities to use available models trained for a different purpose to solve new, yet similar, problems in another field [199]. This facilitates application of detailed ML approaches across different disciplines, though a thorough validation approach should be employed.

Nowadays, imaging and NNs find application as monitoring and control tools in continuous upstream processes, such as synthesis and crystallization [172], in many downstream processes such as drug powder blending [168], granulation [119], [172] and tabletting [205], [218]; and for investigation of the final product, *e.g.*, during dissolution and release testing [115], [166]. A recently developed CNN system which detects tablet anomalies from x-ray microcomputed tomography images showed high accuracy (94%) and could be rapidly adapted to detect inner defects in other solid dosage form products [219]. According to the authors, this approach could be used for large-scale manufacturing inspection by being time and cost efficient [219]. Mészáros *et al.* focused their work on development and application of PAT UV/VIS imaging-based classification model using pattern recognition NN for qualitative and quantitative particle size assessment in intact tablets [216]. Their machine vision model showed greater than 97% accuracy when applied to different particle sizes of an API. It was found that the use of AI systems reduces experimental time and could be applied in different areas of pharmaceutical industry in order to increase productivity, efficiency and quality of the processes [192], [220]. Furthermore, sophisticated image analysis is being used in novel approaches to solubility testing in a flow-through set up by using machine vision to recognize particles and track their morphology [221].

According to a recent review the emerging interest and application of AI in many areas of pharmaceutical development urges regulatory agencies to propose guidelines and recommendations for good practices with which to address the use of AI algorithms and their classification as medical devices [222]. On the other hand, some of the commercially available imaging systems used during dissolution testing already provide cameras with AI software which can measure and evaluate physical

parameters like paddle rotation speed (USP 2 paddle apparatus) but also enable continuous video monitoring of the dissolution process.

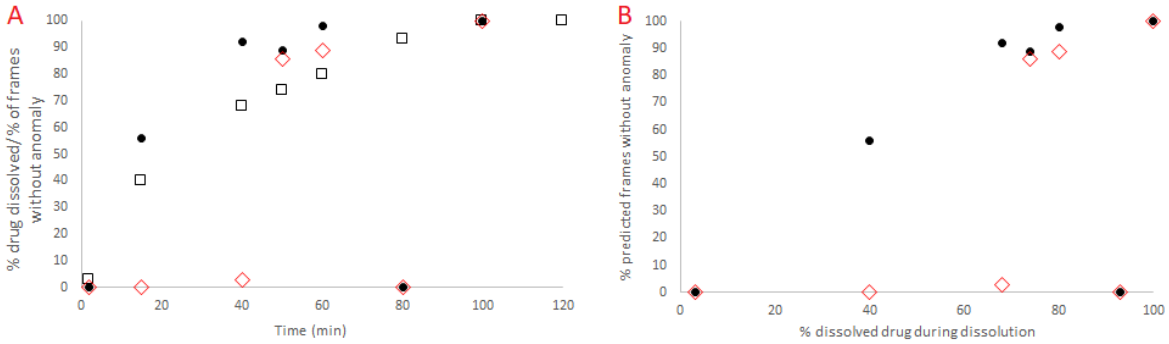

Figure 4.4: A: Dissolution profile (empty black squares) and % frames without anomalies from the precipitation-based model (empty red rhombus) and the dissolution-based model (filled black circles) vs time; B: Dissolution rate vs. % predicted frames without anomaly from the precipitation-based model (empty red rhombus) and dissolution-based model (filled black circles) tested on the dissolution test data sets collected at the 2nd, 15th, 40th, 50th and 100th minute of the dissolution test.

4.4. Conclusion

Dissolution and precipitation processes were examined by imaging techniques and specific features for each process were determined. These features were used to develop a highly accurate model for anomaly classification based on two types of images (normal and anomalous) and tested on images representing early and late stages of precipitation (plume or particle images, respectively). The system accuracy and sensitivity were tested by using precipitation-based double- (plume and particle) or single- (plume or particle) anomaly trained models to identify images with only one type of anomaly. The double-anomaly trained model showed better sensitivity and high accuracy classification (> 95%) due to calculation of a lower ATS value. The system was also trained with two data sets based on precipitation or dissolution images;

following this, the two datasets were tested to identify changes in the presented test cell images during dissolution to characterise the dissolution process.

An automated classification method such as the one presented in this work, has potential application to online dissolution test imaging. The model was found descriptive enough to suggest beginning, middle and final stages of a dissolution process and to identify the early and late stages of precipitation process (plume and particle formation). Predictable interferences in the images such anomalous air bubbles in the water jacket affected model accuracy. Carefully curated training and calibration sets, incorporating the potential to distinguish between relevant events and predictable interferences, could provide a sensitive and accurate pre-trained model able to detect events occurring in the FTA test cell. Due to the limited possibilities for image acquisition in the FTA (closed system without option to insert a probe) the use of an AI system providing image processing and/or image-based classification can provide insight to the dissolution process. However, the benefits of increasing model accuracy need to be considered in the context of the increase in computational and time resources required for acquisition and classification of images and for system training.

There is potential for the classification system to be used to characterise the stages of dissolution and precipitation in the FTA test cell, and, as a proof of concept, the current work demonstrates potential for deep machine learning image analysis to be applied to kinetics of other pharmaceutical processes.

Chapter 5: Application of an AI image analysis to dissolution testing of paediatric oral suspensions in the USP 4 flow-through dissolution apparatus to explore the potential to use imaging as a discriminatory analytical tool for complex formulations

5.1. Introduction

Oral suspensions are a preferred dosage form for children as the drug product can be precisely dosed and easily administered.[223] Furthermore, this formulation allows taste masking, an important feature for the paediatric population, especially for bitter drugs such as most painkillers. Challenges related to the dissolution testing of this type of formulation include proper choice of apparatuses as well as media composition and agitation rate, needed to ensure good discrimination. The most suitable ways to perform dissolution testing of suspensions is a widely discussed topic in the literature.[4], [81] Traditional dissolution testing is well accepted in pharmaceutics, however, not everything that happen in the test cell/vessel can be explained based only on a dissolution profile. Differences in the dissolution profile could appear due to inconsistency of the formulation, presence/change of excipients, change in the API manufacturing process, *e.g.*, API crystals produced by a different crystallization process which results in a different API crystal habit.[35], [93] Dissolution testing used alone is not able to describe phenomena such as viscous fingering, channel formation or particle behaviour during dissolution. To provide a possible solution to some of the challenges related to dissolution testing of suspensions, in this current work, the aims

were to investigate the dissolution behaviour of oral paediatric suspensions, to apply image and AI CNN analysis to quantitatively describe the dissolution process in the USP 4 FTA and to offer a tool for product discrimination.

5.2. Materials and methods

All materials used to conduct the work presented in this Chapter were described in Chapter 2, section 2.1 (Materials). Dissolution medium used for dissolution was phosphate buffer pH 6.8, section 2.2.1.1.1. Drug products were characterized by testing their density, section 2.2.1.2.5 and viscosity, section 2.2.1.2.6, and by API visualization using optical light microscopy, section 2.2.1.2.4. All dissolution tests were performed in the USP 4 FTA CE7, section 2.2.1.3.1. Samples were analysed by high-performance liquid chromatography (HPLC), section 2.2.1.5.2. Direct monitoring and video acquisition during dissolution testing was done by using the SGI camera, section 2.2.1.6.1. Images were further analysed by using an AI CNN analysis, section 2.2.2.2.3.

5.3. Results and discussion

5.3.1. Dissolution in the USP 4 FTA

Dissolution profiles and the results from the two AI analysis approaches (%FwA and %avgATS) from the dissolution test of N100/N200 in the large/small test cell are presented in Figure 5.1. The related image sequences can be seen in Figure 5.2. Figure 5.3 and Figure 5.4 relate to the dissolution, AI analysis and images from the dissolution testing of B100 and B200, respectively. N100 and N200 had a faster dissolution rate (approximately 75 – 120 min needed for full dissolution) in comparison with B100 and B200 (>120 min) in both test set ups, although the viscosity of N100 and N200 was 2 to 3 times higher than the viscosity of B100 and B200 at both room temperature and 37°C

(Table 5.1). In all cases, the lower drug strength formulation had lower viscosity and dissolved faster than the same brand higher strength formulation. All dissolution profiles, apart from N200, show faster dissolution in the small cell compared to the large cell. Only N200 dissolved slightly faster in the large cell, which is confirmed by the images with particles visible for longer in the small cell (90 min) compared to the large cell (75 min) (Figure 5.2).

Table 5.1: Viscosity of oral suspensions – Brupro and Nurofen.

Temperature	N100 (mPa.s/g/ml)	N200 (mPa.s/g/ml)	B100 (mPa.s/g/ml)	B200 (mPa.s/g/ml)
20°C	118 ± 8.5	179 ± 4.9	45.7 ± 1.5	49.4 ± 0.3
37°C	83 ± 3.5	120 ± 0.6	38.5 ± 1.1	42.9 ± 0.3

When investigated by light microscopy (Figure 5.5), all suspensions revealed plate-like particles of ibuprofen, with smaller size for N100/200 and larger for B100/200, which probably explains some differences in the dissolution rate of the formulations. Another difference is the suspending agent used in the formulations. In N100 and N200 the suspending agent was hydroxypropyl methyl cellulose, while in B100 and B200 sorbitol solution and propylene glycol were used. The combination of sorbitol/propylene glycol results in a lower viscosity, but slower formulation dispersal under current test conditions. Traces of the suspension matrix are evident up to 270 min of the dissolution of B100/B200 in the large test cell (Figure 5.4). In the case of N100/N200 neither particles nor matrix components are evident after 90 min of the test regardless of the cell used (Figure 5.3). Spots visible at the end of most tests, *e.g.*, Figure 5.3 D (120 – 150 min images) show air bubbles formed on the outside of the test cell in the water jacket. They have no effect on the dissolution process inside the cell, however they could be misinterpreted by the AI image analysis as particles.

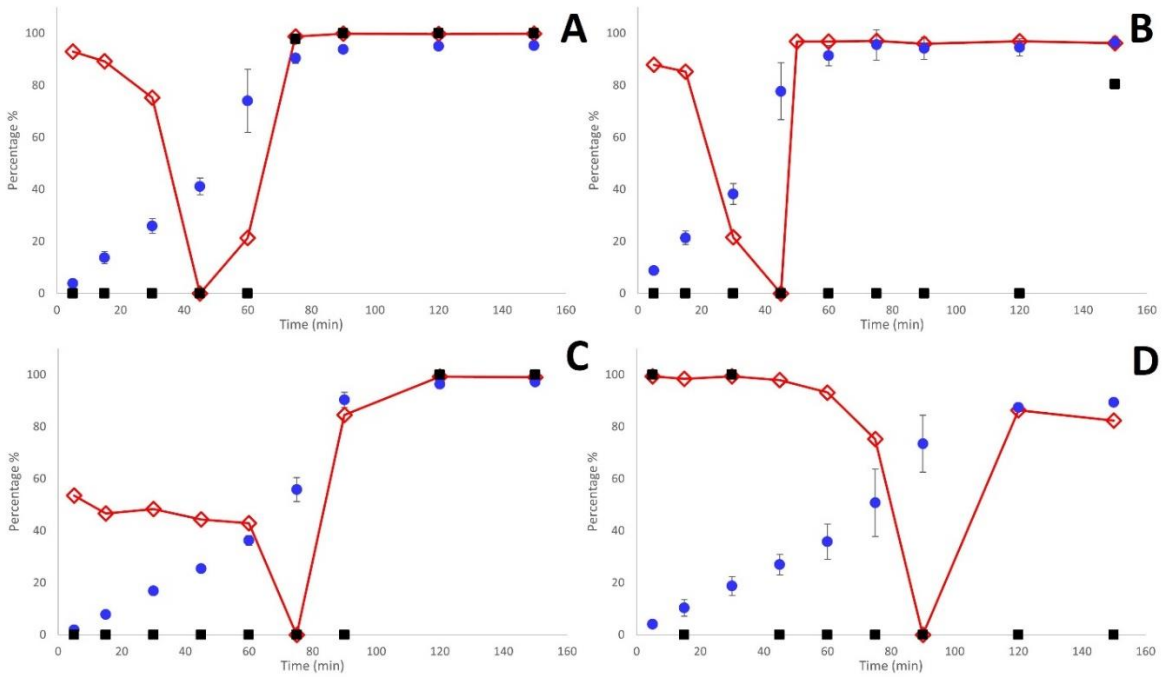

Figure 5.1: Dissolution profile (blue dots), percentage avgATS (red diamonds) and percentage frames without anomalies (black squares) over time from the dissolution of 2.5 mL N100 large cell (A), N100 small cell (B), N200 large cell (C) and N200 small cell (D) in the USP 4 FTA at FR 16 mL/min.

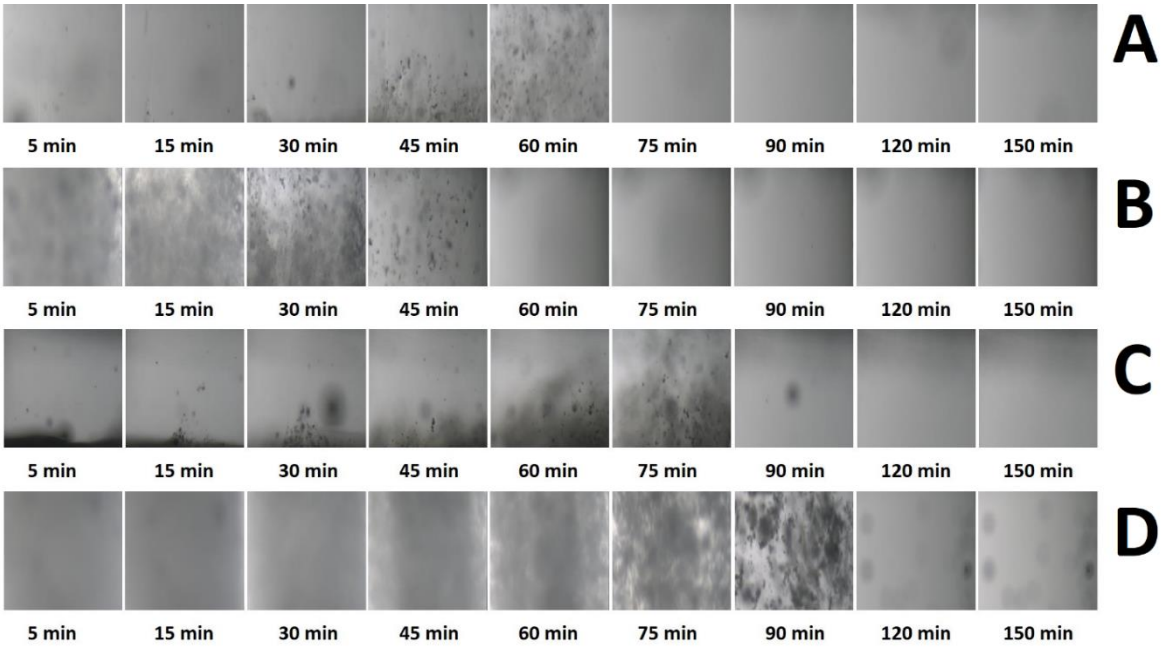

Figure 5.2: Image sequence obtained during the dissolution of 2.5 mL N100 large cell (A), N100 small cell (B), N200 large cell (C) and N200 small cell (D) in the USP 4 FTA at FR 16 mL/min.

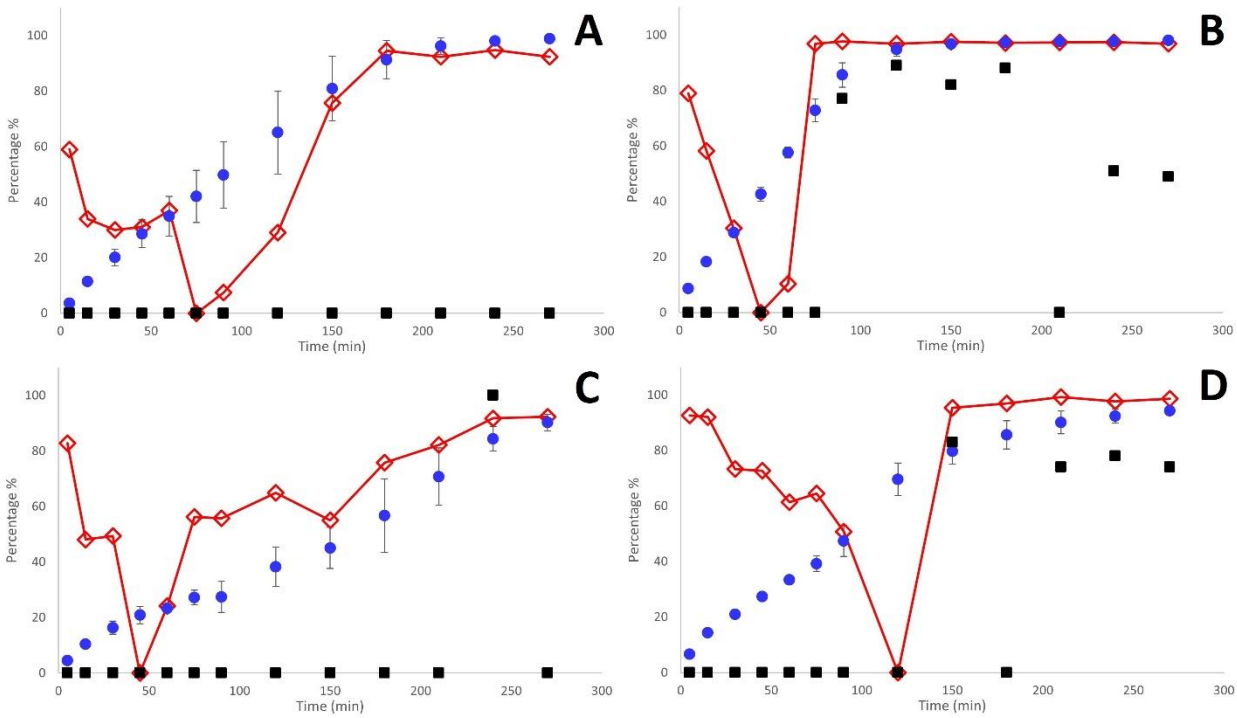

Figure 5.3: Dissolution profile (blue dots), percentage avgATS (red diamonds) and percentage frames without anomalies (black squares) over time from the dissolution of 2.5 mL B100 large cell (A), B100 small cell (B), B200 large cell (C) and B200 small cell (D) in the USP 4 FTA at FR 16 mL/min.

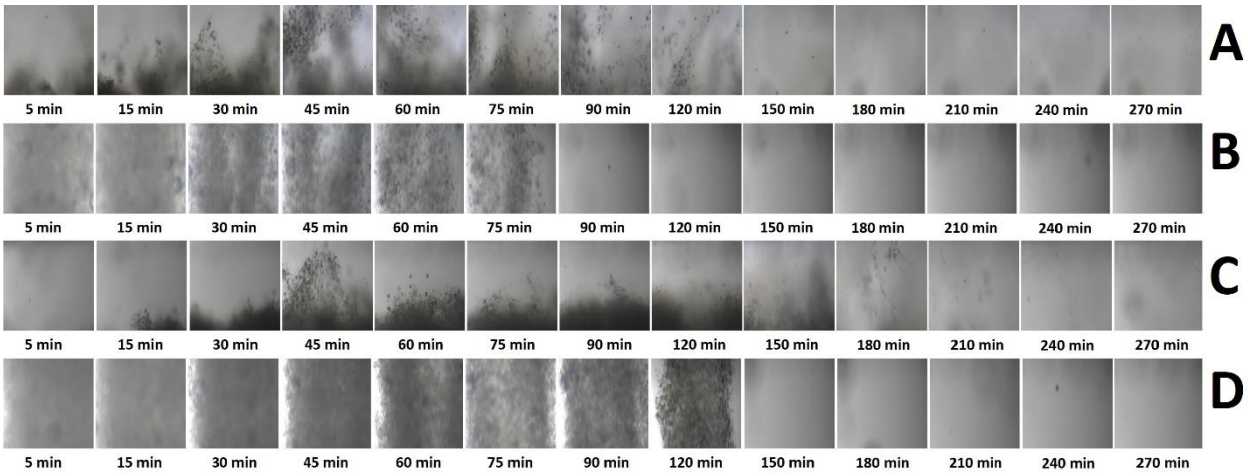

Figure 5.4: Image sequence obtained during the dissolution of 2.5 mL B100 large cell (A), B100 small cell (B), B200 large cell (C) and B200 small cell (D) in the USP 4 FTA at FR 16 mL/min.

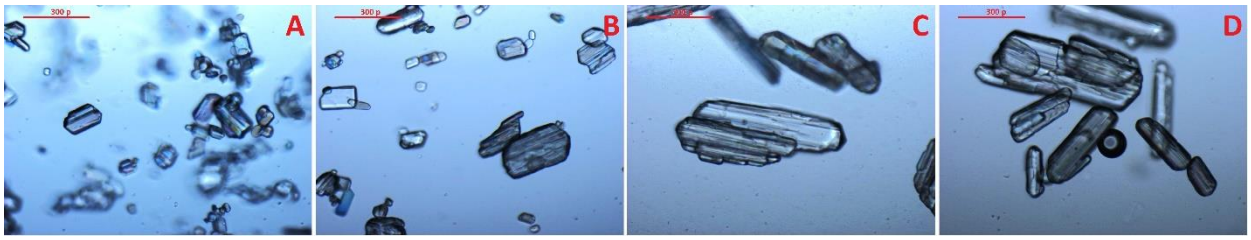

Figure 5.5: Microscopic images of N100 (A), N200 (B), B100 (C) and B200 (D) at 20x magnification.

5.3.2. Hydrodynamics and suspension dispersal

Differences in the hydrodynamics in the small and large USP 4 FTA test cells regarding tablet positioning and flow regimes have been broadly investigated *in vitro* and *in silico*.[2], [55], [224]–[227] Both test cells have a conical bottom part with an opening which lets the pulsing upstream flow pass through the cell and an inner diameter of 12 mm for the small cell and 22.6 mm for the large cell. Kakhi predicted the fluid dynamics in the USP 4 FTA cell by a mathematical modelling approach of three situations – no beads in the cell, only one 5 mm ruby bead and a packed column with 1 ruby bead at the bottom apex of the cell and 1 mm glass beads covering the conical part of the test cell (used in this current work).[226] This resulted in a laminar fluid flow in the "packed column" regime and a turbulent flow under the other two regimes. Shiko *et al.* investigated the regimes including beads described by Kakhi *et al.* under a variety of flow rates and in presence of a non-disintegrating tablet. For most test conditions, the flow was heterogenous, characterized by re-circulation and backward flow.[224] D'Arcy *et al.* used computational fluid dynamics to simulate and analyse the hydrodynamics in the USP 4 FTA, while Shiko *et al.* applied MRI to visualize the hydrodynamic flow in the USP 4 FTA cell. [224], [227], [228] The hydrodynamic flow was found to be a main factor affecting the dissolution rate of non-disintegrating tablets by changing the diffusion layer which are in contact with the formulation surface.[164], [227], [229]–[231] Furthermore, the dosage form itself can affect the hydrodynamics in the cell depending on its position, geometrical and solubility characteristics.[2], [55], [225], [226]

At the time of writing, reports are not found in the literature regarding the hydrodynamics in the USP 4 FTA when a liquid formulation such as suspension is used for dissolution. The addition of 2.5 mL dose of the formulation forms a layer (approximate thickness of 5 mm) on top of the glass beads in the large cell, where it occupies almost the whole volume of the small cell (approximately 35 mm). The sample distribution in the test cell results in changed fluid dynamics through the cell. Channels are formed through the suspension layer during dissolution. This phenomenon is observed better in the large cell when the suspension is expanding. Parts of the suspension are pushed upwards, forming tips which move during dissolution (examples in Figure 5.2 C – 15 and 30 min; 5.2A – 30, 75, 120 min). In the small cell channels are not that well visualized. Typically, one main channel is formed through the suspension or on the side – between the suspension and the cell wall. In most cases the whole mass of the suspension is pulsing up and down in the cell during the test as one whole. A phenomenon described during mixing of fluids with different viscosities is viscous fingering.[90] Viscous fingering occurs as a result of instabilities when a more viscous fluid is displaced by a less viscous fluid when both fluids are fully miscible together. An example for this is the mixing of water and glycerol.[90] Another study that used a numerical simulation showed that this phenomenon is not observed when the more viscous fluid displaces the less viscous one.[91] As a consequence of the viscous fingering, two competing effects were described: 1) mixing enhancement due to induced mixing disturbance and increased contact area between the fluids, and 2) channel formation used as a mainstream by the lower viscosity fluid, which passes through the higher viscosity fluid through these channels, thus decreasing the overall mixing efficacy.[92] Fingering and tip formations are well visualized in the large cell (Figure 5.2 and Figure 5.4, A and C), mostly when B100 and B200 formulations were tested. The slower dissolution rate of B100/200 provides a longer observation time and slower changes of the suspension surface. It can be suggested that the dissolution from the suspension in the small cell occurs mostly at the sides between the suspension and the wall of the test cell due to the layer thickness as the distance between the wall and the formulation becomes larger while the suspension remains one whole during the test (Figure 5.4 B – 45 and 75 min; Figure 5.4 D – 75 and 120 min). Channels through the suspension can be observed in all test set ups, however,

they can be best investigated in the small cell as the formulation occupies the whole imaging window, while in the large cell, due to the space available for the suspension to move upwards, the channels are shorter and viscous fingers are formed. The area where a channel is formed becomes brighter and particles (dark sports) are distributed around it, *e.g.*, Figure 5.2B, image "30 min". In the case of N100/200 (Figure 5.2 B and D), the HPMC-based suspension matrix expands and forms a transparent region around the particles. The aqueous medium can move through these channels increasing the surface area for dissolution. B100/200 matrix composition is less viscous, thus the channels formed through the suspension are not that clears as when N100/200 were tested. One clearly visible channel goes through the middle of the B100 suspension (Figure 5.4 B – 30 min), and the formulation stays as one whole during the test. A channel formed between the suspension and the wall of the cell is well illustrated in Figure 5.4 D, image "120 min". The increase of the distance between the formulation and the wall over time is evident in the image sequences from the small and large test cell (Figure 5.4 B and D). That suggests lower resistance and adhesion between the formulation and the material of the cell and stronger cohesion between the components of the formulation matrix. Furthermore, dissolution happening mainly at the sides would suggest a smaller surface area and could explain the observed slower dissolution rate of B100/200.

Based only on the images, it could be concluded that the dissolution is completed when the suspension is no longer visible in the test cell. However, suspension disappearance corresponds to 50 – 75% drug dissolved, and the images do not give any quantitative information about the % drug dissolved. Thus, more sophisticated AI imaging analysis methods can be used to describe the dissolution process more accurately and to provide extra information by using classification and hidden patterns to confirm the results.

5.3.3. AI image analysis approach

The %FwA approach was found less useful as it is a binary method used to classify images as “empty” or “with particles” (anomalies). It was highly dependent on external influences such as air bubbles that appeared in the water jacket (outer side of the test cell). It was mostly accurate for fast dissolutions such as N100/200 dissolution in the large cell. In these cases, the dissolution rate was fast, and the test was completed leaving less time for the air bubbles to form. As can be seen from the N200 test in the small cell (Figure 5.2 D) after 120 min many bubbles are formed, thus the %FwA would misclassify these images as it would count them as particles. For longer experiments, such as B100/200 dissolution tests, %FwA was able to detect some changes in the small test cell. Since at the beginning the formulation takes the full volume of the cell, the CNN was able to recognize when most of the “anomalies” disappear, *i.e.*, when the suspension is dissolved. The remaining “anomalies” are air bubbles blurring the image.[214]

The %FwA method shows potential to be used as a tool for a qualitative analysis. To describe the dissolution process of suspensions a more continuous, *i.e.*, sensitive approach is needed. AI gives the opportunity to use multiple parameters and large data bases for training and classification purposes to enable the system to find patterns and more sophisticated classification of the data. Thus, an image analysis approach (%avgATS) which allows a more quantitative approach was investigated.

The %avgATS detected three dissolution stages – 1) beginning of the dissolution – including formulation dispersal (suspension expanding/swelling); 2) enlargement of channel formations and decrease in the suspension mass/visible particles and 3) full dissolution of the formulation, *i.e.*, no visible particles (API or excipients) left in the test cell. At the beginning of the dissolution test in the small cell, the suspension is not in focus as the light is diffused by the matrix components, while the large cell looks empty as the suspension occupies a space under the imaging window in the test cell. Thus, the ATS for the first minutes of each test are low. This results in high %avgATS which decreases in a specific pattern depending on the test cell and the formulation used. For N100/N200 the decrease in the %avgATS values is smoother, while for B100/B200 it is more stepwise. When the suspension expands and covers most of the imaging window (large cell) or part of the matrix is dissolved so the particles are

focused better (small cell), avgATS reaches the maximum value for the dissolution test ($avgATS_{max}$), hence %avgATS is 0. In the graph, this point forms a sharp nadir that also serves the purpose of an indicator. This time point marks the end of the first and the beginning of the second stage of the dissolution (suspension expansion/swelling). After this time point, the suspension dissolves faster as viscous fingers and channels are already formed and there are more contact points between the drug and the medium. With the particles' dissolution and disappearance from the images, the avgATS value becomes closer to 0, and consequently the %avgATS becomes closer to 100 % following the dissolution profile. In comparison with %FwA method, this approach is less affected by external sources of image distortion.

The larger particle size of the ibuprofen in the B100/B200 formulation could be one of the reasons for the observed slower dissolution rate. Another suggestion is the effect of the matrix components. The suspension layer of B100/200 expands more slowly than the same volume of N100/200 and channels are not that well defined, which can be concluded from the %avgATS and the images. On the other hand, although N100/N200 formulations show faster dissolution rate and better mixing with the medium, the channel formation is clearer for B100/200.

The %avgATS plot describe the dissolution profiles well – 1) smooth and sharp or slow stepwise decrease of the avgATS towards the 0 point ($avgATS_{max}$) suggests the rate of channel formation, *i.e.*, medium penetration through the suspension, sample dispersal and local hydrodynamics; 2) the nadir of the %avgATS curve indicates the maximum swelling of the formulation. Here channels are already formed, and 40 – 70% of the drug is dissolved; 3) after the nadir, the %avgATS plot closely follows the dissolution profile and could be explored as a predictive model.

5.4. Conclusion

Dissolution testing of suspensions can be a challenging task given the minimal guidance provided for this specific formulation. In order to enhance the discriminatory

power of the test and to show the potential of a different approach to formulation testing, a new imaging analysis and use of AI classification were presented. In this work, two commercial brands of paediatric oral suspensions at two different strengths were tested in USP 4 FTA dissolution apparatuses equipped with an imaging system. Differences between the two brands were found regarding their dissolution rate, viscosity, excipient content and drug particle size. The two brands showed different behaviour during dissolution testing in the large and small test cell as well as between the strengths within the brand. The lower strength formulation dissolved faster than the higher strength possibly due to smaller drug amount dispersed in the same volume of the suspension. Based on the microscopy, B100/ B200 API particle size is larger than the API particle size in N100/N200. This may contribute to the observed slower dissolution rate of B100/200. Different viscosity enhancing agents used in both brands also affected the dissolution rate. In the case of N100/200 where HPMC was used, the suspension expanded faster, the matrix became transparent, and the dissolution was completed faster in comparison to B100/200 where the formulation stayed in the test cell as one piece and dissolved much slower. The medium transition through the suspension was challenging, thus in the small cell channels were formed on the side between the suspension and the test cell wall. Differences in the dissolution process and rate were also observed when the small or the large test cells were used. The dissolution was completed faster in the small cell, except for N200 which dissolved slightly faster in the large cell. The expansion of the formulation layer was well visualized in the large cell, while in the small cell the same dose occupied the entire available space. On the other hand, that provided an opportunity to observe channel formation through the formulation.

The imaging analysis and the two AI approaches gave important visual information regarding the suspension behaviour in the test cell. Phenomena such as channel formation, viscous fingering and suspension expansion could be observed. The binary %FwA approach provided qualitative information about the presence of formulation in the cell even though the method was influenced by appearance of external factors like air bubbles. The %avgATS approach was less sensitive to the effect of the air bubbles and it was able to provide quantitative and qualitative information comparable with

the dissolution profile. Three stages of the dissolution process were distinguished by the %avgATS method – 1) formulation dispersal and channel formation; 2) enlargement of the channels and dissolution of the formulation; and 3) full dissolution of the formulation when no particles are present in the test cell.

The %FwA has been applied in a simpler dissolution system where only API without presence of excipients was tested (This work was presented in Chapter 4 and published in the EJPB). This current work involves a more complex situation of sample dispersal and mixing of fluids of different viscosities. There is scope to use both presented image analyses to quantitatively characterise the impact of medium on suspension formulations in terms of sample dispersal and dissolution. Furthermore, image analysis could also be used to explore other in-use dispersions such as granules administered with soft foods, in patient-centric formulation development.

Chapter 6: Investigation of pH dependent drug precipitation and crystal growth in the USP 2 paddle apparatus by in-situ micro-imaging

This brief chapter outlines a preliminary study in the USP 2 paddle apparatus in combination with the Mini-cell LED Inflow Canty™ imaging system.

6.1. Introduction

One of the commonly used dissolution apparatuses is the paddle apparatus. As discussed in Chapter 1, it consists of dissolution vessels, placed in a water bath and a paddle rotating in each vessel. This set up allows a sample to be placed inside the vessel into a large volume of medium (500 – 900 mL). For comparison, in the USP 4 FTA, the medium volume is 8 mL and 19 mL inside the small (12 mm) and large (22.6 mm) test cells, respectively.[232] However, even volumes of medium greater than 900 mL can be circulated through the flow-through cell. Another benefit of the paddle apparatus is that a probe (*e.g.*, imaging or UV) can be inserted directly into the vessel,[101], [147], [233] while observation of phenomena in the USP 4 FTA is possible only on the outside as it is a closed system.

Drug precipitation *in vivo* has raised many concerns over the years especially for pH dependent drugs. *In vitro* drug precipitation of poorly soluble weak bases in the small intestine due to a pH change has been explored by simulating the transition of the solution to the small intestine to observe precipitation in the paddle apparatus.[234] The aims of this Chapter were to 1) investigate the potential of using an imaging analysis to describe the dissolution process of ibuprofen powder in the USP 2 paddle apparatus, 2) explore drug precipitation *in vitro* by directly decreasing the pH of an

ibuprofen solution and 3) conduct a preliminary investigation into the potential to use an online imaging system to visualize crystal formation and growth.

The dissolution test set-up consisted of a commercially available USP 2 paddle apparatus and attached imaging Mini-cell LED Inflow Canty™ system. Both pieces of equipment were described in Chapter 1, section 1.1.4.1, Chapter 2, section 2.2.1.3.2 and 2.2.1.6.2, respectively. A schematic visualization of the system is presented in Figure 6.1.

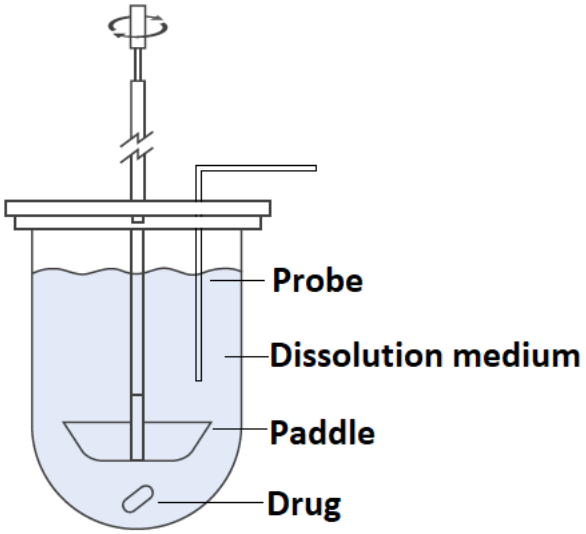

Figure 6.1:Schematic of the USP 2 paddle apparatus equipped with a probe part of the Mini-cell LED Inflow Canty™ imaging system.

6.2. Materials and methods

Dissolution testing of ibuprofen in PB 0.005% w/v (low) and 0.05% w/v (high) Tween 20, section 2.2.1.1.1 was performed in the USP 2 paddle apparatus, section 2.2.1.3.2. Samples were filtered and analysed by UV spectrophotometry, section 2.2.1.5.1. Precipitation testing of pre-dissolved ibuprofen was performed directly in the USP 2 dissolution vessel, section 2.2.1.4.2. Images of the process were recorded by using the

Mini-cell LED Inflow Canty™ camera and further analysed by the built-in analytical software, section 2.2.1.6.2.

6.3. Results and discussion

6.3.1. Imaging of a dissolution process

According to the USP solid oral forms are considered very rapidly dissolving when >85% of the mass used for dissolution is dissolved in 15 minutes.[52] The dissolution tests in PB 0.005% w/v Tween 20 (50 and 100 rpm) show slightly slower dissolution rate compared to those in PB 0.05% w/v Tween 20 in the first few minutes of the tests (Figure 6.2). As all dissolution tests were completed within 15 min, distinction between the surfactant concentrations or the paddle rotation speed was not possible.

Since the ibuprofen dissolves quickly, only the imaging data for the first 10 minutes of each test is presented (Table 6.1). In all cases, a low number of particles was detected. As the particles were diluted in the medium volume used, the probability of withdrawing particles in the medium sample was low. A slower dissolution rate would allow a longer detection time since the particles would be present in the test vessel for longer before their complete dissolution. The highest number of detections was registered during the dissolution with lower surfactant concentration, where the dissolution profile showed the slowest dissolution rate (Figure 6.2). As discussed in Chapter 1 and 3, ibuprofen shows poor wettability, and it is prone to agglomeration; these factors most likely contributed to the low detection rate. The Mini-cell LED Inflow Canty™ system specifications dictate that lens distance should exceed three times the maximum particle size; the used experimental set-up used a maximum lens distance of 850 µm, which lead to an expected particle size range <300 um, which correlates well with the observed results (Table 6.1 and Figure 6.3). The maximum particle size detected was 351.6 µm in PB 0.005% w/v Tween 20 at 100 rpm. A larger lens distance would allow larger particles to be sized, although the smaller particles would not be captured. This limitation made the existing imaging set-up unsuitable to detect agglomerations occurring in the paddle apparatus due to their typically large size. Furthermore, the collected data was not enough to describe the dissolution

process due to lower particle detection rate and fast dissolution. Another major limitation was the lack of image replicates. To confirm the observed results the tests need to be repeated, thus more replicates to be collected.

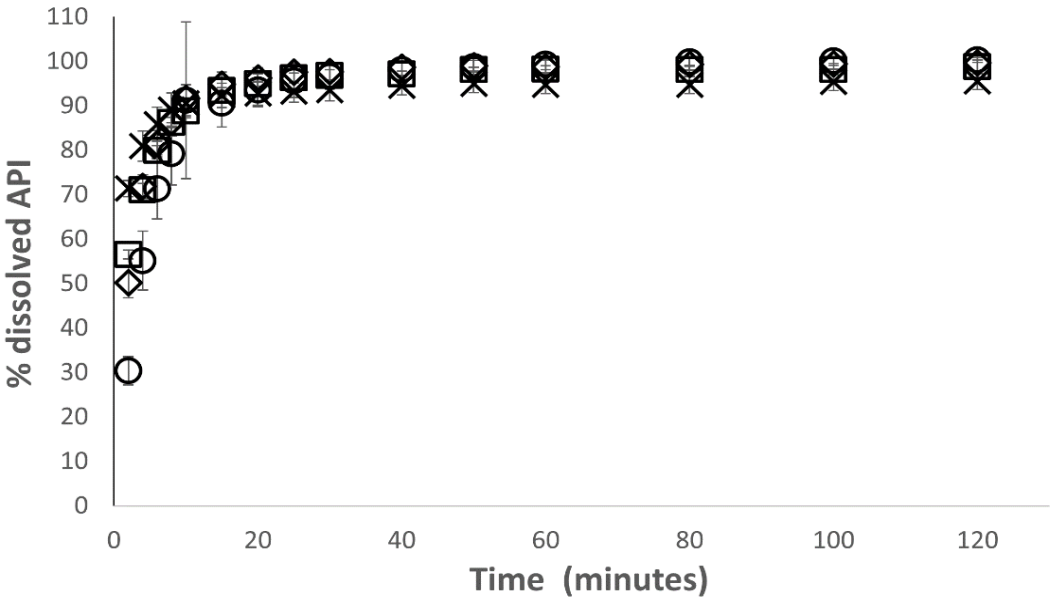

Figure 6.2: Dissolution profile of 250 mg ibuprofen dissolved in PB 0.005% w/v (circles and diamonds) and 0.05% w/v (squares and crosses) Tween 20 in paddle apparatus at 50 (circles and squares) and 100 rpm (diamonds and crosses).

Table 6.1: Particle characteristics detected by Canty™ Mini-cell LED Inflow and CVIA software during dissolution in PB 0.005% w/v (low) Tween 20 and PB 0.05% w/v (high) Tween 20 in the USP 2 paddle apparatus at 50 and 100 rpm.

	Time (min)	No. of detections	Average minimum diameter (µm)	Average maximum diameter (µm)	Aspect ratio	Circularity
PB low, 50 rpm	2	10	8.2	19.5	1.6	0.94
	4	33	4.8	9.7	1.5	0.96
	6	10	3.2	4.6	1.5	0.96
	8	8	2.8	3.9	1.3	0.98
	10	0	0	0	0	0
PB low, 100 rpm	2	6	4.9	9	1.4	0.95
	4	8	7.1	39.5	3.8	0.80
	6	5	3.5	4.4	1.3	0.98
	8	4	3.7	4.9	1.3	0.98
	10	0	0	0	0	0
PB high, 50 rpm	2	6	5.3	8.6	1.5	0.96
	4	5	13.3	69.1	2.3	0.90
	6	4	3	3.5	1.1	0.99
	8	2	3.1	4.2	1.3	0.98
	10	2	5.1	9	1.7	0.94
PB high, 100 rpm	2	8	3.8	7.9	2.1	0.90
	4	6	7	10.7	1.6	0.96
	6	4	6.7	14.4	2.2	0.88
	8	0	0	0	0	0
	10	2	4.4	7.2	1.6	0.95

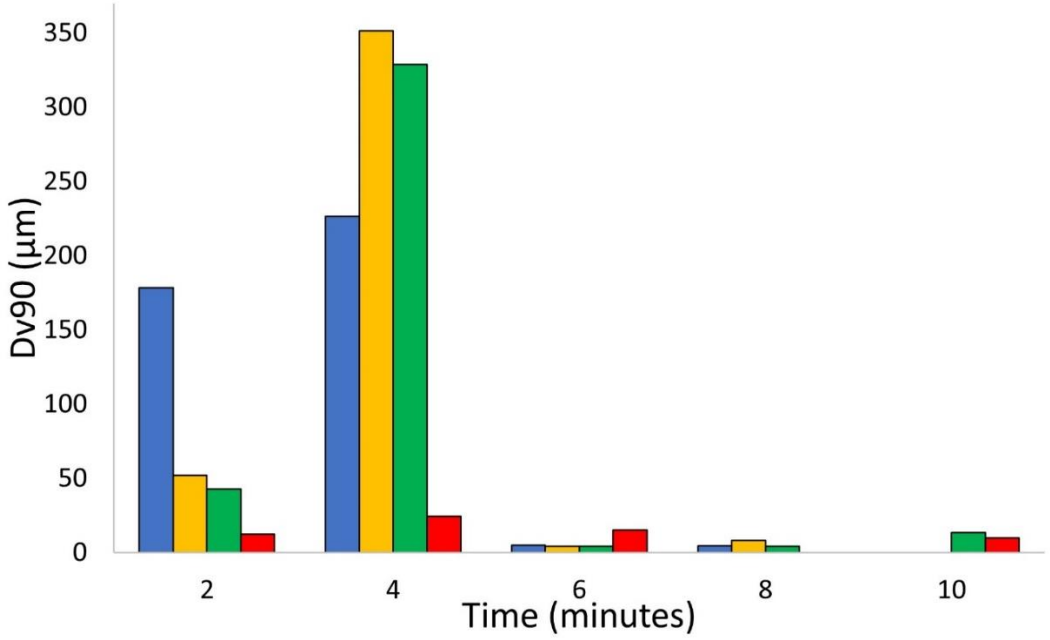

Figure 6.3: Particle size distribution Dv90 over time of ibuprofen dissolved in PB 0.005% w/v Tween 20 at 50 rpm (blue) and 100 rpm (yellow) and PB 0.05% w/v Tween 20 at 50 rpm (green) and 100 rpm (red).

6.3.2. Imaging of a precipitation process and crystal growth

Precipitation was observed instantaneously after mixing the ibuprofen solution and the HCl in the dissolution vessel. A milky solution formed straight after mixing in all tests, except for the control. In the first few minutes of the test, the newly formed particles were circular and appeared like grains (circularity 80 – 90%) (Table 6.2). Needle-shaped crystals started to form after 3 – 5 minutes of the test in all solutions (Figure 6.4). The aspect ratio of the detected particles suggests needle-shaped or elongated crystals. An increase in the particle size volume distribution under 50% and 90% (Dv50 and Dv90) is observed after the 5th minute of each test. At the end of the tests these two parameters are levelling to more constant values. Particle maximum diameter, aspect ratio and circularity also became relatively constant after 180 minutes. A smaller diameter and aspect ratio was observed for precipitates from the 0.5 mg/mL solution, as well as a higher circularity compared with 1 and 2 mg/mL. A

reason for this could be the formation of shorter crystals due to low drug concentration. Very few particles were detected after 60 minutes of the control test, reaching a maximum of 18 particles detected at 180 minutes. The origin of these particles is unclear. A hypothesis that was considered was salt formation between the PB and HCl or external contamination, *e.g.*, a fibre as ibuprofen particles were formed at early times. However, particles were not isolated to confirm their origin. Currently, it is not clear what would be the impact of such particle formations on an ibuprofen-containing experiment and if these particles were formed due to contamination or they form during every test. Thus, another control test could be conducted and in case of particle formation, they could be extracted and analysed.

The effect of the camera lens distance was explored during the precipitation of 1 mg/mL ibuprofen between the 12^{th} and 17^{th} minute of the test when needle-shaped crystals were already formed (Figure 6.5). Although the number of particles present in the test vessel was similar, the detections at 25 and 250 µm were 119 and 178, respectively; at 50 and 200 µm detections were higher – 439 and 397, respectively; and the two average distances (100 and 150 µm) showed the higher detection rate of 621 (100 µm) and 609 (150 µm) particle detections. There are more particles captured at the two highest distances, however, the system does not count particles that are not in focus. These out of focus particles increase the background noise level which can lead to false positive results. A balance between particle detection and image sharpness is needed for accurate crystal growth investigation.

Table 6.2: Number of particles detections, minimum and maximum particle diameter, aspect ratio, elongation factor, circularity and size distribution (Dv50 and Dv90) recorded for each time point of the precipitation of ibuprofen 0, 0.5, 1 and 2 mg per mL dissolved in PB 0.05% w/v Tween 20 after mixing in ratio1:1 with 0.2 N HCl in the USP Paddle apparatus vessel at constant stirring of 50 rpm. Likely outliers are marked in red.

	Time (min)	Npd	Min. diameter (µm)	Max. diameter (µm)	Aspect ratio	Elongation factor	Circularity	Dv50 (µm)	Dv90 (µm)
0 mg/mL (control)	**1**	0	0.0	0.0	0.0	0.0	0.0	0.0	0.0
	5	1	11.8	21.0	1.8	1.5	0.9	21.0	21.0
	10	0	0.0	0.0	0.0	0.0	0.0	0.0	0.0
	20	0	0.0	0.0	0.0	0.0	0.0	0.0	0.0
	60	5	7.5	27.6	3.7	1.8	0.7	27.3	29.2
	180	18	7.2	26.8	3.7	1.6	0.7	28.9	29.9
	210	9	7.1	27.2	3.8	1.6	0.7	29.0	29.8
0.5 mg/mL	**2**	1	8.9	17.4	2.0	1.6	0.9	17.4	17.4
	3	960	4.3	18.8	4.1	3.3	0.8	64.3	157.4
	5	3176	4.6	33.9	7.2	4.7	0.6	96.5	268.3
	30	1053	4.8	36.8	7.9	5.0	0.6	92.5	214.1
	60	1352	5.2	40.3	8.0	4.7	0.6	106.8	226.7
	180	3066	4.0	14.4	2.8	2.1	0.9	162.5	427.3
	240	3034	4.3	14.5	2.8	2.1	0.9	168.6	387.1
	300	2379	4.9	20.5	3.3	2.4	0.9	203.9	375.7

	Time (min)	Npd	Min. diameter (µm)	Max. diameter (µm)	Aspect ratio	Elongation factor	Circularity	Dv50 (µm)	Dv90 (µm)
1 mg/mL	2	380	2.0	31.8	7.6	1.8	0.9	493.0	859.3
	3	104	5.3	227.4	41.0	2.4	0.3	3397.0	3397.0
	5	61	3.3	13.1	4.0	2.1	0.8	36.9	46.2
	30	6760	4.8	28.4	6.1	5.2	0.6	85.1	169.4
	60	3535	5.0	27.5	5.7	5.2	0.7	86.8	234.8
	180	2268	5.6	32.8	6.2	5.0	0.7	113.2	215.5
	240	3431	5.8	31.8	5.8	4.9	0.7	117.1	240.4
	300	3815	5.9	31.7	5.8	4.9	0.7	119.4	238.5
2 mg/mL	2	6616	3.9	17.6	4.0	2.7	0.8	177.0	379.2
	3	6661	4.4	25.3	5.7	3.9	0.7	135.0	471.5
	5	5979	4.4	25.3	5.8	4.0	0.7	100.7	253.3
	30	2982	5.2	38.0	7.7	3.6	0.6	138.2	246.5
	60	1430	6.6	74.1	11.3	3.2	0.5	642.9	999.1
	180	1975	6.4	51.1	8.3	3.3	0.6	263.8	663.3
	240	1329	6.6	48.3	8.1	3.3	0.6	208.2	376.7
	300	2314	6.5	43.3	7.4	3.3	0.6	219.7	430.2

	Time (min)	Npd	Min. diameter (µm)	Max. diameter (µm)	Aspect ratio	Elongation factor	Circularity	Dv50 (µm)	Dv90 (µm)
0 mg/mL (control)	**1**	0	0.0	0.0	0.0	0.0	0.0	0.0	0.0
	5	1	11.8	21.0	1.8	1.5	0.9	21.0	21.0
	10	0	0.0	0.0	0.0	0.0	0.0	0.0	0.0
	20	0	0.0	0.0	0.0	0.0	0.0	0.0	0.0
	60	5	7.5	27.6	3.7	1.8	0.7	27.3	29.2
	180	18	7.2	26.8	3.7	1.6	0.7	28.9	29.9
	210	9	7.1	27.2	3.8	1.6	0.7	29.0	29.8
0.5 mg/mL	**2**	1	8.9	17.4	2.0	1.6	0.9	17.4	17.4
	3	960	4.3	18.8	4.1	3.3	0.8	64.3	157.4
	5	3176	4.6	33.9	7.2	4.7	0.6	96.5	268.3
	30	1053	4.8	36.8	7.9	5.0	0.6	92.5	214.1
	60	1352	5.2	40.3	8.0	4.7	0.6	106.8	226.7
	180	3066	4.0	14.4	2.8	2.1	0.9	162.5	427.3
	240	3034	4.3	14.5	2.8	2.1	0.9	168.6	387.1
	300	2379	4.9	20.5	3.3	2.4	0.9	203.9	375.7
	2	380	2.0	31.8	7.6	1.8	0.9	493.0	859.3
	3	104	5.3	227.4	41.0	2.4	0.3	3397.0	3397.0
	5	61	3.3	13.1	4.0	2.1	0.8	36.9	46.2
	30	6760	4.8	28.4	6.1	5.2	0.6	85.1	169.4

	60	3535	5.0	27.5	5.7	5.2	0.7	86.8	234.8
	180	2268	5.6	32.8	6.2	5.0	0.7	113.2	215.5
	240	3431	5.8	31.8	5.8	4.9	0.7	117.1	240.4
	300	3815	5.9	31.7	5.8	4.9	0.7	119.4	238.5
	2	6616	3.9	17.6	4.0	2.7	0.8	177.0	379.2
	3	6661	4.4	25.3	5.7	3.9	0.7	135.0	471.5
	5	5979	4.4	25.3	5.8	4.0	0.7	100.7	253.3
	30	2982	5.2	38.0	7.7	3.6	0.6	138.2	246.5
	60	1430	6.6	74.1	11.3	3.2	0.5	642.9	999.1
	180	1975	6.4	51.1	8.3	3.3	0.6	263.8	663.3
	240	1329	6.6	48.3	8.1	3.3	0.6	208.2	376.7
	300	2314	6.5	43.3	7.4	3.3	0.6	219.7	430.2

	Time (min)	Npd	Min. diameter (µm)	Max. diameter (µm)	Aspect ratio	Elongation factor	Circularity	Dv50 (µm)	Dv90 (µm)
1 mg/mL	**2**	380	2.0	31.8	7.6	1.8	0.9	493.0	859.3
	3	104	5.3	227.4	41.0	2.4	0.3	3397.0	3397.0
	5	61	3.3	13.1	4.0	2.1	0.8	36.9	46.2
	30	6760	4.8	28.4	6.1	5.2	0.6	85.1	169.4
	60	3535	5.0	27.5	5.7	5.2	0.7	86.8	234.8
	180	2268	5.6	32.8	6.2	5.0	0.7	113.2	215.5
	240	3431	5.8	31.8	5.8	4.9	0.7	117.1	240.4

2 mg/mL	**2**	6616	3.9	17.6	4.0	2.7	0.8	177.0	379.2
	3	6661	4.4	25.3	5.7	3.9	0.7	135.0	471.5
	5	5979	4.4	25.3	5.8	4.0	0.7	100.7	253.3
	30	2982	5.2	38.0	7.7	3.6	0.6	138.2	246.5
	60	1430	6.6	74.1	11.3	3.2	0.5	642.9	999.1
	180	1975	6.4	51.1	8.3	3.3	0.6	263.8	663.3
	240	1329	6.6	48.3	8.1	3.3	0.6	208.2	376.7
	300	2314	6.5	43.3	7.4	3.3	0.6	219.7	430.2

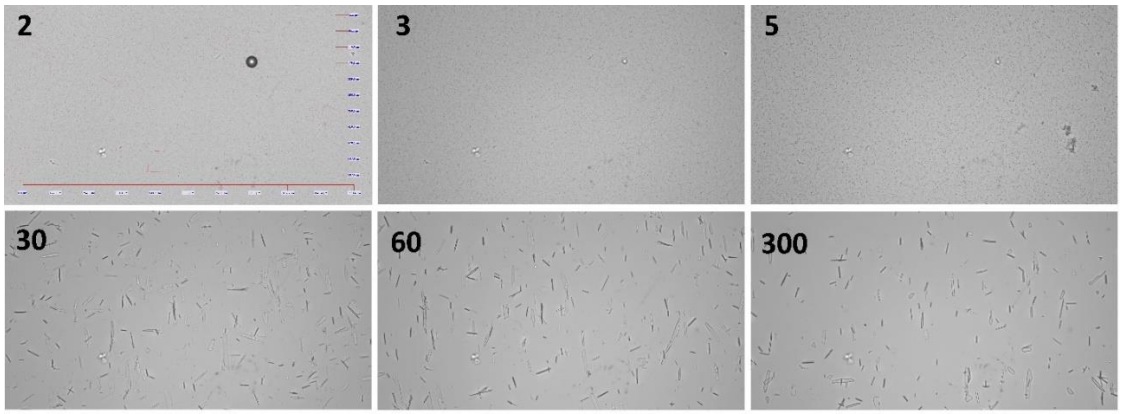

Figure 6.4: An example of the ibuprofen crystal growth observed in the USP 2 paddle apparatus after direct mixing of ibuprofen:PB 0.05% w/v Tween 20 solution 1 mg/mL and 0.2N HCl, ratio 1:1. Images taken after 2, 3, 5, 30, 60 and 300 minutes after mixing.

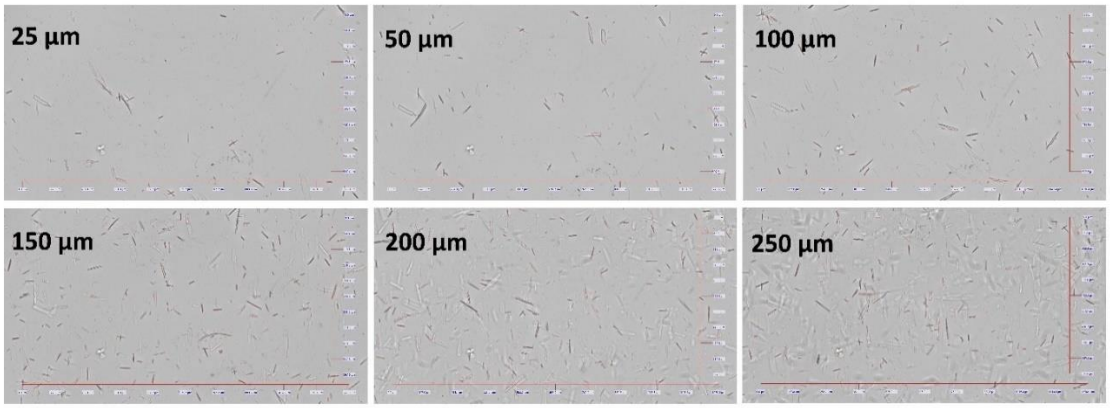

Figure 6.5: Crystal detection after precipitation of 0.1 mg/mL ibuprofen dissolved in PB 0.05% w/v Tween 20 and mixed with 0.2N HCl ratio 1:1 and constant stirring of 50 rpm in the USP paddle apparatus vessel at camera lens distance in the range 25 – 250 µm.

The possibility to mimic *in vitro* processes observed *in vivo* would be beneficial for future drug product development and optimization. A simple monitoring tool such as an optical imaging system could be implemented on a much broader basis in oral drug development, while to investigate drugs which are very prone to precipitation, implementation of much more sophisticated tool might be needed.[60] Nowadays, AI and more specifically NNs are being used to advance such tools and elevate their performance.[163], [235], [236]An imaging system attached to the dissolution vessel

and equipped with analytical software could characterize particles during dissolution providing information on their size, shape and behaviour. There is potential for such a tool to be used during dissolution of formulations or release testing to distinguish between excipients and APIs or as a discriminatory tool for generic formulations in biowaiver studies. Crystal formation and growth could be visualized, and crystal habit could be investigated in solution. This might be important during preparation and testing of amorphous solid dispersions due to the common instability phenomenon where the drug conversion from an amorphous to a crystalline form is observed.[72], [237]

Some limitations of the imaging method as it is, need to be discussed such as the lack of replicates, the need for a reference data base and the necessity for a high number of particles seeded in the test vessel. The imaging probe is connected to only one of the dissolution vessels while for dissolution at least three replicates are done simultaneously.[8] Thus, to confirm the results, the test needs to be repeated to collect more replicates, or probes need to be attached to all test vessels. The system needs to be configured according to the particles that are going to be investigated. In this way the software could better "recognize" them based on the expected shape. The system allows detected particles to be classified into manually created classes, *e.g.*, "ibuprofen", "excipient A", "excipient B", thus a classification file could be created which ideally would be able to automatically classify detected particles from formulations. Dissolution of formulations such as tablets would produce higher number of particles for detection due to the presence of multiple components, mostly excipients, except when very high drug loading is used, as shown by Wilson *et al.*[101]. The existing classification file was able to distinguish between two classes – solids and air bubbles. When transparent particles would be investigated such as crystals or oil droplets, the background could be changed to provide better separation. In this current work, it was found that the detection of particles strongly depends on two factors – 1) number of particles present in the vessel and 2) lens distance. In the case where 250 mg of ibuprofen powder were dispersed and dissolved in 500 mL of medium, the number of particles reaching the camera was negligibly low (Table 6.1), while when the same drug mass was pre-dissolved in 250 mL of medium (1 mg/mL

initial concentration) and mixed with 250 mL of a precipitation agent (HCl), thousands of growing particles with small size were captured (Table 6.2). Currently, small particles under 300 µm could be better captured with the camera lens distance used while large particles in the upper end of the detection range is more likely to be missed.

6.4. Conclusion

Dissolution and precipitation processes of ibuprofen were visualized in the USP 2 paddle apparatus. Dissolving particles and crystals growing from a solution were captured and characterized. The potential to use imaging to characterize the effect of different surfactant concentrations and a change of the paddle rotation speed were investigated during dissolution testing. The imaging system showed a potential to distinguish between dissolution profiles, however a prolonged dissolution time is needed for more particulate images to be generated. There is scope to use the built-in AI software for further API/excipient classification, crystal habit investigation and amorphous solid dispersion precipitation tendency.

Crystal formation following pH-induced precipitation in the paddle apparatus was successfully visualized from instantaneous grain formations to crystals with a specific shape (needles) determined visually and by the aspect ratio of the crystals. The number of particles and their size were automatically detected. At the end of each test several parameters such as number of detected particles, Dv, aspect ratio and circularity were levelling to more constant values. The specific shape was confirmed by the particles' aspect ratio and the obtained images.

Some important limitations such as lack of image replicates required further method development. As this is a preliminary study, more experiments would be needed to confirm the presented results and to fully understand the possible applications of this imaging system. There are no replicates of the presented precipitation studies. Also, there are no image replicates of the dissolution tests, although dissolutions were conducted in triplicate. Hence, at this stage the author is

unable to draw more definite conclusions. A direction for a future work could be investigation of the dissolution of formulations with a mass above 250 mg and presence of excipients to increase the number of particles in the vessel; training new classification categories to distinguish API particles and excipients or crystal habits; to mimic drug precipitation that may occur *in vivo* by using a weak base instead of a weak acid (ibuprofen) due to the physiological transition in the gastro-intestinal tract from more acidic to more basic environment.

Chapter 7: General discussion

7.1. *In vitro* dissolution testing

7.1.1. Biorelevant media, hydrodynamics and physiologically based pharmacokinetic (PBPK) modelling and *in vitro-in vivo* correlation

Over recent decades, the use of dissolution testing shifted from purely a quality control tool to prediction of *in vivo* drug performance, establishing *in vitro-in vivo* correlations, identification of potential bioavailability issues and a critical test in generic bioequivalence/biowaiver studies. It is known that physiological factors such as pH, surface tension, solubilisation, buffer capacity, the GI volume and food ingestion play a vital role in drug release and absorption *in vivo*.[234] The advances in the development of biorelevant media[17], [238], which reflect the main properties of the GI fluids, simulations of GI motility, residence time and hydrodynamics[60], [239] improved the understanding of critical *in vitro-in vivo* relations for immediate and modified release formulations[204]. It is known now that the human intestinal fluids contain higher concentrations of lipids and surfactants (*e.g.*, phospholipids) in a fed state compared to a fasted state. These components delivered with food or produced by the body, can increase the solubilization of poorly soluble drugs and thus, improve their bioavailability.[206] Addition of surfactants in simple dissolution media (*e.g.*, PB) is a common technique used to mimic GI drug dissolution. Another important characteristic of the biorelevant medium (buffer capacity) was investigated by Matsui *et al.*[240]. They express their concerns regarding the lower buffer capacity of the intraluminal fluids than the buffer capacity of the *in vitro* compendial dissolution media and the effect of dissolution testing performed in highly buffered media on the predictability of *in vivo* drug performance.[240] Mudie *et al.* realized the challenges of choosing an appropriate dissolution medium after the emergence of biorelevant media with a variety of properties and compositions on the market. They presented a methodology for selecting a practical physiologically relevant medium that is

representative of a fasted state for dissolution evaluation of immediate release formulations.[241] Furthermore, this knowledge and *in vitro* dissolution data are used as an input in physiologically based pharmacokinetic (PBPK) prediction models where different factors affecting drug performance *in vivo* are integrated. PBPK and biorelevant dissolution testing were applied in formulation development, to predict drug solubilization and precipitation behaviour *in vivo* and to support regulatory decision-making. Furthermore, the possibility to extend BCS-based biowaivers to include poorly soluble drugs Class II was investigated.[86], [206], [239], [242]

This current work contributes towards understanding of the effect of media composition on dissolution testing by investigation of the addition of small amounts of surfactant to PB. Measured solubility showed a minor increase, while the SGI analysis showed improved particle dispersal during dissolution, consequently an increased dissolution rate. Kim *et al.*[243] demonstrated improved particle wettability and reduced agglomeration tendency by dry coating of micronized poorly wettable particles with hydrophobic or hydrophilic nano-silica coating. Here, the same effects were demonstrated by addition of surfactant where the low surfactant concentration resulted in detection of particles for a longer time and slight increase in the dissolution rate, while the higher surfactant concentration led to detection of thousands of particles (compared to hundreds at the lower surfactant concentration) for shorter time (approx. 10 minutes) and overall faster dissolution rate. Hence, it was shown that addition of surfactant could visibly improve drug dissolution performance, which could be a promising strategy to discriminate between generic products or to confirm batch-to-batch consistency. Other parameters related to the dissolution process (*e.g.*, FR) and the drug (*e.g.*, mass, crystal habit) were also investigated as they could be critical for a biorelevant dissolution testing. In agreement with the QbD framework[31], the identification of the critical material attributes and critical process parameters that mostly influence the product performance is needed. Thus, in this current work, it was shown that in the case of powder dissolution in the USP 4 FTA, an increase of the FR leads to slight increase in the dissolution rate. On the other hand, an increase of the mass used for dissolution slows the dissolution rate and increases the potential of agglomerate formations due to the limited space in the test cell. The

aggregation particle behaviour during dissolution was widely investigated.[64], [94], [207], [243] However, this is the first time when SGI was used to detect and characterize agglomerates occurring during dissolution. Acknowledging the limitations of the SGI to distinguish overlapping single particles from agglomerates; the effect of particle position in the cell on the size detection; and the effect of the cell volume on the depth of focus – SGI provided a satisfactory amount of information to develop a prototype of an automated tool for agglomerate detection which gives a possibility to reduce the labour-intensive and time-consuming manual video observation and labelling of agglomerates.

7.1.2. Drug precipitation

Kostewicz *et al.*[234] investigated the precipitation tendency of weak bases when they are transferred from the stomach to the small intestine. In his study he used the drug concentration-time relationship to investigate *in vitro* the precipitation tendency of poorly soluble weak bases in the small intestine due to supersaturation. He concluded that the supersaturation phenomenon cannot be predicted by solubility or dissolution experiments *in vitro* due to higher concentrations registered *in vivo* as a consequence of the drug absorption rate and that the drug is more likely to precipitate *in vivo* where there is a fast transition between different parts of the GI tract.[234] To gain further insight into the precipitation behaviour of weak bases *in vivo* and the nature of the precipitates, several groups compared *in vitro* data with *in vivo* results retrieved from rats.[244], [245] Others used *in silico* methods to simulate the precipitation of poorly soluble drugs and to evaluate the impact on the bioavailability.[59], [246] In more recent years, UV optical analysis has been applied as a real time monitoring tool which enables the assessment of a dissolution process and the observation of phenomena such as *in vitro* precipitation.[115], [116], [247] Sun *et al.*[247] used a custom-made flow-through cell to observe the dissolution, supersaturation and precipitation of piroxicam (BCS Class II), while Kuentz *et al.*[116] presented small-scale dissolution and precipitation tests in a commercial non-

pharmacopeial µFLUX apparatus (pION Inc.). In this current work, two optical methods for weakly acidic drug precipitation in pharmacopeial paddle (USP 2) and flow-through (USP 4 CE1) apparatuses by direct imaging in real time were investigated. For instance, direct optical imaging does not require a specific wavelength and the images could be observed directly in real time without further manipulation of the results. The first method investigated a slow medium change in the USP 4 FTA where a solution of the drug was filled into the test cell (either pre-dissolved or after conducting a dissolution test), hence the medium in the reservoir was changed with a medium with lower pH to initiate drug precipitation. Thus, two stages of drug precipitation were observed – plume formation (early stage) which occurred instantaneously and particle reformation (late stage). The second method investigated the precipitation of pre-dissolved drug with known concentration (below saturation) after direct mixing with a low pH solution (HCl) in the dissolution vessel. An optical probe with a micro lens (Mini-cell LED Inflow Canty™) was used to observe the early stage of crystal formation (grains) and the following crystal growth (needles). The resolution and the quality of the images obtained with the micro lens were of significantly higher quality compared to the SGI camera. However, limitations such as change in the hydrodynamics in the vessel, blockage of the probe and crystals stuck between the lens and the light source should be considered. On the other hand, due to the lower SGI camera resolution, the grain stage of the precipitation could not be visualized. A plume of milky-like fluid (cloudy formation with different refractive index than the solution) was observed in the test cell. This information was sufficient to observe a change occurring in the test cell, however there is room for further improvement of the equipment.

7.2. Imaging as a process analytical technology (PAT) real time monitoring tool

In recent years, the QbD concept for real time monitoring[95] and the potential for real time release testing[248] gained a lot of interest in the pharmaceutical

industry.[249] A recent paper by Sacher *et al.* acknowledges the advances of PAT to monitor many critical quality attributes, however, it also points out the lack of suitable techniques for implementation to dissolution testing which would tackle two of the limitations related to dissolution – the extensive testing time and the destructiveness of the offline method.[250] Mészáros *et al.*[249] discussed particle size as another critical parameter which could affect the *in vitro* dissolution of the final products. They advocate that imaging technologies have the capability to analyse challenging samples which can serve as at-line, non-destructive techniques with multiple advantages over microscopic particle size measurement.[249] Such imaging techniques were developed and exploited for dissolution testing mainly of solid dosage forms (tablets). MRI can provide an insight into the hydration of a tablet during dissolution as it maps the water molecules and movement, which offers a possibility to quantify tablet dimensions due to hydration. Thus, this method provides the potential to observe the effects of hydration like water penetration, gel formation and tablet swelling.[251] Raman and FTIR spectroscopic imaging are similar fast physicochemical imaging techniques which use the molecular vibrations in molecules to obtain information on the chemical structure of the formulation. Raman spectroscopy relies on the photons' interaction with the formulation to produce a map of the tablet composition.[156], [252] On the other hand, FTIR spectroscopy is dependent on a change in the dipole moment during vibration thus water appear strongly in the IR absorption spectrum compared to Raman spectroscopy.[253] A draw back from the Raman imaging spectroscopy is that to work successfully this technique needs a special flow-through cell where the sample is static[252] making it unsuitable for use in conjunction with standard dissolution apparatuses. Furthermore, the static position of the sample would influence the dissolution process by limiting the surface area exposed for dissolution, and would also affect the relative fluid velocity to which the dissolving surface is exposed, *i.e.*, hydrodynamic implications. Galata *et al.* [156] comments that although Raman and near infrared (NIR) imaging are also similar, NIR imaging allows faster measurements than Raman imaging, however NIR spectroscopy has a lower spatial image resolution, thus it might be more difficult to differentiate between excipients in drug formulations such as HPMC. So far, UV imaging is the closest technique to the ones used in this current work, which provides insight into drug dissolution processes such as diffusion,

tablet swelling, drug crystal growth and precipitation in a non-pharmacopeial commercially available flow-through set up.[115], [254] Since most UV-Vis instruments use the light of a single wavelength, it could be challenging to distinguish the absorption of the dissolved drug from the scattered light by the solid particles.[252] This could be particularly challenging in complex formulations containing multiple excipients. Li *et al.* [255] investigated the potential to develop a dual wavelength imaging technique to provide functional characterisation of excipients in solid oral dosage forms. However, to the best of the author's knowledge, there are currently no published studies where pharmacopeial dissolution apparatuses and a non-destructive real time imaging techniques are used for API and formulation characterization.

7.2.1. Shadowgraph imaging (SGI) and image analysis in the USP 4 FTA

In this current work, the dissolution behaviour of ibuprofen as a weakly acidic API was investigated under various conditions depending on surfactant concentration, mass, FR and crystal habit. By using SGI, particles were sized based on an internal calibration. The average particle size from all tests, where un-sieved powder was used, was in the range between 100 and 200 µm which is in a good agreement with the size defined by using the offline particle size analysis (162 µm) in wet mode (Chapter 3, section 3.3.1.3). SGI could detect more particles when they were better dispersed at higher surfactant concentrations (0.005% w/v and 0.05% w/v). The FR had a minor effect on the particle dispersal, thus there was not major differences in the particle detection rate when surfactant was not added to the medium. On the other hand, a higher mass used for dissolution resulted in more particles available for detection for longer time. The dissolution rate decreased with the increase of the mass. Hence, there was an increase in the detection rate and the time of detection. This phenomenon is well observed at the lower surfactant concentration, where the surfactant enhances the dispersion, thus improving particle detection without significantly affecting the solubility. Furthermore, the resolution of the SGI camera was

sufficient to discern between crystal habits (plates and needles). Other objects such as air bubbles and agglomerates were also well defined. In the case where sieved fractions were used, the FR had a clearly observable effect on the particle dispersal, thus particles were detected for longer under the same dissolution conditions as the un-sieved particles as shown in Chapter 3. Some limitations related to the SGI set-up should be noted. SGI was conducted in the USP 4 FTA CE1 which required dissolution tests to be done in parallel in the CE7 (triplicate). A custom-made water jacket and cell holder suitable for the standard USP 4 FTA CE7 had to be made and the SGI set-up had to be installed to fit the larger dissolution apparatus. These changes were done during the time of this project and the new SGI/CE7 set-up was used to conduct the dissolutions and imaging of the suspension products. During the current project SGI was trialled with the suspension formulations, but this proved to be challenging due to inability to accurately distinguish between the ibuprofen particles and the excipients. The refractive index of the transparent matrix components and transparent suspended drug particles were too close for a proper separation, thus the system captured only particles from the viscous fingers or separated from the suspension layer. However, most of the detections were inaccurate and therefore not investigated further with the current set-up and methods.

Although acquisition of dissolution results in triplicate and imaging at the same time was possible after the modifications of the USP 4 FTA CE7, the limitation of having images from only one of the test cells remain. To enable replicates and quantify how variability in dissolution is represented, but also variability in SGI itself, an SGI set-up could be connected to each test cell. A challenge that may arise from such change in the equipment could be how the data to be aggregated and processed together. Other issues related to insufficient imaging resolution result in imaging limited to particles above 20 µm and inaccurate particle sizing if the particle is positioned in front or behind the focus plane. Possible ways to overcome these limitations could be improvement in the camera magnification and resolution, or a change of the LED light source with a laser. However, while the related hazards and the extra cost of the equipment should be considered, the use of laser or installation of a second camera under a specific angle could be beneficial to better define particle shape. Furthermore,

validation methods need to be developed depending on how quantitative data is to be deployed. However, due to the test cell shape and size the improvement possibilities are limited.

7.2.2. An alternative dissolution imaging system used in combination with the USP 2 paddle apparatus

The un-sieved ibuprofen powder was also investigated in the paddle apparatus equipped with the Mini-cell LED Inflow Canty™ camera. Although, the camera allows particles small as 0.7 µm to be imaged, a powder sample of 250 mg dispersed in the whole medium volume (500 mL) was not enough mass for good particle characterization. Very few particles were withdrawn by the probe and transported to the camera window for detection. Thus, the information provided was not sufficient to describe the dissolution process or to characterize any changes in the particle size and behaviour. Moreover, the dissolution in the paddle apparatus was very rapid (10 min), thus the time for particle observation was limited. The imaging system was more useful to capture precipitation where the same mass of drug precipitated into multiple small size particles. To describe the dissolution process, the system would be more suitable in cases of slow dissolution, *e.g.*, ibuprofen dissolving in an acidic medium; higher mass of micronized particles used for dissolution or formulations where the added excipients would provide more particles for detection. This would increase the number and time of detections, thus more data would be collected, which could be further applied into PBPK modelling and simulations.[202] Collection of more data would allow also investigation of the impact of hydrodynamics on detection.

7.2.3. Imaging of formulations in the USP 4 FTA

When it comes to formulations, solid oral dosage forms (*e.g.*, tablets) get much more attention than other formulations as they are the most commonly used dosage

form.[102], [137], [238], [256]–[260] Although dissolution tests were initially developed for immediate- and then for modified-release tablets, the emergence of different dosage forms that aim to meet various patient needs (*e.g.*, suspensions, orodispersible tablets, chewable tablets, suppositories), increased the need to find a better way to characterize the *in vitro* release from these dosage forms.[81] From a biopharmaceutical perspective, suspensions correspond to the post-disintegration stage of the solid dosage forms. Thus, for them dissolution is also a rate-limiting step for absorption and bioavailability with a chance for *in vitro-in vivo* correlations.[77] Currently, the most common approach for suspension testing is the use of the rotating paddle method[4], [81], where suspensions dissolve in less than 30 minutes.[77], [85] However, from a development and biowaiver perspective, a very rapid dissolution hides a risk of insufficient discrimination between products especially for poorly soluble drugs BCS Class II.[261] Matsui *et al.* discussed that dissolution testing which enables slow dissolution generally provides a high discriminatory power between formulations.[240]

Although dissolution testing in the USP 4 FTA is used for injectable suspension products, it is less commonly used for oral suspensions.[4] Van der Vossen *et al.*[239] performed dissolution testing of tablets and an oral liquid formulation (a solution) in a mini-paddle apparatus and the USP 4 FTA to best mimic the dissolution process in paediatric patients as their GI volumes are smaller than in adults. The aims of their study were to use drug-related factors (solubility and dissolution) in biorelevant media adapted to reflect the paediatric population and to investigate the impact of patient-related factors on drug performance.[239]

As the number of papers in the literature regarding dissolution or release testing of suspensions[61], [244], [262]–[265] is scarce and there are even fewer reports that involve imaging, in the current work the dissolution behaviour of paediatric oral suspensions during dissolution testing in the USP 4 FTA was investigated by direct imaging and AI image analysis. While a few papers discussing the imaging of injectable or in-house prepared suspensions were found,[64], [131], [139], [266], [267] none of them describes imaging of the dissolution process of commercially available oral suspensions. In the current work, two brands of paediatric oral suspensions were

tested in the small and large USP 4 FTA test cell. Videos during the tests were recorded and analysed. A good discrimination was observed between the two tested brands as one of the suspensions (B100/200) exhibited much slower dissolution than the other one (N100/200). Discrimination within the same brand was also possible, although not as obvious as amongst the brands. The suspensions of a lower strength dissolved faster than the higher strength of the same brand, possibly due to a lower mass suspended in the same volume. Imaging on the other hand, provided valuable visual information regarding the dissolution process and the suspension behaviour in the test cell.

One basic requirement of a good suspension is that the suspended particles remain suspended without settling during administration *in vivo* in order to enhance uniform and accurate dosing.[268] After transferring them into the test cell and during the whole dissolution process, samples behaviour was observed. Although the samples settled on the bottom of the cell on top of the bed of glass beads, drug particles remain dispersed within the suspension matrix which was also visible from the videos. Furthermore, phenomena such as viscous fingering, channelling[90]–[92] and expansion of the suspension matrix were captured.

Excipients swelling during tablet dissolution was investigated by using two imaging techniques (direct imaging and MRI).[103], [112], [269], [270] Felicijan *et al.*, Chen *et al.* and Rajkumar *et al.* investigated in-house prepared 100% HPMC tablets by direct imaging[103], [269] and MRI[270], while Zhang *et al.* used commercial fluvastatin tablets containing 30% w/w HPMC. During tablet dissolution the expansion of the excipients promotes tablet disintegration and water penetration inside the compact, thus it supports the drug release. In suspensions drug particles are dispersed in the suspending matrix, thus they cannot easily escape from the formulation. When the matrix expands more fluid penetrates through the formulation and gets in contact with the drug particles. This was observed from the dissolution profiles of all tested suspensions where after the matrix expansion, the percentage of drug dissolved quickly increased. When suspensions are tested in the paddle apparatus the speed of the paddle rotation can be controlled depending on the viscosity of the sample.[4], [81] In the flow-through cell mixing occurs due to the pulsing flow. It was found that a 16 mL/min flow cannot sufficiently mix the suspension and the sample lies on the

bottom of the cell (small and large). Thus, the upstream medium flow forms channels through the suspension on its way up. This provides additional contact areas between the fluid and the drug. In the case of the B100/200 formulation in the small test cell, the medium found an easier route around the formulation and passed mostly between the formulation and the wall of the test cell rather than through the formulation. This could suggest different hydrophilicity or polarity of the excipients, or an impact of excipients on the balance between cohesion and adhesion.

Andesson *et al.* explained in his work that the dissolution of solids is dependent on the contact area between the solid and the medium, *i.e.*, the surface area available for dissolution, and the hydrodynamics in the test vessel.[271] The flow of the fluid around the particles and the particle size were noted as the two main factors that affect the thickness of the diffusion boundary layer in a dissolution process and consequently, the dissolution rate.[271], [272] Real time monitoring of the suspension dissolution process allows different patterns in the channel formation and the suspension behaviour during dissolution to be observed. This presents the potential to use differences between generic products or different strengths within a brand to be used as a quality control or a bioequivalence tool in addition to the similarity factor (f_2)[258].

7.3. Computational methods and AI analysis

7.3.1. Development and application of NNs for prediction of in vitro dissolution profiles

Direct imaging provides an easy, inexpensive method for process observation. However, further image analysis and data interpretation could be a labour- and time-consuming task or to require a significant processing power. Computational image analysis methods have become easily accessible in commercially available software, such as SGI became easily accessible with platforms like Matlab™ or they are already built-in in commercially available software like CANTYVISION intelligent

analysis Canty™. SGI uses ML algorithms available in some of the Matlab™ toolboxes[157], [273] for image recognition, object detection and parameter calculation such as object size, position, orientation and velocity. In this way, SGI could be classified as a simple (low level) AI system as ML and DL are sub-sections of AI as described in the introduction of this work (Chapter 1). The SGI successfully captured changes during dissolution of powders and showed potential to be used as an in-line quality control tool. Moreover, the data collected and analysed by this method set a solid base for further development of other computational and classification methods, such as the AIM, able to detect agglomerates and possibly other specific phenomena with additional development according to the situation. On the downside, the limitations of the SGI method represented insurmountable challenges in more complex systems such as drug precipitation/crystal growth and dissolution of suspensions. The system was not able to recognize the drug particles either because of their small size (precipitation) or due to light scattering from the excipients in the suspension, thus more sufficient method was needed.

The ability of ANN to discern complex and latent patterns in the information presented to them was found back in the 90s[274], when computer power was not as advanced as nowadays and the NNs were not that well known. Achanta *et al.*[274] tried to identify areas in the pharmaceutical sciences where ANN could be successfully applied as according to the authors, there was a lack of pharmaceutical publications in the literature that use ANNs. Ebube *et al.* used ANN to investigate the ANN ability to predict the *in vitro* dissolution rate as a function of product formulation changes. Accordingly they trained the NN with sets of hypothetical and experimental data of formulations with known dissolution profiles and tested it to recognize patterns of similar formulations which were not included in the training.[275] Later, the same group[235] expanded their ANN application in combination with pharmacokinetic simulations to design controlled-release formulations with predictable *in vitro* and *in vivo* behaviour. They used formulation variables like moisture, particle size and tablet hardness as an ANN input and the dissolution profile as an output, thus the ANN was constructed by selecting the optimal number of hidden layers and nodes (parts of the ANN structure) (Figure 1.4) and it was used for predictions based on two desired target

in vitro dissolution profiles and two desired bioavailability profiles. The authors have shown the potential of using ANN, along with pharmacokinetic simulations, to support the development of complex formulations. Furthermore, they have pointed out a major advantage of the ANN model in that it "*can generalize the relationship between independent and dependant variables without a specific mathematical function*".[235] Peh *et al.*[190] investigated a different approach to train their multi-layered perceptron (type of AI model). He used the entire dissolution profile as a time-series curve. The model estimated the profile by taking time point by time point. Thus, each time point was used as a separate feature which affects further predictions.[190]

In this current work, another type of NN (CNN) was used to describe the dissolution processes in the USP 4 FTA. Images were used as an input and the results from the model were compared to the dissolution profile. It was found that the dissolution testing of suspensions could be divided into stages – beginning, early and late stage based on the suspension appearance in the image. Furthermore, it was found that background interference could result in falsely classified images which suggest presence of drug particles/formulation in the test cell after the dissolution process was completed.

7.3.2. Application of ANNs for prediction of release profiles and development of solid oral dosage forms

After the successful application of ANNs by Hussain *et al.*[276], Ebube *et al.*[275] and Chen *et al.*[235] in the late 90s, the beginning of the 21st century was marked by even more groups willing to apply the new technology to their research. ANNs have been successfully applied to various pharmaceutical areas such as modelling of *in vitro* release from immediate-release tablets[236], sustained-release tablets[163], controlled-release pellets[190] and granules[277], and to the development of solid dispersions[278]. Authors agree that ANNs are very useful when the data is nonlinear[163], [279] or incomplete[276]. ANNs have an advantage over conventional statistical methods[163] as they are capable of extracting and combining information,

recognizing patterns, making associations, and analysing and predicting output responses.[163], [236] Basheer *et al.*[280] reported that ANNs show robustness, learning ability, fault and failure tolerance, ability to generalize data and to handle vague and unclear information.

Examples from the work of two groups reported over the last two decades are presented here. Ibrić *et al.*[279] developed and applied a generalized regression NN, to assist in development of extended-release dosage forms. In 2012, they published an extensive review regarding ANNs and their application in optimization of modified-release dosage forms.[165] In their work, they divided the NNs into static and dynamic and pointed out the flexibility of the dynamic systems as their major advantage, along with the connectivity of the inputs which are not independent, but interact and influence each other.[281] Later, the same group focused on novel dosage forms such as solid dispersions and 3D printed tablets where ANNs have been applied to predict the drug release profiles.[205], [218], [278] Nagy *et al.*[172], [173], [282] focused on the development of PAT imaging technologies for real time monitoring in combination with AI models for continuous manufacturing. They have reported that their ANN model assisted the prediction of the *in vitro* dissolution of extended-release tablets using NIR and Raman spectroscopic data and could increase the sampling frequency during dissolution testing which would provide an opportunity for real time process monitoring and control.[173] As ANNs are considered the simplest NNs as discussed earlier in the introduction of this work (Chapter 1) due to their "feed-forward" nature, more recent studies report the use of CNNs as they consider the spatial information carried by images.[283], [284] Hence, the prediction of the dissolution profile could be based on the formulation composition gathered through chemical imaging, *e.g.*, Raman imaging.[155], [283]

7.3.3. CNNs – the future of imaging technologies

According to some authors, a single software or modelling algorithm, *i.e.*, NN model or ML algorithm can solve multiple problems.[165], [205] In this work, the transferring

of a CNN model initially created as a quality control tool to detect intact tablet surface to event detection during dissolution and precipitation in the USP 4 FTA was investigated. The process of model modification is explained in Chapter 4. Initially, the model was created to serve a specific reason, however, the possibility to repurpose an existing model would be time- and cost-efficient. Furthermore, the development of a new NN could require a specific knowledge in engineering and computer science, thus not many pharmaceutical scientists would have the necessary programming skill-set.

Galata *et al.*[156] used CNN to predict the dissolution profile of solid oral dosage forms based on the particle size of HPMC in the formulation. They used two spectroscopic methods (Raman and NIR) for their predictions. However, images of the dissolution process were not taken. In this current project, two methods using CNN were presented where images were acquired during the dissolution of ibuprofen powder and precipitation of particles (%FwA) (Chapter 4), and dissolution of oral suspensions (%FwA and %avgATS) (Chapter 5). The sequence of images could be used directly to give an insight into the process, or they can be used to train the model to automatically detect changes during the test. The %FwA approach is a quantitative binary method which gives a percentage of frames per time point classified as containing particles. The processing time is short (depending on the processing power),does not require sampling or insertion of probes, thus it does not interrupt the dissolution process and the hydrodynamics in the test cell, which makes it suitable to be used as a PAT real time monitoring tool[95]. There is potential for this method to be used for qualitative measurements in cases where the percentage of frames without anomalies continuously increases/decreases over time. However, the sensitivity of the method is insufficient, and the system could be confused by disturbances of the background, *e.g.*, air bubbles. In the cases where the dissolution process of suspensions was investigated, the method successfully defined the end of the dissolution process when drug and excipients were fully dissolved. It was not informative enough to detect other changes occurring in the test cell (viscous fingering, channels or matrix swelling). On the other hand, the %avgATS approach was more informative regarding changes during dissolution of the suspension, however, the method was not automated to produce the post-processing results straight away.

The CNN calculated the ATS values for each frame, then further manual analysis was needed to calculate the final %avgATS based on the images taken over the time of the whole dissolution test.

7.4. Conclusions

This section presents a list of key findings established during the conduction of this work:

1) The SGI was particularly useful to capture particle dispersal in the presence of small concentrations of surfactant. It provided a good estimation of the particle size during dissolution. Suggestions regarding particle shape could be made based on the calculated by the SGI aspect ratio. The particle detection rate and time of the detections could be used to predict the dissolution rate. For example, a high number of early detections would correspond to a generally fast dissolution, and prolonged particle detection would correspond to a slower dissolution. SGI successfully captured differences between sieved and un-sieved fractions of ibuprofen powder, crystal habits and agglomeration tendencies. The lower detection rate of needle-shaped crystals (Ibu-nd), which also showed slower dissolution rate, may reflect greater agglomeration tendency related to the crystal habit when compared to the plate-shaped crystals (Ibu-pl). Differences in the structure of the agglomerates were captured by the SGI. Needle-shaped crystals tended to connect at the tips and to form larger agglomerates, while the agglomerations formed from plate-like crystals were with undefined form and smaller size. The Ibu-pl agglomerations disappeared more quickly than the agglomerations formed from the Ibu-nd crystals.

2) Phenomena observed during dissolution such as agglomerates, found in all tests where ibuprofen powder was used, established the need for an automated online method for agglomeration identification (AIM) to be developed. The AIM was able to accurately indicate the presence of agglomerates during dissolution, considering the challenges related to presence of very large or small number of particles, choice of parameters to describe agglomerates and suitable criteria cut-off parameters. Several

parameters such as signal numbers, detection patterns and overall particle detections should be considered during AIM development and application. This method could be further applied to image selection for CNN training.

3) Dissolution and precipitation processes were examined in two dissolution apparatuses by using alternative imaging systems (SGI and Mini-cell LED Inflow Canty™ camera) and specific features for each process were determined. Due to the slow mixing of ibuprofen solution and pH decreasing (HCl) medium in the USP 4 flow-through system, both early stages (plume formation) and late stage (particle formation) of precipitation were observed. The camera resolution was not sufficient to detect very small precipitates, thus due to the pulsing flow, they looked like plume in the test cell. For instance, in the paddle apparatus a plume was not observed as equal volumes of the drug solution and HCl were instantaneous mixed. However, the Mini-cell LED Inflow Canty™ camera resolution was better compared to the SGI camera, thus observation of the particle formation process, from a grain to fully developed crystals, was possible in the paddle apparatus. On the other hand, the Mini-cell LED Inflow Canty™ camera captured very few particles during dissolution testing in the paddle apparatus. Limitations such as lens distance and drug mass need to be considered. This system has the potential to be useful during *in vitro* dissolution of high dose formulations due to presence of more particles (API and excipients) and during *in vitro* investigation of drug precipitation, *e.g.*, from supersaturated solution.

4) Images from the dissolution and precipitation process in the USP 4 FTA were used to develop a highly accurate CNN model for anomaly classification. The model was found descriptive enough to suggest beginning, middle and final stages of a particulate dissolution process and to identify the early and late stages of precipitation process (plume and particle formation). This type of AI model was developed for the first time to serve the purpose of an *in vitro* dissolution supporting tool. As a proof of concept, the current work

demonstrates potential for deep machine learning image analysis to be applied to kinetics of other pharmaceutical processes.

5) The application of this model was extended to oral liquid formulations (suspensions). There is no evidence in the literature of the imaging or AI image analysis of oral suspensions that has been done before. The image analysis of the suspension during dissolution gave important visual information regarding the formulation stability – no sedimentation of particles was observed; hydrodynamic phenomena such as viscous fingering and channel formation through the formulation and excipients swelling were observed. All these observations were used to develop a qualitative CNN model able to describe the dissolution process and to indicate specific features for the tested formulations which can be used as quality markers, *e.g.*, a specific ATS trend (smooth for N100/200 and stepwise for B100/200):

    a. The binary %FwA approach provided qualitative information about the presence of formulation in the cell even though the method was influenced by appearance of external factors like air bubbles.

    b. The %avgATS approach was less sensitive to the effect of the air bubbles and it was able to provide quantitative and qualitative information comparable with the dissolution profiles. It successfully defined three stages of the dissolution process – 1) formulation dispersal and channel formation; 2) enlargement of the channels and dissolution of the formulation; and 3) full dissolution of the formulation when no particles are present in the test cell.

This final work involved a more complex situation of sample dispersal and mixing of fluids of different viscosities. There is a scope to use both presented CNN image analyses (%FwA and %avgATS) to quantitatively characterise the impact of critical attributes such as medium composition on suspension formulations dispersal and dissolution. Furthermore, image analysis could be used to explore other formulations' dissolution behaviour, the effect of more viscous media and to support formulation

development and quality control. In conclusion, imaging and image analysis showed a great potential to be used in many areas of pharmaceutical development and research. A combination of imaging with AI models opens even more possibilities for further image investigation. Object recognition and the ability to recognize patterns without supervision could speed-up processes and decision-making. ML and DL hold many possibilities for development of customised software for multiple purposes. Although NNs have been investigated for several decades, they are still referred as a “black box” technology[282], [284] In this current work, we opened the “black box” to better understand the processes occurring inside the NN, hence the %avgATS method was developed. This work suggests that there remain potential unrealised opportunities from AI.

7.5. Future work

During the conduction of this body of work, areas for improvement and further investigation were identified. Some of these improvements could be:

7.5.1. SGI and image analysis

- Originally the SGI set-up was connected to a single cell USP 4 FTA, which provided valuable information regarding the dissolution process. However, for replicability purpose each dissolution test had to be repeated in another dissolution apparatus which allows dissolution testing done in triplicate. During the course of this project, the SGI set-up was successfully transferred to the USP 4 FTA CE7, thus imaging (n = 1) and dissolution (n = 3) could be conducted together. A custom-made water jacket for one of the test cells and a customised cell holder were

produced by the Department of Mechanical, Manufacturing & Biomedical Engineering, Trinity College Dublin.

- Although currently replicates of the dissolution data can be collected, imaging remains without replicates. Collecting multiple frames from a single video (150 frames at 10 frames per second) provides replicates of a single time point, however, variability between test cells could not be captured. Currently multiple repeats of a single dissolution test would be needed to gather this information. A possible improvement to be considered is connection of more cameras to each of the test cell. A similar approach was used by Johansson *et al.*[233] where probes were inserted in each dissolution vessel. A challenge that may arise related to multiple imaging sources could be how to combine and compare the results together.

- To improve the SGI detection power and lower the particle detectable size, a micro camera like the one used in the paddle apparatus or a lens with higher resolution/magnification could help. The refractive indices of very small particles (< 10 µm), the medium used and the cell walls should be considered. Changing the light source to a laser instead of LED light could be beneficial to better define particles.

- Currently, particle shape could be defined after manual video observation or suggested by some parameters such as the aspect ratio and solidity (circularity of the detected particle). Addition of a second camera under a certain angle (*e.g.*, 90 degrees) could provide 3D spatial information to support the shape identification.

- From a validation perspective, to exploit this technique as a PAT quality control[95] tool for real time monitoring or in advanced process control[285] tool, limitations such as repeatability, effect of external interferences (air bubbles) and accurate sizing need to be addressed.[286] Currently, an internal calibration standard with known size is used for calibration of the system before each test, thus a

specified distance of the imaging window is converted from pixels to µm, then detected particles are sized. However, to validate the sizing ability of the SGI, an experiment with insoluble particles of known size could be performed. A limitation for accurate measurement could be the depth of focus and the sharpness of the acquired image as particles appear blurred, smaller, or larger depending on their position in the cell.

7.5.2. AI analysis

According to a current FDA consultation document regarding future evaluation and validation of AI/ML concepts[3], a clear model specification and documentation of criteria for development and assessment of models is needed. Model risk factors – model influence on the decision making and the potential consequences of a wrong decision need to be evaluated. It is important to understand and monitor model performance to ensure it is reliable, relevant, and consistent over time. From a regulatory perspective, an AI model could not be referred as a "black box" technology[282], [284] and the biases related to the underlying data which shapes the decisions made by the AI model have to be understand and monitored. To date, there are limited industry standards and FDA guidance regarding development and validation of models and their potential impact on product quality.[3], [285]

- The AIM and CNN AI model presented in this present work were developed and validated based on comparison of the results with manually created reference data set (AIM) or visual confirmation. Dissolution profiles were used as a well characterised analytical procedure to compare the SGI and CNN model ability to describe a dissolution process. However, all models presented here are more proof-of-concept rather than fully developed tools for routine application. Therefore, further development and validation of the models is needed depending on how quantitative data is to be deployed.[286]

- Further improvement of the CNN approaches (%FwA and %avgATS) could be minimizing the external influence, *e.g.*, from air bubbles on model accuracy (mostly applicable for the %FwA model).

- Implementation of a built-in equation with flexible values able to calculate %avgATS based on current values at every sampling point in real time would increase the applicability of this model into industrial situations, *e.g.*, advanced process control or process monitoring and fault detection during continuous manufacturing.[285] Them obtained profile would be a dynamic function calculated based on the current situation in the test cell. However, building such function would require specific programming knowledge, *i.e.*, coding knowledge. Moreover, the application and interpretation of such feature would require solid knowledge of what the NN is doing or how this feature is being employed. At the current stage of this project, %FwA method could be used as a real time monitoring tool, while %avgATS could give additional qualitative information after further processing the data.

- Imaging and AI analysis of oral suspensions showed the potential of this technology to be used for characterisation of formulations and to support *in vitro* dissolution testing. There is scope to apply these methods to other formulations such as tablets, gels, solutions, patches or injectables. Specific characteristics related to different formulations could be captured and used by the AI model for classification and characterization. Re-training and application of the same CNN to different formulations or drug molecules would contribute to better understanding of the NN's learning processes, model validation and how one model could be transferred to different situations.[3], [286]

- The prediction ability of the AI model could be further explored by testing suspensions with different drug/excipients ratios, *i.e.*, different product strengths or suspensions with similar excipients content and different drug, *e.g.* paracetamol-containing paediatric oral suspensions. Product performance could be controlled by "smart monitoring"[285] if a specific

dissolution pattern is known for a certain product (*e.g.*, stepwise for B100/200). However, further confirmation of the observed patterns is needed.

Taking into consideration all limitations of the methods presented in this work, it is undeniable that there is potential to exploit these methods to gain extra insight. By using imaging and image analysis, real time particle monitoring and characterization during dissolution in standard apparatuses was possible. Information regarding events occurring in the test cell such as drug precipitation and agglomeration could be gathered and further exploited, *e.g.*, in a quality control set-up. Application of AI model could be used for a qualitative and quantitative analysis of dissolution processes. In the future, application of such methods as they are, or with some further development could become an indispensable part of industrial processes such as continuous manufacturing and quality control.

References

[1] D. M. D'Arcy and T. Persoons, "Mechanistic modelling and mechanistic monitoring: Simulation and shadowgraph imaging of particulate dissolution in the flow-through apparatus," *J. Pharm. Sci.*, vol. 100, no. 3, pp. 1102–1115, 2011, doi: 10.1002/jps.22337.

[2] D. M. D'Arcy, B. Liu, T. Persoons, and O. I. Corrigan, "Hydrodynamic complexity induced by the pulsing flow field in USP dissolution apparatus 4," *Dissolution Technol.*, vol. 18, no. 4, pp. 6–13, 2011, doi: 10.14227/DT180411P6.

[3] U.S. Food and Drug Administration (FDA), "Using artificial intelligence and machine learning in the development of drug and biological products," (Discussion paper), pp. 1–33, 2022. [Online]. Available: https://www.fda.gov/media/167973/download

[4] N. Fotaki *et al.*, "In–vitro product performance testing of oral drug products – views of the USP expert panel," (Stimuli article), pp. 1–11, 2024. doi: https://doi.org/10.31003/USPNF.

[5] M. Siewert, J. Dressman, C. K. Brown, and V. P. Shah, "FIP/AAPS Guidelines to dissolution/*in vitro* release testing of novel/special dosage forms," vol. 4, no. 1, pp. 1–10, 2003, doi: 10.1208/pt040107.

[6] A. Nokhodchi and K. Asare-Addo, "Drug release from matrix tablets: Physiological parameters and the effect of food," *Expert Opin. Drug Deliv.*, vol. 11, no. 9, pp. 1401–1418, 2014, doi: 10.1517/17425247.2014.924498.

[7] European Medicines Agency (EMA), Committee for medicinal products for human use (CHMP), "The new EMEA guideline on the investigation of bioequivalence," (Guideline), pp. 76–80, 2009. [Online]. Available: https://www.ema.europa.eu/en/documents/scientific-guideline/guideline-investigation-bioequivalence-rev1_en.pdf

[8] United States Pharmacopeia (USP), "The dissolution procedure: development

and validation (1092)," (Monograph), pp. 1–23, 2020. [Online]. Available: https://online.uspnf.com/uspnf/document/1_GUID-CE0902BA-77AC-422D-8BF0-A221B5DE6012_5_en-US

[9] European Medicines Agency (EMA), "Reflection paper on the dissolution specification for generic solid oral immediate release products with systemic action," (Reflection paper), pp. 1–10, 2017. [Online]. Available: https://www.ema.europa.eu/en/documents/scientific-guideline/reflection-paper-dissolution-specification-generic-solid-oral-immediate-release-products-systemic-action-first-version_en.pdf

[10] Y. Wang, R. D. Snee, G. Keyvan, and F. J. Muzzio, "Statistical comparison of dissolution profiles," *Drug Dev. Ind. Pharm.*, vol. 42, no. 5, pp. 796–807, 2016, doi: 10.3109/03639045.2015.1078349.

[11] O. Anand, L. X. Yu, D. P. Conner, and B. M. Davit, "Dissolution testing for generic drugs: An FDA perspective," *AAPS J.*, vol. 13, no. 3, pp. 328–335, 2011, doi: 10.1208/s12248-011-9272-y.

[12] X. Zhang *et al.*, "Mechanistic oral absorption modeling and simulation for formulation development and bioequivalence evaluation: Report of an FDA public workshop," *CPT Pharmacometrics Syst. Pharmacol.*, vol. 6, no. 8, pp. 492–495, 2017, doi: 10.1002/psp4.12204.

[13] U.S. Department of Health and Human Services. Food and Drug Administration (FDA), "Dissolution testing and acceptance criteria for immediate-release solid oral dosage form drug products containing high solubility drug substances. Guidance for industry," (Guideline), vol. August, pp. 1–8, 2018. [Online]. Available: http://www.fda.gov/Drugs/GuidanceComplianceRegulatoryInformation/Guidances/default.htm%0Afile:///C:/Users/ASUS/Desktop/Rujukan PhD/Drug Release/1074043 FNL_clean.pdf

[14] E. Scheubel, "Predictive *in vitro* dissolution tools: Application during formulation development," PhD Thesis, Faculty of Pharmacy, Univ. Clermont-Ferrand I, France, 2010. [Online]. Available: https://theses.hal.science/tel-00719613

[15] S. Suarez-Sharp *et al.*, "Applications of clinically relevant dissolution testing: Workshop summary report," *AAPS J.*, vol. 20, no. 6, pp. 1–14, 2018, doi: 10.1208/s12248-018-0252-3.

[16] Y. Tsumea, D. M. Mudiea, P. Langguthb, G. E. Amidona, and G. L. Amidona, "The biopharmaceutics classification system: Subclasses for *in vivo* predictive dissolution (IPD) methodology and IVIVC," *Eur. J. Pharm. Sci.*, vol. June, no. 57, pp. 152–163, 2014, doi: 10.1016/j.ejps.2014.01.009.

[17] S. Klein, "The use of biorelevant dissolution media to forecast the *in vivo* performance of a drug," *AAPS J.*, vol. 12, no. 3, pp. 397–406, 2010, doi: 10.1208/s12248-010-9203-3.

[18] E. Jantratid, N. Janssen, C. Reppas, and J. B. Dressman, "Dissolution media simulating conditions in the proximal human gastrointestinal tract: An update," *Pharm. Res.*, vol. 25, no. 7, pp. 1663–1676, 2008, doi: 10.1007/s11095-008-9569-4.

[19] E. Galia, E. Nicolaides, and J. B. Dressman, "Evaluation of various dissolution media for predicting *in vivo* performance of class I and II drugs," *Pharm. Res.*, vol. 15, no. 5, pp. 698–705, 1998, doi: 10.1023/a:1011910801212.

[20] T. Zoeller and S. Klein, "Simplified biorelevant media for poorly soluble drugs," *Dissolution Technol.*, vol. 14, no. 4, pp. 8–13, 2007, doi: dx.doi.org/10.14227/DT140407P8.

[21] C. H. Gu, R. B. Gandhi, L. K. Tay, S. Zhou, and K. Raghavan, "Importance of using physiologically relevant volume of dissolution medium to correlate the oral exposure of formulations of BMS-480188 mesylate," *Int. J. Pharm.*, vol. 269, no. 1, pp. 195–202, 2004, doi: 10.1016/j.ijpharm.2003.09.005.

[22] A. Avdeef, "Solubility of sparingly-soluble ionizable drugs," *Adv. Drug Deliv. Rev.*, vol. 59, no. 7, pp. 568–590, 2007, doi: 10.1016/j.addr.2007.05.008.

[23] S. Emmanuel, L. Marc, B. Eric, and C. Jean-Michel, "Small volume dissolution testing as a powerful method during pharmaceutical development," *Pharmaceutics*, vol. 2, no. 4, pp. 351–363, 2010, doi:

10.3390/pharmaceutics2040351.

[24] Y. Sun and J. Østergaard, “Application of UV imaging in formulation development,” *Pharm. Res.*, vol. 34, no. 5, pp. 929–940, 2017, doi: 10.1007/s11095-016-2047-5.

[25] J. Siepmann and F. Siepmann, “Mathematical modeling of drug dissolution,” *Int. J. Pharm.*, vol. 453, no. 1, pp. 12–24, 2013, doi: 10.1016/j.ijpharm.2013.04.044.

[26] A. A. Noyes and W. R. Whitney, “The rate of solution of solid substances in their own solutions,” *J. Am. Chem. Soc.*, vol. 19, no. 12, pp. 930–934, 1897. [Online]. Available: https://pubs.acs.org/doi/abs/10.1021/ja02086a003

[27] D. Kapoor, R. Maheshwari, K. Verma, S. Sharma, A. Pethe, and R. K. Tekade, *Drug delivery systems. Chapter 1: Fundamentals of diffusion and dissolution: dissolution testing of pharmaceuticals*. Elsevier Inc., 2019. doi: 10.1016/B978-0-12-814487-9.00001-6.

[28] T. Higuchi, “Mechanism of sustained-action medication. Theoretical analysis of rate of release of solid drugs dispersed in solid matrices,” *J. Pharm. Sci.*, vol. 52, no. 12, pp. 1145–1149, 1963, doi: 10.1002/jps.2600521210.

[29] P. I. Lee, “Modeling of drug release from matrix systems involving moving boundaries: Approximate analytical solutions,” *Int. J. Pharm.*, vol. 418, no. 1, pp. 18–27, 2011, doi: 10.1016/j.ijpharm.2011.01.019.

[30] B. Narasimhan, “Mathematical models describing polymer dissolution: Consequences for drug delivery,” *Adv. Drug Deliv. Rev.*, vol. 48, no. 2–3, pp. 195–210, 2001, doi: 10.1016/S0169-409X(01)00117-X.

[31] European Medicines Agency (EMA), Committee for medicinal products for human use (CHMP), “ICH guideline Q8 (R2) on pharmaceutical development, Step 5: Note for guidance on pharmaceutical development,” (Guideline), vol. 8, no. June, pp.1–24, 2017. [Online]. Available: https://www.ema.europa.eu/en/ich-q8-r2-pharmaceutical-development-scientific-guideline

[32] G. L. Amidon, H. Lennernäs, V. P. Shah, and J. R. Crison, “A theoretical basis for a biopharmaceutic drug classification: The correlation of *in vitro* drug product dissolution and *in vivo* bioavailability,” *Pharm. Res.*, vol. 12, no. 3, pp. 413–420, 1995, doi: 10.1023/A:1016212804288.

[33] U.S. Department of Health and Human Services. Food and Drug Administration (FDA), “Guidance for industry - Dissolution testing of immediate release solid oral dosage forms,” (Guideline), vol. August, pp. 1–17, 1997. [Online]. Available: https://www.fda.gov/media/70936/download.

[34] A. Abend, T. Heimbach, M. Cohen, F. Kesisoglou, X. Pepin, and S. Suarez-Sharp, “Dissolution and translational modeling strategies enabling patient-centric drug product development: The M-CERSI workshop summary report,” *AAPS J.*, vol. 20, no. 60, pp. 1–8, 2018, doi: 10.1208/s12248-018-0213-x.

[35] N. Rasenack and B. W. Müller, “Properties of ibuprofen crystallized under various conditions: A comparative study,” *Drug Dev. Ind. Pharm.*, vol. 28, no. 9, pp. 1077–1089, 2002, doi: 10.1081/DDC-120014575.

[36] J. C. Rivera-Leyva, M. García-Flores, A. Valladares-Méndez, L. M. Orozco-Castellanos, and M. Martínez-Alfaro, “Comparative studies on the dissolution profiles of oral ibuprofen suspension and commercial tablets using biopharmaceutical classification system criteria,” *Indian J. Pharm. Sci.*, vol. 74, no. 4, pp. 312–318, 2012, doi: 10.4103/0250-474X.107062.

[37] A. Ward *et al.*, “Variable-focus microscopy and UV surface dissolution imaging as complementary techniques in intrinsic dissolution rate determination,” *Int. J. Pharm.*, vol. 530, no. 1–2, pp. 139–144, 2017, doi: 10.1016/j.ijpharm.2017.07.053.

[38] K. Asare-Addo *et al.*, “Direct imaging of the dissolution of salt forms of a carboxylic acid drug,” *Int. J. Pharm.*, vol. 551, no. 1–2, pp. 290–299, 2018, doi: 10.1016/j.ijpharm.2018.09.048.

[39] A. M. Healy and O. I. Corrigan, “Predicting the dissolution rate of ibuprofen-acidic excipient compressed mixtures in reactive media,” *Int. J. Pharm.*, vol. 84,

no. 2, pp. 167–173, 1992, doi: 10.1016/0378-5173(92)90057-9.

[40] A. V. Bhosale, G. P. Agrawal, and P. Mishra, “Preparation and evaluation of directly compressible forms of mutual prodrugs of ibuprofen,” *Indian J. Pharm. Sci.*, vol. 68, no. 4, pp. 425–431, 2006, doi: 10.4103/0250-474x.27812.

[41] S. Islam and S. I. Pathan, “Improving micromeritic properties of ibuprofen: An agglomeration approach,” *Bangladesh Pharm. J.*, vol. 20, no. 1, pp. 90–98, 2017, doi: 10.3329/bpj.v20i1.32098.

[42] R. Cristofoletti and J. B. Dressman, “Dissolution methods to increasing discriminatory power of *in vitro* dissolution testing for ibuprofen free acid and its salts,” *J. Pharm. Sci.*, vol. 106, no. 1, pp. 92–99, 2017, doi: 10.1016/j.xphs.2016.06.001.

[43] V. Gray, G. Kelly, M. Xia, C. Butler, S. Thomas, and S. Mayock, “The science of USP 1 and 2 dissolution: Present challenges and future relevance,” *Pharm. Res.*, vol. 26, no. 6, pp. 1289–1302, 2009, doi: 10.1007/s11095-008-9822-x.

[44] L. X. Yu *et al.*, “Understanding pharmaceutical quality by design,” *AAPS J.*, vol. 16, no. 4, pp. 771–783, 2014, doi: 10.1208/s12248-014-9598-3.

[45] V. A. Gray, “Power of the dissolution test in distinguishing a change in dosage form critical quality attributes,” *AAPS PharmSciTech*, vol. 19, no. 8, pp. 3328–3332, 2018, doi: 10.1208/s12249-018-1197-7.

[46] U.S. Department of Health and Human Services. Food and Drug Administration (FDA), “Waiver of *in vivo* bioavailability and bioequivalence studies for immediate-release solid oral dosage forms based on a biopharmaceutics classification system. Guidance for industry.,” (Guideline), no. December, pp. 27–35, 2017. [Online].
Available: https://digirepo.nlm.nih.gov/master/borndig/101720038/UCM070246.pdf.

[47] J. M. Butler and J. B. Dressman, “The developability classification system: Application of biopharmaceutics concepts to formulation development,” *J. Pharm. Sci.*, vol. 99, no. 12, pp. 4940–4954, 2010, doi: 10.1002/jps.22217.

[48] H. Potthast *et al.*, “Biowaiver monographs for immediate release solid oral dosage forms: Ibuprofen,” *J. Pharm. Sci.*, vol. 94, no. 10, pp. 2121–2131, 2005, doi: 10.1002/jps.20444.

[49] J. B. Dressman and C. Reppas, “*In vitro-in vivo* correlations for lipophilic, poorly water-soluble drugs,” *Eur. J. Pharm. Sci.*, vol. 11, no. Suppl. 2, pp. 73–80, 2000, doi: 10.1016/S0928-0987(00)00181-0.

[50] European Medicines Agency (EMA), “European Pharmacopoeia 11.0. Dissolution test for solid dosage forms (Ph. Eur. 2.9.3),” (Monograph), pp. 228–230, 2023. [Online]. Available: http://www.uspbpep.com/ep60/2.9

[51] United States Pharmacopeia (USP), “Dissolution (711),” (Monograph), pp. 1–13, 2023. [Online]. Available: http://ftp.uspbpep.com/v29240/usp29nf

[52] United States Pharmacopeia (USP). “Assessment of solid oral drug product performance and interchangeability, bioavailability, bioequivalence, and dissolution (1090),” (Monograph), pp. 1–10, 2019. [Online]. Available: https://doi.usp.org/USPNF/USPNF

[53] E. Å. Borbás, A. Balogh, K. Bocz, J. Müller, É. Kiserdei, and T. Vigh, “*In vitro* dissolution – permeation evaluation of an electrospun cyclodextrin-based formulation of aripiprazole using mFluxTM,” *Int. J. Pharm.*, vol. 491, no. 1, pp. 180–189, 2015, doi: 10.1016/j.ijpharm.2015.06.019.

[54] J. Štukelj, M. Agopov, J. Yliruusi, C. J. Strachan, and S. Svanbäck, “Image-based dissolution analysis for tracking the surface stability of amorphous powders,” *ADMET DMPK*, vol. 8, no. 4, pp. 401–409, 2020, doi: 10.5599/admet.839.

[55] V. Todaro, T. Persoons, G. Grove, A. M. Healy, and D. M. D’Arcy, “Characterization and simulation of hydrodynamics in the paddle, basket and flow-through dissolution testing apparatuses. A review,” *Dissolution Technol.*, vol. 24, no. 3, pp. 24–36, 2017, doi: 10.14227/DT240317P24.

[56] S. T. Buckley, K. J. Frank, G. Fricker, and M. Brandl, “Biopharmaceutical classification of poorly soluble drugs with respect to ‘enabling formulations,’” *Eur. J. Pharm. Sci.*, vol. 50, no. 1, pp. 8–16, 2013, doi:

10.1016/j.ejps.2013.04.002.

[57] S. Heisel, M. Rolfes, and K. Wohlgemuth, “Discrimination between single crystals and agglomerates during the crystallization process,” *Chem. Eng. Technol.*, vol. 41, no. 6, pp. 1218–1225, 2018, doi: 10.1002/ceat.201700651.

[58] A. Schittny, J. Huwyler, and M. Puchkov, “Mechanisms of increased bioavailability through amorphous solid dispersions: A review,” *Drug Deliv.*, vol. 27, no. 1, pp. 110–127, 2020, doi: 10.1080/10717544.2019.1704940.

[59] Y. Shono, E. Jantratid, and J. B. Dressman, “Precipitation in the small intestine may play a more important role in the *in vivo* performance of poorly soluble weak bases in the fasted state: Case example nelfinavir,” *Eur. J. Pharm. Biopharm.*, vol. 79, no. 2, pp. 349–356, 2011, doi: 10.1016/j.ejpb.2011.04.005.

[60] E. S. Kostewicz *et al.*, “*In vitro* models for the prediction of *in vivo* performance of oral dosage forms,” *Eur. J. Pharm. Sci.*, vol. 57, no. 1, pp. 342–366, 2014, doi: 10.1016/j.ejps.2013.08.024.

[61] M. Hofmann *et al.*, “*In vitro* prediction of *in vivo* absorption of ibuprofen from suspensions through rational choice of dissolution conditions,” *Eur. J. Pharm. Biopharm.*, vol. 149, no. February, pp. 229–237, 2020, doi: 10.1016/j.ejpb.2020.02.009.

[62] G. Nichols *et al.*, “A review of the terms agglomerate and aggregate with a recommendation for nomenclature used in powder and particle characterization,” *J. Pharm. Sci.*, vol. 91, no. 10, pp. 2103–2109, 2002, doi: 10.1002/jps.10191.

[63] United States Pharmacopeia (USP), “Optical microscopy (776),” (Monograph), pp. 2–5, 2023. [Online]. Available: http://www.uspbpep.com/usp29/v29240/usp29nf

[64] H. Shibata, A. Harazono, M. Kiyoshi, and A. Ishii-Watabe, “Quantitative evaluation of insoluble particulate matters in therapeutic protein injections using light obscuration and flow imaging methods,” *J. Pharm. Sci.*, vol. 111, no. 3, pp. 648–654, 2022, doi: 10.1016/j.xphs.2021.09.047.

[65] T. Wenzel, C. Stillhart, P. Kleinebudde, and A. Szepes, “Influence of drug load on dissolution behavior of tablets containing a poorly water-soluble drug: Estimation of the percolation threshold,” *Drug Dev. Ind. Pharm.*, vol. 43, no. 8, pp. 1265–1275, 2017, doi: 10.1080/03639045.2017.1313856.

[66] S. M. Wong, I. W. Kellaway, and S. Murdan, “Enhancement of the dissolution rate and oral absorption of a poorly water soluble drug by formation of surfactant-containing microparticles,” *Int. J. Pharm.*, vol. 317, no. 1, pp. 61–68, 2006, doi: 10.1016/j.ijpharm.2006.03.001.

[67] T. Waghule *et al.*, “Voriconazole loaded nanostructured lipid carriers based topical delivery system: QbD based designing, characterization, in-vitro and ex-vivo evaluation,” *J. Drug Deliv. Sci. Technol.*, vol. 52, no. August, pp. 303–315, 2019, doi: 10.1016/j.jddst.2019.04.026.

[68] A. Elgart, I. Cherniakov, Y. Aldouby, A. J. Domb, and A. Hoffman, “Improved oral bioavailability of BCS class 2 compounds by self nano-emulsifying drug delivery systems (SNEDDS): The underlying mechanisms for amiodarone and talinolol,” *Pharm. Res.*, vol. 30, no. 12, pp. 3029–3044, 2013, doi: 10.1007/s11095-013-1063-y.

[69] I. Sathisaran and S. V. Dalvi, “Engineering cocrystals of poorly water-soluble drugs to enhance dissolution in aqueous medium,” *Pharmaceutics*, vol. 10, no. 108, pp. 1–74, 2018, doi: 10.3390/pharmaceutics10030108.

[70] S. Agharkar, S. Lindenbaum, and T. Higuchi, “Enhancement of solubility of drug salts by hydrophilic counterions: Properties of organic salts of an antimalarial drug,” *J. Pharm. Sci.*, vol. 65, no. 5, pp. 747–749, 1976, doi: 10.1002/jps.2600650533.

[71] S. Kalepu and V. Nekkanti, “Insoluble drug delivery strategies: Review of recent advances and business prospects,” *Acta Pharm. Sin. B*, vol. 5, no. 5, pp. 442–453, 2015, doi: 10.1016/j.apsb.2015.07.003.

[72] S. V. Bhujbal *et al.*, “Pharmaceutical amorphous solid dispersion: A review of manufacturing strategies,” *Acta Pharm. Sin. B*, vol. 11, no. 8, pp. 2505–2536,

2021, doi: 10.1016/j.apsb.2021.05.014.

[73] N. Blagden, M. de Matas, P. T. Gavan, and P. York, “Crystal engineering of active pharmaceutical ingredients to improve solubility and dissolution rates,” *Adv. Drug Deliv. Rev.*, vol. 59, no. 7, pp. 617–630, 2007, doi: 10.1016/j.addr.2007.05.011.

[74] S. Potharaju, “Effect of compression force on agglomeration of micronized active pharmaceutical ingredients: Techniques to prevent API agglomeration during compression,” PhD Thesis, Health Science Center, Univ. of Tennessee, Memphis, TN, USA, 2012. [Online]. Available: http://dx.doi.org/10.21007/etd.cghs.2012.0251.

[75] United States Pharmacopeia (USP), “Pharmaceutical dosage forms (1151),” (Monograph), pp. 1–23, 2024. [Online]. Available: http://www.pharmacopeia.cn/v29240/usp29nf

[76] D. J. Phillips, S. R. Pygall, V. B. Cooper, and J. C. Mann, “Overcoming sink limitations in dissolution testing: A review of traditional methods and the potential utility of biphasic systems,” *J. Pharm. Pharmacol.*, vol. 64, no. 11, pp. 1549–1559, 2012, doi: 10.1111/j.2042-7158.2012.01523.x.

[77] M. G. Azam and S. S. Haider, “Evaluation of dissolution behavior of paracetamol suspensions,” *Dhaka Univ. J. Pharm. Sci.*, vol. 7, no. 1, pp. 53–58, 2008, doi: 10.3329/dujps.v7i1.1218.

[78] L. K. Mathur *et al.*, “Bioavailability and dissolution behavior of trisulfapyrimidine suspensions,” *J. Pharm. Sci.*, vol. 68, no. 6, pp. 699–702, 1979, doi: 10.1002/jps.2600680611.

[79] T. Soares, J. Souza, L. Rosa, and F. Marques-Marinho, “Dissolution test for oral suspension: An overview about use and importance,” *Brazilian J. Pharm. Sci.*, vol. 58, no. e19423, pp. 1–27, 2022, doi: http://dx.doi.org/10.1590/s2175-97902022e19423.

[80] United States Pharmacopeia (USP), “Ibuprofen Oral Suspension,” (Monograph), pp. 1–2, 2024. [Online].

Available: http://www.pharmacopeia.cn/v29240/usp29nf

[81] C. K. Brown *et al.*, "FIP/AAPS joint workshop report: dissolution/*in vitro* release testing of novel/special dosage forms.," *AAPS PharmSciTech*, vol. 12, no. 2, pp. 782–794, 2011, doi: 10.1208/s12249-011-9634-x.

[82] E. Kazandjievska *et al.*, "Non-compendial vs compendial analytical tests - a powerful tool for predicting *in vitro* similarity of highly viscous oral suspension," *Maced. Pharm. Bull.*, vol. 64, no. 2, pp. 61–72, 2019, doi: 10.33320/maced.pharm.bull.2018.64.02.007.

[83] L. B. Da Fonseca, M. Labastie, V. P. De Sousa, and N. M. Volpato, "Development and validation of a discriminative dissolution test for nimesulide suspensions," *AAPS PharmSciTech*, vol. 10, no. 4, pp. 1145–1152, 2009, doi: 10.1208/s12249-009-9320-4.

[84] J. Parker and V. Gray, "Highlights of the AAPS workshop on dissolution testing for the 21st century," *Dissolution Technol.*, vol. 13, no. 3, pp. 26–31, 2006. [Online]. Available: dx.doi.org/10.14227/DT130306P26

[85] O. Boscolo *et al.*, "Pharmaceutical suspensions of ursodeoxycholic acid for pediatric patients: *in vitro* and *in vivo* studies," *Pharm. Dev. Technol.*, vol. 26, no. 5, pp. 599–609, 2021, doi: 10.1080/10837450.2021.1905662.

[86] H. Lennernäs *et al.*, "*In vivo* predictive dissolution (IPD) and biopharmaceutical modeling and simulation: Future use of modern approaches and methodologies in a regulatory context," *Mol. Pharm.*, vol. 14, no. 4, pp. 1307–1314, 2017, doi: 10.1021/acs.molpharmaceut.6b00824.

[87] S. A. Qureshi, G. Caillé, R. Brien, G. Piccirilli, V. Yu, and I. J. Mcgilveray, "Application of flow-through dissolution method for the evaluation of oral formulations of nifedipine," *Drug Dev. Ind. Pharm.*, vol. 20, no. 11, pp. 1869–1882, 1994, doi: 10.3109/03639049409050214.

[88] W. Brown, "Apparatus 4 flow through cell: Some thoughts on operational characteristics," *Dissolution Technol.*, vol. 12, no. 2, pp. 28–30, 2005, doi: 10.14227/DT120205P28.

[89] M. Kakhi, “Classification of the flow regimes in the flow-through cell,” *Eur. J. Pharm. Sci.*, vol. 37, no. 5, pp. 531–544, 2009, doi: 10.1016/j.ejps.2009.04.003.

[90] G. M. Homsy, “Viscous fingering in Hele-Shaw cells,” *J. Fluid Mech.*, vol. 19, pp. 271–311, 1987. [Online]. Available: https://web.njit.edu/~kondic/capstone/2015/homsy_annual_review_87.pdf

[91] M. Mishra, M. Martin, and A. De Wit, “Differences in miscible viscous fingering of finite width slices with positive or negative log-mobility ratio,” *Phys. Rev. E*, vol. 78, no. 6, pp. 1–11, 2008, doi: 10.1103/PhysRevE.78.066306.

[92] B. Jha, L. Cueto-felgueroso, and R. Juanes, “Fluid mixing from viscous fingering,” *Phys. Rev. Lett.*, vol. 106, no. 19, pp. 1–4, 2011, doi: 10.1103/PhysRevLett.106.194502.

[93] H. A. Garekani, F. Sadeghi, A. Badiee, S. A. Mostafa, A. R. Rajabi-Siahboomi, and A. R. Rajabi-Siahboomi, “Crystal habit modifications of ibuprofen and their physicomechanical characteristics,” *Drug Dev. Ind. Pharm.*, vol. 27, no. 8, pp. 803–809, 2001, doi: 10.1081/DDC-100107243.

[94] D. Saravanan, P. Muthudoss, P. Khullar, and A. Rose Venis, “Micronization and agglomeration: Understanding the impact of API particle properties on dissolution and permeability using solid state and biopharmaceutical ‘Toolbox,’” *J. Pharm. Innov.*, vol. 16, no. 1, pp. 136–151, 2021, doi: 10.1007/s12247-019-09424-1.

[95] U.S. Department of Health and Human Services. Food and Drug Administration (FDA), “Guidance for Industry. PAT - a framework for innovative pharmaceutical development, manufacturing and quality assurance,” vol. September, pp. 1–19, 2004. [Online]. Available: https://www.fda.gov/regulatory-information/search-fda-guidance-documents/pat-framework-innovative-pharmaceutical-development-manufacturing-and-quality-assurance

[96] Z. K. Nagy, G. Fevotte, H. Kramer, and L. L. Simon, “Recent advances in the monitoring, modelling and control of crystallization systems,” *Chem. Eng. Res.*

Des., vol. 91, no. 10, pp. 1903–1922, 2013, doi: 10.1016/j.cherd.2013.07.018.

[97] L. Zhang and S. Mao, "Application of quality by design in the current drug development," *Asian J. Pharm. Sci.*, vol. 12, no. 1, pp. 1–8, 2017, doi: 10.1016/j.ajps.2016.07.006.

[98] S. G. Kazarian and A. V. Ewing, "Applications of Fourier transform infrared spectroscopic imaging to tablet dissolution and drug release," *Expert Opin. Drug Deliv.*, vol. 10, no. 9, pp. 1207–1221, 2013, doi: 10.1517/17425247.2013.801452.

[99] B. Nagy *et al.*, "In-line Raman spectroscopic monitoring and feedback control of a continuous twin-screw pharmaceutical powder blending and tableting process," *Int. J. Pharm.*, vol. 530, no. 1–2, pp. 21–29, 2017, doi: 10.1016/j.ijpharm.2017.07.041.

[100] B. Nagy, A. Farkas, E. Borbás, P. Vass, Z. K. Nagy, and G. Marosi, "Raman spectroscopy for process analytical technologies of pharmaceutical secondary manufacturing," *AAPS PharmSciTech*, vol. 20, no. 1, 2019, doi: 10.1208/s12249-018-1201-2.

[101] D. Wilson, S. Wren, and G. Reynolds, "Linking dissolution to disintegration in immediate release tablets using image analysis and a population balance modelling approach," *Pharm. Res.*, vol. 29, no. 1, pp. 198–208, 2012, doi: 10.1007/s11095-011-0535-1.

[102] D. Caccavo, S. Cascone, G. Lamberti, and A. A. Barba, "Controlled drug release from hydrogel-based matrices: Experiments and modeling," *Int. J. Pharm.*, vol. 486, no. 1–2, pp. 144–152, 2015, doi: 10.1016/j.ijpharm.2015.03.054.

[103] A. D. Rajkumar, G. K. Reynolds, D. Wilson, S. Wren, M. J. Hounslow, and A. D. Salman, "Investigating the effect of processing parameters on pharmaceutical tablet disintegration using a real-time particle imaging approach," *Eur. J. Pharm. Biopharm.*, vol. 106, no. September, pp. 88–96, 2016, doi: 10.1016/j.ejpb.2016.06.005.

[104] K. Asare-Addo *et al.*, "Effect of preparation method on the surface properties

and UV imaging of indomethacin solid dispersions," *Eur. J. Pharm. Biopharm.*, vol. 137, no. March, pp. 148–163, 2019, doi: 10.1016/j.ejpb.2019.03.002.

[105] D. Karampalis, H. Cao, J. Caragay, Y. Ding, and S. Bakalis, "Understanding dissolution phenomena of spray dried powders using a single particle approach," *Chem. Eng. Sci.*, vol. 196, no. March, pp. 25–36, 2019, doi: 10.1016/j.ces.2018.11.046.

[106] X. Z. Wang, J. Calderon De Anda, and K. J. Roberts, "Real-time measurement of the growth rates of individual crystal facets using imaging and image analysis: A feasibility study on needle-shaped crystals of L-glutamic acid," *Chem. Eng. Res. Des.*, vol. 85, no. 7, pp. 921–927, 2007, doi: 10.1205/cherd06203.

[107] S. Verma and P. J. Shlichta, "Imaging techniques for mapping solution parameters, growth rate, and surface features during the growth of crystals from solution," *Prog. Cryst. Growth Charact. Mater.*, vol. 54, no. 1–2, pp. 1–120, 2008, doi: 10.1016/j.pcrysgrow.2008.03.001.

[108] K. Tieu, A. Salt, J. Wirges, and G. N. Grove, "Regulatory considerations for the classification of video monitoring in dissolution testing," *Ageing Int.*, vol. 15, no. 6, pp. 1611–1618, 2014, doi: 10.1208/s12249-014-0191-y.

[109] B. Van Eerdenbrugh and L. S. Taylor, "Application of mid-IR spectroscopy for the characterization of pharmaceutical systems," *Int. J. Pharm.*, vol. 417, no. 1–2, pp. 3–16, 2011, doi: 10.1016/j.ijpharm.2010.12.011.

[110] N. L. Gonzalez Vidal and M. Esther Gil Alegre, "UV analytical method suitability for investigation of BCS class 2 biowaivers: Ibuprofen case," *Dissolution Technol.*, vol. 20, no. 1, pp. 44–47, 2013, doi: 10.14227/DT200113P44.

[111] P. Kulinowski, P. Dorożyński, A. Młynarczyk, and W. P. Węglarz, "Magnetic resonance imaging and image analysis for assessment of HPMC matrix tablets structural evolution in USP apparatus 4," *Pharm. Res.*, vol. 28, no. 5, pp. 1065–1073, 2011, doi: 10.1007/s11095-010-0357-6.

[112] Q. Zhang, L. Gladden, P. Avalle, and M. Mantle, "*In vitro* quantitative 1H and 19F nuclear magnetic resonance spectroscopy and imaging studies of fluvastatin™

in Lescol® XL tablets in a USP-IV dissolution cell," *J. Control. release*, vol. 156, no. 3, pp. 345–354, 2011, doi: 10.1016/j.jconrel.2011.08.039.

[113] N. M. Goudarzi, A. Samaro, C. Vervaet, and M. N. Boone, "Development of flow-through cell dissolution method for in-situ visualization of dissolution processes in solid dosage forms using X-ray µCT," *Pharmaceutics*, vol. 14, no. 2475, pp. 1–15, 2022, doi: 10.3390/pharmaceutics14112475.

[114] J. Østergaard, J. Lenke, S. S. Jensen, Y. Sun, and F. Ye, "UV imaging for *in vitro* dissolution and release studies: Initial experiences," *Dissolution Technol.*, vol. 21, no. 4, pp. 27–38, 2014, doi: 10.14227/DT210414P27.

[115] J. Østergaard, "UV imaging in pharmaceutical analysis," *J. Pharm. Biomed. Anal.*, vol. 147, no. January, pp. 140–148, 2018, doi: 10.1016/j.jpba.2017.07.055.

[116] M. Kuentz, "Analytical technologies for real-time drug dissolution and precipitation testing on a small scale," *J. Pharm. Pharmacol.*, vol. 67, no. 2, pp. 143–159, 2015, doi: 10.1111/jphp.12271.

[117] A. Ward *et al.*, "Development of a novel method utilising dissolution imaging for the measurement of swelling behaviour in hydrophilic matrices," *Int. J. Pharm. X*, vol. 1, no. November 2018, 2019, doi: 10.1016/j.ijpx.2019.100013.

[118] M. Kiyoshi *et al.*, "Collaborative study for analysis of subvisible particles using flow imaging and light obscuration: Experiences in japanese biopharmaceutical consortium," *J. Pharm. Sci.*, vol. 108, no. 2, pp. 832–841, 2019, doi: 10.1016/j.xphs.2018.08.006.

[119] N. Laitinen, O. Antikainen, J. Rantanen, and J. Yliruusi, "New perspectives for visual characterization of pharmaceutical solids," *J. Pharm. Sci.*, vol. 93, no. 1, pp. 165–176, 2004, doi: 10.1002/jps.10529.

[120] M. Legrand, J. Nogueira, A. Lecuona, and A. Hernando, "Single camera volumetric shadowgraphy system for simultaneous droplet sizing and depth location, including empirical determination of the effective optical aperture," *Exp. Therm. Fluid Sci.*, vol. 76, pp. 135–145, 2016, doi: 10.1016/j.expthermflusci.2016.03.018.

[121] A. Srivastava, K. Muralidhar, and P. K. Panigrahi, “Comparison of interferometry, schlieren and shadowgraph for visualizing convection around a KDP crystal,” *J. Cryst. Growth*, vol. 267, no. 1–2, pp. 348–361, 2004, doi: 10.1016/j.jcrysgro.2004.03.031.

[122] P. K. Panigrahi and K. Muralidhar, *Schlieren and shadowgraph methods in heat and mass transfer. Chapter 2: Laser schlieren and shadowgraph.* SpringerBriefs Therm. Eng. Appl. Sci., 2012, doi: 10.1007/978-1-4614-4535-7_2.

[123] W. Merzkirch, “Shadowgraph technique,” *Termopedia*, https://www.thermopedia.com/content/1117/, Accessed: Aug. 25, doi: 10.1615/AtoZ.s.shadowgraph_technique.

[124] G. S. Settles, *Schlieren and shadowgraph techniques.* Springer, Berlin, Heidelberg, 2001. doi: 10.1007/978-3-642-56640-0.

[125] G. Settles and F. Alvi, “Structure of swept shock wave/boundary-layer interactions using conical shadowgraphy,” *AIAA 21st Fluid dynamicss, plasma dynamics and lasers conference*. Washington, D.C., USA, 1990, doi: 10.2514/6.1990-1644.

[126] D. Wirz, M. Hofmann, H. Lorenz, H. J. Bart, A. Seidel-Morgenstern, and E. Temmel, “A novel shadowgraphic inline measurement technique for image-based crystal size distribution analysis,” *Crystals*, vol. 10, no. 9, pp. 1–26, 2020, doi: 10.3390/cryst10090740.

[127] O. F. P. Lyons, T. Persoons, and D. B. Murray, “Particle sizing and flow measurements in an atomizing mist jet nozzle: A shadowgraphy approach,” *ILASS – Europe 2010, 23rd Annual Conference on Liquid Atomization and Spray Systems*. Brno, Czech Republic, 2010. [Online]. Available: https://www.researchgate.net/publication/228821312

[128] *Particle master shadow*, LaVision GmbH, Göttingen, Germany, 2010. Accessed: Aug. 25, 2020. [Online]. Available: https://www.lavision.de/en/downloads/manuals/systems.php

[129] D. R. Serrano, T. Persoons, D. M. D’Arcy, C. Galiana, M. A. Dea-Ayuela, and A. M.

Healy, “Modelling and shadowgraph imaging of cocrystal dissolution and assessment of *in vitro* antimicrobial activity for sulfadimidine/4-aminosalicylic acid cocrystals,” *Eur. J. Pharm. Sci.*, vol. 89, no. August, pp. 125–136, 2016, doi: 10.1016/j.ejps.2016.04.030.

[130] J. Li, S. Shao, and J. Hong, “Machine learning shadowgraph for particle size and shape characterization,” *Meas. Sci. Technol.*, vol. 32, no. 1, pp. 1–10, 2020, doi: 10.1088/1361-6501/abae90.

[131] D. M. D’Arcy and T. Persoons, “Understanding the potential for dissolution simulation to explore the effects of medium viscosity on particulate dissolution,” *AAPS PharmSciTech*, vol. 20, no. 2, pp. 1–13, 2019, doi: 10.1208/s12249-018-1260-4.

[132] Z. Liu *et al.*, “Correlative image-based release prediction and 3D microstructure characterization for a long acting parenteral implant,” *Pharm. Res.*, vol. 38, no. 11, pp. 1915–1929, 2021, doi: 10.1007/s11095-021-03145-2.

[133] A. K. Rajagopalan *et al.*, “A comprehensive shape analysis pipeline for stereoscopic measurements of particulate populations in suspension,” *Powder Technol.*, vol. 321, no. November, pp. 479–493, 2017, doi: 10.1016/j.powtec.2017.08.044.

[134] C. R. Mercer, *Optical metrology for fluids, combustion and solids*. Springer New York, NY, 2003. doi: 10.1007/978-1-4757-3777-6.

[135] Y. Gao, B. Glennon, V. K. Kamaraju, G. Hou, and P. Donnellan, “Dissolution kinetics of a BCS class II active pharmaceutical ingredient,” *Org. Process Res. Dev.*, vol. 22, no. 3, pp. 328–336, 2018, doi: 10.1021/acs.oprd.7b00365.

[136] A. Tadayyon and S. Rohani, “Determination of particle size distribution by Par-Tec® 100: Modeling and experimental results,” *Part. Part. Syst. Charact.*, vol. 15, no. 3, pp. 127–135, 1998, doi: 10.1002/(SICI)1521-4117(199817)15:3<127::AID-PPSC127>3.0.CO;2-B.

[137] C. A. Coutant, M. J. Skibic, G. D. Doddridge, C. A. Kemp, and D. C. Sperry, “*In vitro* monitoring of dissolution of an immediate release tablet by focused beam

reflectance measurement," *Mol. Pharm.*, vol. 7, no. 5, pp. 1508–1515, 2010, doi: 10.1021/mp1001476.

[138] J-H. Han *et al.*, "A real-time study of disintegration and Reflectance, in solid oral dosage forms with focused beam measurement (FBRM) technology," (Poster presentation), AAPS Annual Meeting and Exposition. Los Angeles, CA. *AAPS J.*, vol. 11, no. 2, pp. 1162, 2009.

[139] K. Dave, P. E. Luner, C. Forness, D. Baker, C. Jankovsky, and S. Chen, "Feasibility of focused beam reflectance measurement (FBRM) for analysis of pharmaceutical suspensions in preclinical development," *AAPS PharmSciTech*, vol. 19, no. 1, pp. 155–165, 2018, doi: 10.1208/s12249-017-0819-9.

[140] C. F. Rawlinson-Malone, A. P. Ferreira, D. Nicholls, and S. Nicholson, "Elucidating spray-dried dispersion dissolution mechanisms with focused beam reflectance measurement: contribution of polymer chemistry and particle properties to performance," *Pharm. Dev. Technol.*, vol. 24, no. 9, pp. 1055–1062, 2019, doi: 10.1080/10837450.2018.1559189.

[141] A. S. Narang *et al.*, "Resolution and sensitivity of inline focused beam reflectance measurement during wet granulation in pharmaceutically relevant particle size ranges," *J. Pharm. Sci.*, vol. 105, no. 12, pp. 3594–3602, 2016, doi: 10.1016/j.xphs.2016.09.001.

[142] R. G. Sparks and C. L. Dobbs, "The use of laser backscatter instrumentation for the on-line measurement of the particle size distribution of emulsions," *Part. Part. Syst. Charact.*, vol. 10, no. 5, pp. 279–289, 1993, doi: 10.1002/ppsc.19930100512.

[143] Z. Qiao, Z. Wang, C. Zhang, S. Yuan, Y. Zhu, and J. Wang, "PVAm–PIP/PS composite membrane with high performance for CO_2/N_2 separation," *AIChE J.*, vol. 59, no. 4, pp. 215–228, 2012, doi: 10.1002/aic.13781.

[144] S. Schorsch, D. R. Ochsenbein, T. Vetter, M. Morari, and M. Mazzotti, "High accuracy online measurement of multidimensional particle size distributions during crystallization," *Chem. Eng. Sci.*, vol. 105, no. February, pp. 155–168,

2014, doi: 10.1016/j.ces.2013.11.003.

[145] J. Emmerich, Q. Tang, Y. Wang, P. Neubauer, S. Junne, and S. Maaß, "Optical inline analysis and monitoring of particle size and shape distributions for multiple applications: Scientific and industrial relevance," *Chinese J. Chem. Eng.*, vol. 27, no. 2, pp. 257–277, 2019, doi: 10.1016/j.cjche.2018.11.011.

[146] S. Zölls *et al.*, "Flow imaging microscopy for protein particle analysis - A comparative evaluation of four different analytical instruments," *AAPS J.*, vol. 15, no. 4, pp. 1200–1211, 2013, doi: 10.1208/s12248-013-9522-2.

[147] J. Østergaard *et al.*, "Real-time UV imaging of nicotine release from transdermal patch," *Pharm. Res.*, vol. 27, no. 12, pp. 2614–2623, 2010, doi: 10.1007/s11095-010-0257-9.

[148] F. Ye, A. Yaghmur, H. Jensen, S. W. Larsen, C. Larsen, and J. Østergaard, "Real-time UV imaging of drug diffusion and release from Pluronic F127 hydrogels," *Eur. J. Pharm. Sci.*, vol. 43, no. 4, pp. 236–243, 2011, doi: 10.1016/j.ejps.2011.04.015.

[149] Y. C. Shen, "Terahertz pulsed spectroscopy and imaging for pharmaceutical applications: A review," *Int. J. Pharm.*, vol. 417, no. 1–2, pp. 48–60, 2011, doi: 10.1016/j.ijpharm.2011.01.012.

[150] J. A. Zeitler, P. F. Taday, D. A. Newnham, M. Pepper, K. C. Gordon, and T. Rades, "Terahertz pulsed spectroscopy and imaging in the pharmaceutical setting - a review," *J. Pharm. Pharmacol.*, vol. 59, no. 2, pp. 209–223, 2010, doi: 10.1211/jpp.59.2.0008.

[151] P. Wray, J. Li, L. Q. Li, and S. G. Kazarian, "Combined study of biphasic and zero-order release formulations with dissolution tests and ATR-FTIR spectroscopic imaging," *J. Pharm. Sci.*, vol. 103, no. 7, pp. 1995–2004, 2014, doi: 10.1002/jps.23987.

[152] B. N. Singh, "Product development, manufacturing, and packaging of solid dosage forms under QbD and PAT paradigm: DOE case studies for industrial applications," *AAPS PharmSciTech*, vol. 20, no. 8, pp. 1–49, 2019, doi:

10.1208/s12249-019-1515-8.

[153] K. Raza, “Polymorphism: The phenomenon affecting the performance of drugs,” *SOJ Pharm. Pharm. Sci.*, vol. 1, no. 2, pp. 1-10, 2014, doi: 10.15226/2374-6866/1/2/00111.

[154] V. P. Wallace *et al.*, “Terahertz pulsed imaging and spectroscopy for biomedical and pharmaceutical applications,” *Faraday Discuss.*, vol. 126, no. 1, pp. 255–263, 2004, doi: 10.1039/b309357n.

[155] D. L. Galata *et al.*, “Raman mapping-based non-destructive dissolution prediction of sustained-release tablets,” *J. Pharm. Biomed. Anal.*, vol. 212, no. April, pp. 1–9, 2022, doi: 10.1016/j.jpba.2022.114661.

[156] D. L. Galata *et al.*, “Comparing the performance of Raman and near-infrared imaging in the prediction of the *in vitro* dissolution profile of extended-release tablets based on artificial neural networks,” *Pharmaceuticals*, vol. 16, no. 9, pp. 1–12, 2023, doi: 10.3390/ph16091243.

[157] *MATLAB Image processing toolbox*, The MathWorks, Inc., Natick, MA, USA, 2022. Accessed: Aug. 25, 2020. [Online]. Available: https://uk.mathworks.com/products/image-processing.html

[158] D. Treffer *et al.*, “In-line implementation of an image-based particle size measurement tool to monitor hot-melt extruded pellets,” *Int. J. Pharm.*, vol. 466, no. 1–2, pp. 181–189, 2014, doi: 10.1016/j.ijpharm.2014.03.022.

[159] C. Li, C. Amador, and Y. Ding, “An investigation on dissolution kinetics of single sodium carbonate particle with image analysis method,” *Chinese J. Chem. Eng.*, vol. 24, no. 10, pp. 1487–1496, 2016, doi: 10.1016/j.cjche.2016.08.001.

[160] E. Paladino *et al.*, “High spatial resolution ToF-SIMS imaging and image analysis strategies to monitor and quantify early phase separation in amorphous solid dispersions,” *Int. J. Pharm.*, vol. 628, no. August, pp. 1–12, 2022, doi: 10.1016/j.ijpharm.2022.122191.

[161] P. P. Doroyński, P. Kulinowski, A. Młynarczyk, and G. J. Stanisz, “Foundation

review: MRI as a tool for evaluation of oral controlled release dosage forms," *Drug Discov. Today*, vol. 17, no. 3–4, pp. 110–123, 2012, doi: 10.1016/j.drudis.2011.10.026.

[162] J. F. Gamble, M. Tobyn, and R. Hamey, "Application of image-based particle size and shape characterization systems in the development of small molecule pharmaceuticals," *J. Pharm. Sci.*, vol. 104, no. 5, pp. 1563–1574, 2015, doi: 10.1002/jps.24382.

[163] M. M. Leane, I. Cumming, and O. I. Corrigan, "The use of artificial neural networks for the selection of the most appropriate formulation and processing variables in order to predict the *in vitro* dissolution of sustained release minitablets," *AAPS PharmSciTech*, vol. 4, no. 2, pp. 1–12, 2003, doi: 10.1208/pt040226.

[164] D. M. D'Arcy, B. Liu, and O. I. Corrigan, "Investigating the effect of solubility and density gradients on local hydrodynamics and drug dissolution in the USP 4 dissolution apparatus," *Int. J. Pharm.*, vol. 419, no. 1–2, pp. 175–185, 2011, doi: 10.1016/j.ijpharm.2011.07.048.

[165] S. Ibrić, J. Djuriš, J. Parojčić, and Z. Djurić, "Artificial neural networks in evaluation and optimization of modified release solid dosage forms," *Pharmaceutics*, vol. 4, no. 4, pp. 531–550, 2012, doi: 10.3390/pharmaceutics4040531.

[166] A. Mendyk *et al.*, "From heuristic to mathematical modeling of drugs dissolution profiles: Application of artificial neural networks and genetic programming," *Comput. Math. Methods Med.*, vol. 2015, no. 863874, pp. 1–9, 2015, doi: 10.1155/2015/863874.

[167] S. Agatonovic-Kustrin and R. Beresford, "Basic concepts of artificial neural network (ANN) modeling and its application in pharmaceutical research," *J. Pharm. Biomed. Anal.*, vol. 22, no. 5, pp. 717–727, 2000, doi: 10.1016/S0731-7085(99)00272-1.

[168] Y. Mahdi, L. Mouhi, N. Guemras, and K. Daoud, "Coupling the image analysis and

the artificial neural networks to predict a mixing time of a pharmaceutical powder," *J. Fundam. Appl. Sci.*, vol. 8, no. 3, pp. 655–670, 2018, doi: 10.4314/jfas.v8i3.1.

[169] Y. Mintz and R. Brodie, "Introduction to artificial intelligence in medicine," *Minim. Invasive Ther. Allied Technol.*, vol. 28, no. 2, pp. 73–81, 2019, doi: 10.1080/13645706.2019.1575882.

[170] M. Franke, *Managing Airline Networks. Chapter 12: Machine learning and artificial intelligence.* Routledge, London, UK, 2020, pp. 153–159, doi: 10.4324/9780429318795-15.

[171] D. L. Galata *et al.*, "Applications of machine vision in pharmaceutical technology: A review," *Eur. J. Pharm. Sci.*, vol. 159, no. November 2020, pp. 1–24, 2021, doi: 10.1016/j.ejps.2021.105717.

[172] B. Nagy, D. László, G. Attila, F. Zsombor, and K. Nagy, "Application of artificial neural networks in the process analytical technology of pharmaceutical manufacturing — a review," *AAPS J.*, vol. 24, no. 74, pp. 1–18, 2022, doi: 10.1208/s12248-022-00706-0.

[173] B. Nagy *et al.*, "Application of artificial neural networks for process analytical technology-based dissolution testing," *Int. J. Pharm.*, vol. 567, no. March, pp. 1–12, 2019, doi: 10.1016/j.ijpharm.2019.118464.

[174] W. S. McCullouch and W. Pitts, "A logical calculus of the ideas immanent in nervous activity," *Bull. Math. Biophys.*, vol. 5, no. 4, pp. 115–133, 1943, doi: 10.1007/BF02478259.

[175] N. Muthukrishnan, F. Maleki, K. Ovens, C. Reinhold, B. Forghani, and R. Forghani, "Brief history of artificial intelligence," *Neuroimaging Clin. N. Am.*, vol. 30, no. 4, pp. 393–399, 2020, doi: 10.1016/j.nic.2020.07.004.

[176] J. McCarthy, M. L. Minsky, N. Rochester, and C. E. Shannon, "A proposal for the Dartmouth summer research project on artificial intelligence, August 31, 1955," *AI Mag.*, vol. 27, no. 4, pp. 12–14, 2006, doi: 10.1609/aimag.v27i4.1904

[177] A. M. Turing, “Compution machinery and intelligence,” *Mind*, vol. 59, no. 236, pp. 433–464, 1950, doi: 10.1093/oso/9780198250791.003.0017

[178] F. Rosenblatt, “The perceptron: A probabilistic model for information storage and organization in the brain,” *Psychol. Rev.*, vol. 65, no. 6, pp. 386–408, 1958, doi: 10.1037/h0042519.

[179] *MATLAB Machine learning toolbox*, The MathWorks, Inc., Natick, MA, USA, 2022. Accessed: Aug. 25, 2022. [Online]. Available: https://uk.mathworks.com/help/stats/machine-learning-in-matlab.html

[180] *MATLAB Deep learning toolbox*, The MathWorks, Inc., Natick, MA, USA, 2022. Accessed: Aug. 25, 2022. [Online]. Available: https://uk.mathworks.com/help/deeplearning/

[181] C. Aktolun, “Artificial intelligence and radiomics in nuclear medicine: potentials and challenges,” *Eur. J. Nucl. Med. Mol. Imaging*, vol. 46, no. February, pp. 2731–2736, 2019, doi: 10.1007/s00259-019-04593-0.

[182] D. Visvikis *et al.*, “Application of artificial intelligence in nuclear medicine and molecular imaging: A review of current status and future perspectives for clinical translation,” *Eur. J. Nucl. Med. Mol. Imaging*, vol. 49, no. July, pp. 4452–4463, 2022, doi: 10.1007/s00259-022-05891-w.

[183] R. Hesse, F. Krull, and S. Antonyuk, “Prediction of random packing density and flowability for non-spherical particles by deep convolutional neural networks and discrete element method simulations,” *Powder Technol.*, vol. 393, no. November, pp. 559–581, 2021, doi: 10.1016/j.powtec.2021.07.056.

[184] E. Westphal and H. Seitz, “A machine learning method for defect detection and visualization in selective laser sintering based on convolutional neural networks,” *Addit. Manuf.*, vol. 41, no. May, pp. 1–13, 2021, doi: 10.1016/j.addma.2021.101965.

[185] A. V Joshi, *Machine learning and artificial intelligence*, Springer Cham, Switzerland AG, 2020. doi: 10.1007/978-3-031-12282-8.

[186] Abishek Gupta, “Difference between ANN, CNN and RNN - GeeksforGeeks,” *Geeksforgeeks*, 2023. Accessed: 15 March 2024. [Online]. Available: https://www.geeksforgeeks.org/difference-between-ann-cnn-and-rnn/

[187] M. K. Das and T. Chakraborty, *Artificial neural network for drug design, delivery and disposition. Chapter 14: ANN in pharmaceutical product and process development*. Elsevier Inc., 2016, pp. 277-293, doi: 10.1016/B978-0-12-801559-9.00014-4.

[188] Y. Sun, Y. Peng, Y. Chen, and A. J. Shukla, “Application of artificial neural networks in the design of controlled release drug delivery systems,” *Adv. Drug Deliv. Rev.*, vol. 55, no. 9, pp. 1201–1215, 2003, doi: 10.1016/S0169-409X(03)00119-4.

[189] V. B. Sutariya, A. Groshev, and Y. V. Pathak, “Artificial neural network in drug delivery and pharmaceutical research,” *Open Bioinforma. J.*, vol. 7, no. suppl. 1, pp. 49–62, 2013, doi: 10.2174/1875036201307010049.

[190] K. K. Peh, C. P. Lim, S. S. Quek, and K. H. Khoh, “Use of artificial neural networks to predict drug dissolution profiles and evaluation of network performance using similarity factor,” *Pharm. Res.*, vol. 17, no. 11, pp. 1384–1388, 2000, doi: 10.1023/A:1007578321803.

[191] Y. Lecun, Y. Bengio, and G. Hinton, “Deep learning,” *Nature*, vol. 521, no. 7553, pp. 436–444, 2015, doi: 10.1038/nature14539.

[192] W. Y. Goh, C. P. Lim, K. K. Peh, and K. Subari, “Application of a recurrent neural network to prediction of drug dissolution profiles,” *Neural Comput. Appl.*, vol. 10, no. 4, pp. 311–317, 2002, doi: 10.1007/s005210200003.

[193] J. Ilonen, R. Juránek, T. Eerola, L. Lensu, M. Dubská, and P. Zem, “Comparison of bubble detectors and size distribution estimators,” *Pattern Recognit. Lett.*, vol. 101, no. January, pp. 60–66, 2018, doi: 10.1016/j.patrec.2017.11.014.

[194] T. Haas, C. Schubert, M. Eickhoff, and H. Pfeifer, “BubCNN: Bubble detection using faster RCNN and shape regression network,” *Chem. Eng. Sci.*, vol. 216, no.

115467, pp. 1–13, 2020, doi: 10.1016/j.ces.2019.115467.

[195] I. Poletaev, M. P. Tokarev, and K. S. Pervunin, “Bubble patterns recognition using neural networks: Application to the analysis of a two-phase bubbly jet,” *Int. J. Multiph. Flow*, vol. 126, no. May, pp. 1–14, 2020, doi: 10.1016/j.ijmultiphaseflow.2019.103194.

[196] E. S. Kostewicz *et al.*, “*In vitro* models for the prediction of *in vivo* performance of oral dosage forms,” *Eur. J. Pharm. Sci.*, vol. 57, no. 1, pp. 342–366, 2014, doi: 10.1016/j.ejps.2013.08.024.

[197] European Pharmacopoeia 11.0. Appendix XII, “Recommendations on Dissolution Testing (Ph. Eur. 2.9.3) EDQM, Strasbourg, France.,” (Monograph), pp. 3–8, 2023. [Online]. Available: http://www.uspbpep.com/ep60/2.9

[198] J. Alsenz and M. Kansy, “High throughput solubility measurement in drug discovery and development,” *Adv. Drug Deliv. Rev.*, vol. 59, no. 7, pp. 546–567, 2007, doi: 10.1016/j.addr.2007.05.007.

[199] J. Lu, V. Behbood, P. Hao, H. Zuo, S. Xue, and G. Zhang, “Transfer learning using computational intelligence: A survey,” *Knowledge-Based Syst.*, vol. 80, no. May, pp. 14–23, 2015, doi: 10.1016/j.knosys.2015.01.010.

[200] P. Liznerski, L. Ruff, R. A. Vandermeulen, B. J. Franks, M. Kloft, and K.-R. Müller, “Explainable deep one-class classification,” *ICRL*, 2020, Accessed: June. 25, 2021. [Online]. Available: http://arxiv.org/abs/2007.01760

[201] F. Luis and G. Moncayo, *Drug-like properties: Concepts, structure design and methods*. Elsevier Inc., 2008. ISBN: 978-0-12-369520-8.

[202] L. Zoller *et al.*, “A comparison of USP 2 and µDISS Profiler™ apparatus for studying dissolution phenomena of ibuprofen and its salts,” *Eur. J. Pharm. Sci.*, vol. 193, no. February, pp. 1–11, 2024, doi: 10.1016/j.ejps.2023.106684.

[203] M. Maghsoodi and F. Kiafar, “Co-precipitation with PVP and agar to improve physicomechanical properties of ibuprofen,” *Iran. J. Basic Med. Sci.*, vol. 16, no. 4, pp. 627–634, 2013, PMCID: PMC3830754

[204] A. Pali, G. C. Ordean, G. M. Pomian, L. L. Rus, and R. I. Iovanov, “A study on the influence of the dissolution test factors on *in vitro* release of ibuprofen from sustained release tablets,” *Rom. J. Pharm. Pract.*, vol. 13, no. 2, pp. 79–86, 2020, doi: 10.37897/RJPhP.2020.2.6.

[205] M. Madzarevic *et al.*, “Optimization and prediction of ibuprofen release from 3D DLP printlets using artificial neural networks,” *Pharmaceutics*, vol. 11, no. 10, pp. 1–16, 2019, doi: 10.3390/pharmaceutics11100544.

[206] R. Jamil and J. E. Polli, “Prediction of food effect on *in vitro* drug dissolution into biorelevant media: Contributions of solubility enhancement and relatively low colloid diffusivity,” *Eur. J. Pharm. Sci.*, vol. 177, no. October, pp. 1–39, 2022, doi: 10.1016/j.ejps.2022.106274.

[207] M. M. De Villiers, “Influence of agglomeration of cohesive particles on the dissolution behaviour of furosemide powder,” *Int. J. Pharm.*, vol. 136, no. 1–2, pp. 175–179, 1996, doi: 10.1016/0378-5173(95)04380-2.

[208] Z. Q. Yu, J. W. Chew, P. S. Chow, and R. B. H. Tan, “Recent advances in crystallization control: An industrial perspective,” *Chem. Eng. Res. Des.*, vol. 85, no. 7, pp. 893–905, 2007, doi: 10.1205/cherd06234.

[209] C. D. Papageorgiou *et al.*, “Development of screening methodology for the assessment of the agglomeration potential of APIs,” *Org. Process Res. Dev.*, vol. 20, no. 8, pp. 1500–1508, 2016, doi: 10.1021/acs.oprd.6b00201.

[210] S. Heisel, J. Holtkötter, and K. Wohlgemuth, “Measurement of agglomeration during crystallization: Is the differentiation of aggregates and agglomerates via ultrasonic irradiation possible?,” *Chem. Eng. Sci.*, vol. 210, no. December, pp. 1–10, 2019, doi: 10.1016/j.ces.2019.115214.

[211] M. Navas-Bachiller, T. Persoons, and D. M. D’Arcy, “Exploring bulk volume, particle size and particle motion definitions to increase the predictive ability of *in vitro* dissolution simulations,” *Eur. J. Pharm. Sci.*, vol. 174, no. October 2021, pp. 1–12, 2022, doi: 10.1016/j.ejps.2022.106185.

[212] R. Cristofoletti and J. B. Dressman, “Matching phosphate and maleate buffer

systems for dissolution of weak acids: Equivalence in terms of buffer capacity of bulk solution or surface pH?," *Eur. J. Pharm. Biopharm.*, vol. 103, no. June, pp. 104–108, 2016, doi: 10.1016/j.ejpb.2016.03.024.

[213] G. M. Khan and Z. Jiabi, "Preparation, characterization, and evaluation of physicochemical properties of different crystalline forms of ibuprofen," *Drug Dev. Ind. Pharm.*, vol. 24, no. 5, pp. 463–471, 1998, doi: 10.3109/03639049809085644.

[214] A. R. Taseva, T. Persoons, and D. M. D'Arcy, "Challenges and considerations of automated agglomeration detection method development with image analysis in dissolution testing," *Br. J. Pharm.*, vol. 7, no. 2, pp. 1–3, 2022, doi: 10.5920/bjpharm.1139.

[215] F. J. S. Doerr, C. J. Brown, and A. J. Florence, "Direct image feature extraction and multivariate analysis for crystallization process characterization," *Cryst. Growth Des.*, vol. 22, no. 4, pp. 2105–2116, 2022, doi: 10.1021/acs.cgd.1c01118.

[216] L. A. Mészáros *et al.*, "UV/VIS imaging-based PAT tool for drug particle size inspection in intact tablets supported by pattern recognition neural networks," *Int. J. Pharm.*, vol. 620, no. January, pp. 1–12, 2022, doi: 10.1016/j.ijpharm.2022.121773.

[217] S. Svanbäck, H. Ehlers, and J. Yliruusi, "Optical microscopy as a comparative analytical technique for single-particle dissolution studies," *Int. J. Pharm.*, vol. 469, no. 1, pp. 10–16, 2014, doi: 10.1016/j.ijpharm.2014.04.036.

[218] S. Svanbäck, H. Ehlers, and J. Yliruusi, "Optical microscopy as a comparative analytical technique for single-particle dissolution studies," *Int. J. Pharm.*, vol. 469, no. 1, pp. 10–16, 2014, doi: 10.1016/j.ijpharm.2014.04.036.

[219] X. Ma *et al.*, "Application of deep learning convolutional neural networks for internal tablet defect detection: High accuracy, throughput, and adaptability," *J. Pharm. Sci.*, vol. 109, no. 4, pp. 1547–1557, 2020, doi: 10.1016/j.xphs.2020.01.014.

[220] J. Jiang, X. Ma, D. Ouyang, and R. O. Williams, "Emerging artificial intelligence

(AI) technologies used in the development of solid dosage forms," *Pharmaceutics*, vol. 14, no. 2257, pp. 1–26, 2022, doi: 10.3390/pharmaceutics14112257.

[221] J. Štukelj, M. Agopov, J. Yliruusi, C. J. Strachan, and S. Svanbäck, "Machine-vision-enabled salt dissolution analysis," *Anal. Chem.*, vol. 92, no. 14, pp. 9730–9738, 2020, doi: 10.1021/acs.analchem.0c01068.

[222] J. Đuriš, I. Kurćubić, and S. Ibrić, "Review of machine learning algorithms' application in pharmaceutical technology," *Arh. Farm. (Belgr).*, vol. 71, no. 4, pp. 302–317, 2021, doi: 10.5937/arhfarm71-32499.

[223] T. Nunn and J. Williams, "Formulation of medicines for children," *Br. J. Clin. Pharmacol.*, vol. 59, no. 6, pp. 674–676, 2005, doi: 10.1111/j.1365-2125.2005.02410.x.

[224] G. Shiko, L. F. Gladden, A. J. Sederman, P. C. Connolly, and J. M. Butler, "MRI studies of the hydrodynamics in a USP 4 dissolution testing Cell," *J. Pharm. Sci.*, vol. 100, no. 3, pp. 976–991, 2011, doi: 10.1002/jps.22343.

[225] S. R. Cammarn and A. Sakr, "Predicting dissolution via hydrodynamics: Salicylic acid tablets in flow through cell dissolution," *Int. J. Pharm.*, vol. 201, no. 2, pp. 199–209, 2000, doi: 10.1016/S0378-5173(00)00415-4.

[226] M. Kakhi, "Mathematical modeling of the fluid dynamics in the flow-through cell," *Int. J. Pharm.*, vol. 376, no. 1–2, pp. 22–40, 2009, doi: 10.1016/j.ijpharm.2009.04.012.

[227] D. M. D'Arcy, B. Liu, G. Bradley, A. M. Healy, and O. I. Corrigan, "Hydrodynamic and species transfer simulations in the USP 4 dissolution apparatus: Considerations for dissolution in a low velocity pulsing flow," *Pharm. Res.*, vol. 27, no. 2, pp. 246–258, 2010, doi: 10.1007/s11095-009-0010-4.

[228] G. Shiko, A. J. Sederman, and L. F. Gladden, "MRI technique for the snapshot imaging of quantitative velocity maps using RARE," *J. Magn. Reson.*, vol. 216, no. March, pp. 183–191, 2012, doi: 10.1016/j.jmr.2012.01.021.

[229] H. Yoshida, A. Kuwana, H. Shibata, K. I. Izutsu, and Y. Goda, “Particle image velocimetry evaluation of fluid flow profiles in USP 4 flow-through dissolution cells,” *Pharm. Res.*, vol. 32, no. 9, pp. 2950–2959, 2015, doi: 10.1007/s11095-015-1676-4.

[230] J. Kukura, P. E. Arratia, E. S. Szalai, and F. J. Muzzio, “Engineering tools for understanding the hydrodynamics of dissolution tests,” *Drug Dev. Ind. Pharm.*, vol. 29, no. 2, pp. 231–239, 2003, doi: 10.1081/DDC-120016731.

[231] M. Morihara, N. Aoyagi, N. Kaniwa, N. Katori, and S. Kojim, “Hydrodynamic flows around tablets in different pharmacopeial dissolution tests,” *Drug Dev. Ind. Pharm.*, vol. 28, no. 6, pp. 655–662, 2002, doi: 10.1081/DDC-120003856.

[232] N. Fotaki, “Flow-through cell apparatus (USP Apparatus 4): Operation and features,” *Dissolution Technol.*, vol. 18, no. 4, pp. 46–49, 2011, doi: 10.14227/DT180411P46.

[233] J. Johansson, M. Cauchi, and M. Sundgren, “Multiple fiber-optic dual-beam UV/Vis system with application to dissolution testing,” *J. Pharm. Biomed. Anal.*, vol. 29, no. 3, pp. 469–476, 2002, doi: 10.1016/S0731-7085(02)00091-2.

[234] E. S. Kostewicz, M. Wunderlich, U. Brauns, R. Becker, T. Bock, and J. B. Dressman, “Predicting the precipitation of poorly soluble weak bases upon entry in the small intestine,” *J. Pharm. Pharmacol.*, vol. 56, no. 1, pp. 43–51, 2004, doi: 10.1211/0022357022511.

[235] Y. Chen, T. W. McCall, A. R. Baichwal, and M. C. Meyer, “The application of an artificial neural network and pharmacokinetic simulations in the design of controlled-release dosage forms,” *J. Control. Release*, vol. 59, no. 1, pp. 33–41, 1999, doi: 10.1016/S0168-3659(98)00171-0.

[236] P. M. Sathe and J. Venitz, “Comparison of neural network and multiple linear regression as dissolution predictors,” *Drug Dev. Ind. Pharm.*, vol. 29, no. 3, pp. 349–355, 2003, doi: 10.1081/DDC-120018209.

[237] A. Hermans *et al.*, “Challenges and strategies for solubility measurements and dissolution method development for amorphous solid dispersion formulations,”

AAPS J., vol. 25, no. 11, pp. 1–14, 2023, doi: 10.1208/s12248-022-00760-8.

[238] C. Reppas *et al.*, "Dissolution testing of modified release products with biorelevant media: An OrBiTo ring study using the USP apparatus III and IV," *Eur. J. Pharm. Biopharm.*, vol. 156, no. June, pp. 40–49, 2020, doi: 10.1016/j.ejpb.2020.08.025.

[239] A. C. Van der Vossen, L. M. Hanff, A. G. Vulto, and N. Fotaki, "Potential prediction of formulation performance in paediatric patients using biopharmaceutical tools and simulation of clinically relevant administration scenarios of nifedipine and lorazepam," *Br. J. Clin. Pharmacol.*, vol. 85, no. 8, pp. 1728–1739, 2019, doi: 10.1111/bcp.13956.

[240] K. Matsui, K. Nakamichi, M. Nakatani, H. Yoshida, S. Yamashita, and S. Yokota, "Lowly-buffered biorelevant dissolution testing is not necessarily biopredictive of human bioequivalence study outcome: Relationship between dissolution and pharmacokinetics," *Int. J. Pharm.*, vol. 631, no. August 2022, pp. 1–12, 2023, doi: 10.1016/j.ijpharm.2022.122531.

[241] D. M. Mudie, N. Samiei, D. J. Marshall, G. E. Amidon, and C. A. S. Bergström, "Selection of *in vivo* predictive dissolution media using drug substance and physiological properties," *AAPS J.*, vol. 22, no. 34, pp. 1–13, 2020, doi: 10.1208/s12248-020-0417-8.

[242] I. Loisios-Konstantinidis, R. Cristofoletti, N. Fotaki, D. B. Turner, and J. Dressman, "Establishing virtual bioequivalence and clinically relevant specifications using *in vitro* biorelevant dissolution testing and physiologically-based population pharmacokinetic modeling. case example: Naproxen," *Eur. J. Pharm. Sci.*, vol. 143, no. February, pp. 1–79, 2020, doi: 10.1016/j.ejps.2019.105170.

[243] S. Kim, E. Bilgili, and R. N. Davé, "Impact of altered hydrophobicity and reduced agglomeration on dissolution of micronized poorly water-soluble drug powders after dry coating," *Int. J. Pharm.*, vol. 606, no. May, pp. 1–16, 2021, doi: 10.1016/j.ijpharm.2021.120853.

[244] H. Higashino *et al.*, "*In vitro-in vivo* correlation of the effect of supersaturation

on the intestinal absorption of BCS class 2 drugs," *Mol. Pharm.*, vol. 11, no. 3, pp. 746–754, 2014, doi: 10.1021/mp400465p.

[245] A. Ruff, R. Holm, and E. S. Kostewicz, "Evaluating the predictability of the *in vitro* transfer model and *in vivo* rat studies as a surrogate to investigate the supersaturation and precipitation behaviour of different albendazole formulations for humans," *Eur. J. Pharm. Sci.*, vol. 105, no. May, pp. 108–118, 2017, doi: 10.1016/j.ejps.2017.04.024.

[246] D. Kou *et al.*, "*In vitro*, in silico, and *in vivo* assessments of intestinal precipitation and its impact on bioavailability of a BCS Class 2 basic compound," *Mol. Pharm.*, vol. 15, no. 4, pp. 1607–1617, 2018, doi: 10.1021/acs.molpharmaceut.7b01143.

[247] Y. Sun *et al.*, "UV − vis imaging of piroxicam supersaturation, precipitation, and dissolution in a flow-through setup," *Anal. Chem.*, vol. 90, no. MAy, pp. 6413–6418, 2018, doi: 10.1021/acs.analchem.8b00587.

[248] European Medicines Agency (EMA), "EMA Guideline on real time release testing (formerly Guideline on parametric release)," (Guideline), vol. 44, no. March. pp. 1–10, 2012. [Online].
Available: https://www.ema.europa.eu/en/documents/scientific-guideline/guideline-real-time-release-testing-formerly-guideline-parametric-release-revision-1_en.pdf

[249] L. A. Mészáros *et al.*, "Real-time release testing of *in vitro* dissolution and blend uniformity in a continuous powder blending process by NIR spectroscopy and machine vision," *Eur. J. Pharm. Biopharm.*, vol. 201, no. June, pp. 1–12, 2024, doi: 10.1016/j.ejpb.2024.114368.

[250] S. Sacher, A. Kottlan, J. B. Diop, and R. Heimsten, "Prediction of in-vitro dissolution and tablet hardness from optical porosity measurements," *Int. J. Pharm.*, vol. 660, no. June, pp. 1–8, 2024, doi: 10.1016/j.ijpharm.2024.124336.

[251] K. P. Nott, "Magnetic resonance imaging of tablet dissolution," *Eur. J. Pharm. Biopharm.*, vol. 74, no. 1, pp. 78–83, 2010, doi: 10.1016/j.ejpb.2009.07.003.

[252] C. van Haaren, M. De Bock, and S. G. Kazarian, “Advances in ATR-FTIR spectroscopic imaging for the analysis of tablet dissolution and drug release,” *Molecules*, vol. 28, no. 4705, pp. 1–24, 2023, doi: 10.3390/molecules28124705.

[253] K. C. Gordon and C. M. McGoverin, “Raman mapping of pharmaceuticals,” *Int. J. Pharm.*, vol. 417, no. 1–2, pp. 151–162, 2011, doi: 10.1016/j.ijpharm.2010.12.030.

[254] P. Zarmpi, T. Flanagan, E. Meehan, J. Mann, and N. Fotaki, “Surface dissolution UV imaging for characterization of superdisintegrants and their impact on drug dissolution,” *Int. J. Pharm.*, vol. 577, no. January, p. 1–12, 2020, doi: 10.1016/j.ijpharm.2020.119080.

[255] Z. Li *et al.*, “Towards functional characterization of excipients for oral solid dosage forms using UV–Vis imaging. Liberation, release and dissolution,” *J. Pharm. Biomed. Anal.*, vol. 194, no. February, pp. 1–9, 2021, doi: 10.1016/j.jpba.2020.113789.

[256] F. Fredholt, C. Di Meo, S. Sloth, A. Müllertz, and R. Berthelsen, “Direct visualizing of paracetamol immediate release tablet disintegration *in vivo* and *in vitro*,” *Eur. J. Pharm. Biopharm.*, vol. 180, no. August, pp. 63–70, 2022, doi: 10.1016/j.ejpb.2022.09.007.

[257] J. B. Dressman, G. L. Amidon, C. Reppas, and V. P. Shah, “Dissolution testing as a prognostic tool for oral drug absorption: immediate release dosage forms,” *Pharm. Res.*, vol. 15, no. 1, pp. 11–22, 1998, doi: 10.1023/a:1011984216775.

[258] J. Muselík, A. Komersová, K. Kubová, K. Matzick, and B. Skalická, “A critical overview of FDA and EMA statistical methods to compare *in vitro* drug dissolution profiles of pharmaceutical products,” *Pharmaceutics*, vol. 13, no. 10, pp. 1–12, 2021, doi: 10.3390/pharmaceutics13101703.

[259] G. Garbacz and S. Klein, “Dissolution testing of oral modified-release dosage forms,” *J. Pharm. Pharmacol.*, vol. 64, no. 7, pp. 944–968, 2012, doi: 10.1111/j.2042-7158.2012.01477.x.

[260] R. Aishwarya, A. Murthy, T. Ahmed, and S. Chachad, “A novel approach to justify

dissolution differences in an extended release drug product using physiologically based biopharmaceutics modeling and simulation," *J. Pharm. Sci.*, vol. 111, no. 6, pp. 1820–1832, 2022, doi: 10.1016/j.xphs.2022.02.007.

[261] M. Kubbinga, P. Langguth, and D. Barends, "Risk analysis in bioequivalence and biowaiver decisions," *Biopharm. Drug Dispos.*, vol. 34, no. November 2012, pp. 254–261, 2013, doi: 10.1002/bdd.

[262] T. R. Batesx, J. M. Young, C. M. Wu, and H. A. Rosenberg, "pH-dependent dissolution rate of nitrofurantoin from commercial suspensions, tablets, and capsules," vol. 63, no. 4, pp. 643–645, 1974, doi: 10.1002/jps.2600630441.

[263] M. Barzegar-Jalali and J. H. Richards, "The effect if suspending agents on the release of aspirin from aqueous suspennsions *in vitro*," *Int. J. Pharm.*, vol. 2, no. 3-4, pp. 195–201, 1979, doi: 10.1016/0378-5173(79)90020-6.

[264] S. A. Howard, J. Mauger, J. W. Hsieh, and K. Amin, "Suspending agent effects on steroid suspension dissolution profiles," *J. Pharm. Sci.*, vol. 68, no. 12, pp. 1475–1479, 1979, doi: 10.1002/jps.2600681203.

[265] N. L. G. Vidal, P. D. Zubata, L. D. Simionato, and M. T. Pizzorno, "Dissolution stability study of cefadroxil extemporaneous suspensions," *Dissolution Technol.*, vol. 15, no. 3, pp. 29–36, 2008, doi: 10.14227/DT150308P29.

[266] D. C. Ripple and Z. Hu, "Correcting the relative bias of light obscuration and flow imaging particle counters," *Pharm. Res.*, vol. 33, no. 3, pp. 653–672, 2016, doi: 10.1007/s11095-015-1817-9.

[267] H. Wang *et al.*, "Characterization of the suspension stability of pharmaceuticals using a shadowgraphic imaging method," *Int. J. Pharm.*, vol. 548, no. 1, pp. 128–138, 2018, doi: 10.1016/j.ijpharm.2018.06.053.

[268] F. W. A. Owusu *et al.*, "Formulation and *in vitro* evaluation of oral capsules and suspension from the ethanolic extract of Cola nitida seeds for the treatment of diarrhea," *Biomed Res. Int.*, vol. 2021, no. June, pp. 1-7, 2021, doi: 10.1155/2021/6630449.

[269] T. Felicijan, A. Krese, A. Mrhar, and M. Bogataj, “Applicability of bottom-view cameras for evaluation of tablet performance during dissolution testing,” *Dissolution Technol.*, vol. 23, no. 4, pp. 24–32, 2016, doi: 10.14227/DT230416P24.

[270] Y. Y. Chen, L. P. Hughes, L. F. Gladden, and M. D. Mantle, “Quantitative ultra-fast MRI of HPMC swelling and dissolution,” *J. Pharm. Sci.*, vol. 99, no. 8, pp. 3462–3472, 2010, doi: 10.1002/jps.22110.

[271] S. B. E. Andersson, G. Frenning, and G. Alderborn, “Determination of intrinsic drug dissolution and solute effective transport rate during laminar fluid flow at different velocities,” *Pharmaceutics*, vol. 13, no. 6, pp. 1–24, 2021, doi: 10.3390/pharmaceutics13060835.

[272] M. Bisrat and C. Nyström, “Physicochemical aspects of drug release. VIII. The relation between particle size and surface specific dissolution rate in agitated suspensions,” *Int. J. Pharm.*, vol. 47, no. 1–3, pp. 223–231, 1988, doi: 10.1016/0378-5173(88)90235-9.

[273] *MATLAB Statistics and machine learning toolbox*, The MathWorks, Inc., Natick, MA, USA, 2022. Accessed: Aug. 25, 2022. [Online]. Available: https://uk.mathworks.com/help/stats/

[274] A. S. Achanta, J. G. Kowalski, and C. T. Rhodes, “Artificial neural networks: Implications for pharmaceutical sciences,” *Drug Dev. Ind. Pharm.*, vol. 21, no. 1, pp. 119–155, 1995, doi: 10.3109/03639049509048099.

[275] N. K. Ebube, T. McCall, Y. Chen, and M. C. Meyer, “Relating formulation variables to *in vitro* dissolution using an artificial neural network,” *Pharm. Dev. Technol.*, vol. 2, no. 3, pp. 225–232, 1997, doi: 10.3109/10837459709031442.

[276] A. S. Hussain, R. D. Johnson, N. N. Vachharajani, and W. A. Ritschel, “Feasibility of developing a neural network for prediction of human pharmacokinetic parameters from animal data,” *Pharm. Res.*, vol. 10, no. 3, pp. 466–469, 1993, doi: 10.1023/a:1018917128684.

[277] Y. Peng, M. Geraldrajan, Q. Chen, Y. Sun, J. R. Johnson, and A. J. Shukla,

"Prediction of dissolution profiles of acetaminophen beads using artificial neural networks," *Pharm. Dev. Technol.*, vol. 11, no. 3, pp. 337–349, 2006, doi: 10.1080/10837450600769744.

[278] D. P. Medarević, P. Kleinebudde, J. Djuriš, Z. Djurić, and S. Ibrić, "Combined application of mixture experimental design and artificial neural networks in the solid dispersion development," *Drug Dev. Ind. Pharm.*, vol. 42, no. 3, pp. 389–402, 2016, doi: 10.3109/03639045.2015.1054831.

[279] S. Ibrić *et al.*, "Artificial neural networks in the modeling and optimization of aspirin extended release tablets with Eudragit L 100 as matrix substance," *AAPS PharmSciTech*, vol. 4, no. 1, pp. 1–9, 2003, doi: 10.1208/pt040109.

[280] I. A. Basheer and M. Hajmeer, "Artificial neural networks: Fundamentals, computing, design, and application," *J. Microbiol. Methods*, vol. 43, no. 1, pp. 3–31, 2000, doi: 10.1016/S0167-7012(00)00201-3.

[281] J. Petrović, S. Ibrić, G. Betz, J. Parojčić, and Z. Durić, "Application of dynamic neural networks in the modeling of drug release from polyethylene oxide matrix tablets," *Eur. J. Pharm. Sci.*, vol. 38, no. 2, pp. 172–180, 2009, doi: 10.1016/j.ejps.2009.07.007.

[282] B. Nagy *et al.*, "Interpretable artificial neural networks for retrospective QbD of pharmaceutical tablet manufacturing based on a pilot-scale developmental dataset," *Int. J. Pharm.*, vol. 633, no. January, pp. 1–11, 2023, doi: 10.1016/j.ijpharm.2023.122620.

[283] D. L. Galata, L. A. Mészáros, B. Nagy, and Z. K. Nagy, "Convolutional neural network-based evaluation of chemical maps obtained by fast Raman imaging for prediction of tablet dissolution profiles," *Int. J. Pharm.*, vol. 640, no. June, pp. 1–8, 2023, doi: 10.1016/j.ijpharm.2023.123001.

[284] Z. Salahuddin, H. C. Woodruff, A. Chatterjee, and P. Lambin, "Transparency of deep neural networks for medical image analysis: A review of interpretability methods," *Comput. Biol. Med.*, vol. 140, no. January, pp. 1–18, 2022, doi: 10.1016/j.compbiomed.2021.105111.

[285] U.S. Food and Drug Administration (FDA), “Artificial Intelligence in Drug Manufacturing,” (Discussion paper), 2023. [Online]. Available: https://www.fda.gov/media/165743/download

[286] European Medicines Agency (EMA), Committee for medicinal products for human use (CHMP), “ICH Q2 (R2) validation of analytical procedures,” (Guideline), vol. 2, no. December, pp. 1–33, 2023. [Online]. Available: https://www.ema.europa.eu/en/ich-q2r2-validation-analytical-procedures-scientific-guideline.

Appendix 1

Ibuprofen calibration curves in the UV-Vis spectrophotometer used for the solubility study and dissolution tests of the ibuprofen API powder presented in Chapters 3, 4 and 6.

Calibration curves for the dissolution tests of ibuprofen API were carried out by preparing dilutions of ibuprofen powder in pH 6.8 phosphate buffer with surfactant concentrations from 0 to 0.05% w/v Tween 20. The concentration ranges used were: 0.5 µg/mL to 20 µg/mL for Ibu-nd in PB 0% w/v (Figure A1.1), 0.003% w/v (Figure A1.2) and 0.01% w/v Tween 20 (Figure A1.3), 0.125 µg/mL to 20 µg/mL for Ibu-nd in PB 0.005% w/v (Figure A1.4) and 0.05% w/v Tween 20 (Figure A1.5) at 222 nm wavelength, and 30 µg/mL to 600 µg/mL for Ibu-nd in PB 0%w/v (Figure A1.6), 0.003% w/v (Figure A1.7) and 0.01% w/v Tween 20 (Figure A1.8), and 2 µg/mL to 600 µg/mL for Ibu-nd in PB 0.005% w/v (Figure A1.9) and 0.05% w/v Tween 20 (Figure A1.10) at 264 nm wavelength.

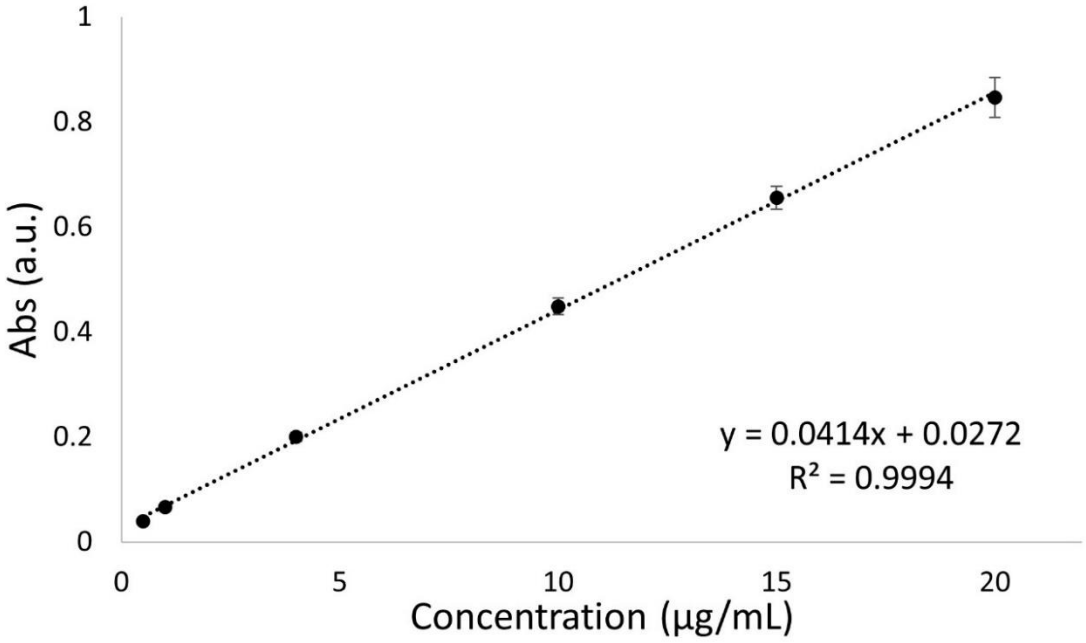

Figure A1.1: Mean absorbance (±SD) of ibuprofen API at concentrations of 0.5 µg/mL to 20 µg/mL in pH 6.8 PB 0% w/v Tween 20 at 222 nm (n = 3).

Mean absorbance (±SD) of ibuprofen API at concentrations of 0.5 µg/mL to 20 µg/mL in pH 6.8 PB 0% w/v Tween 20 at 222 nm (n = 3).

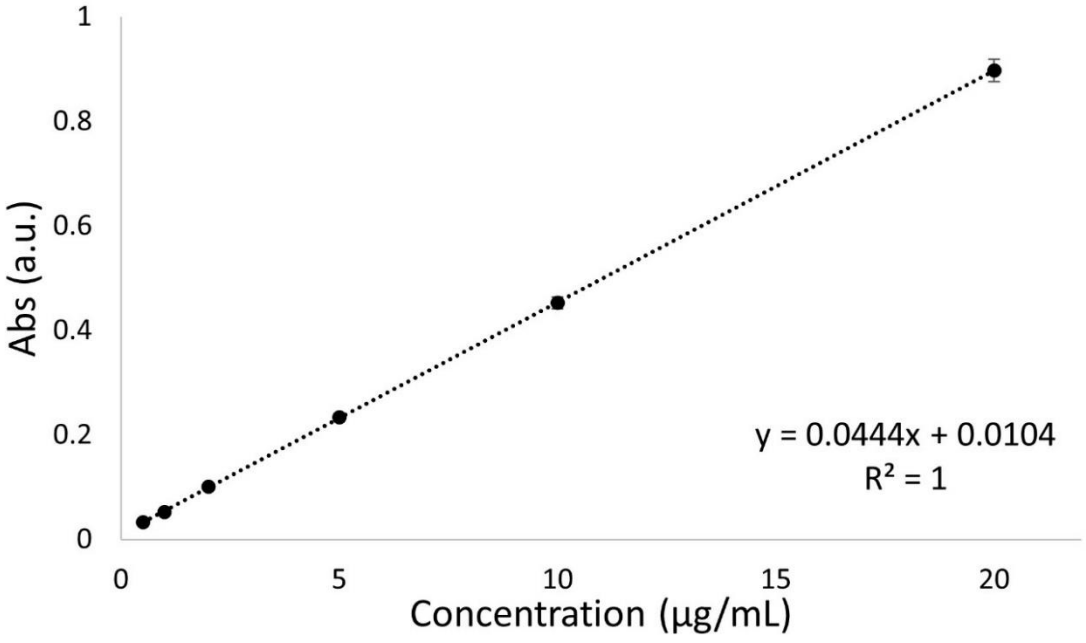

Figure A1.2: Mean absorbance (±SD) of ibuprofen API at concentrations of 0.5 µg/mL to 20 µg/mL in pH 6.8 PB 0.003% w/v Tween 20 at 222 nm (n = 3).

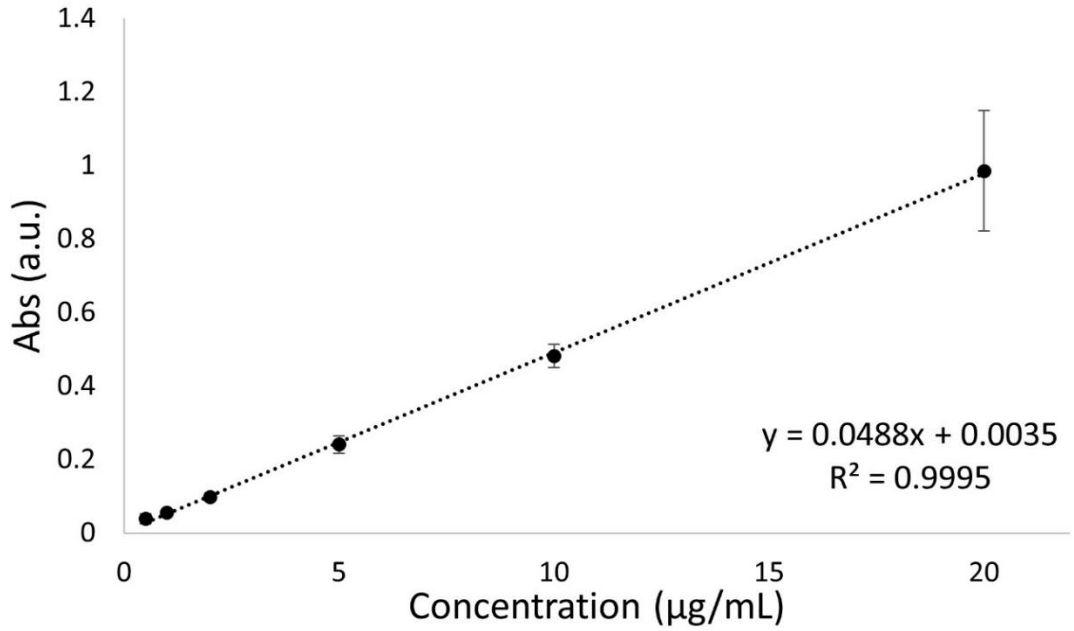

Figure A1.3: Mean absorbance (±SD) of ibuprofen API at concentrations of 0.5 µg/mL to 20 µg/mL in pH 6.8 PB 0.01% w/v Tween 20 at 222 nm (n = 3).

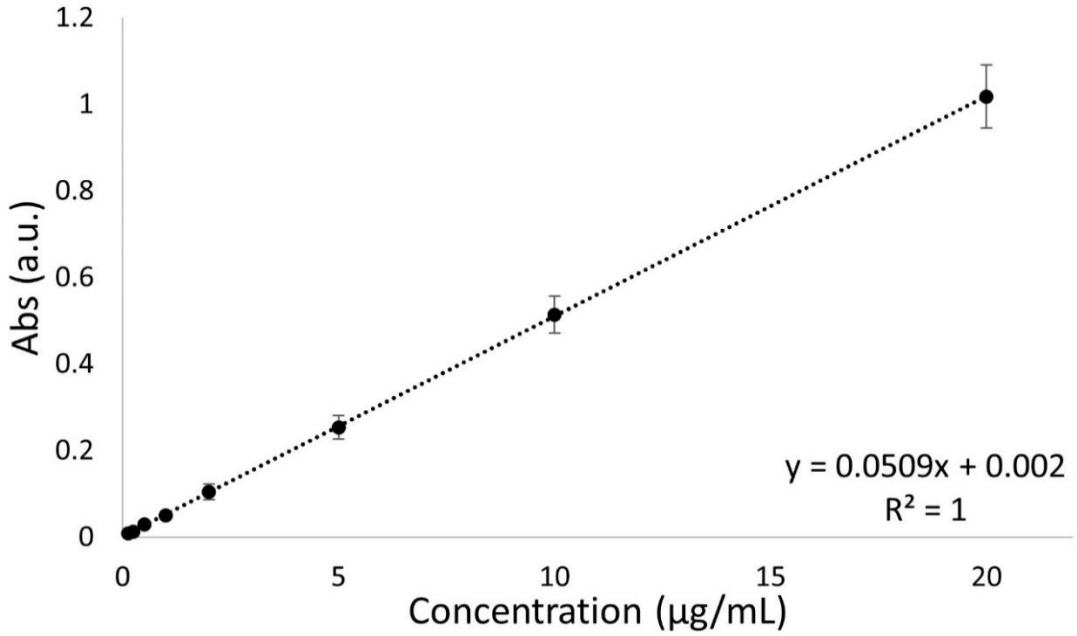

Figure A1.4: Mean absorbance (±SD) of ibuprofen API at concentrations of 0.125 µg/mL to 20 µg/mL in pH 6.8 PB 0.005% w/v Tween 20 at 222 nm (n = 3).

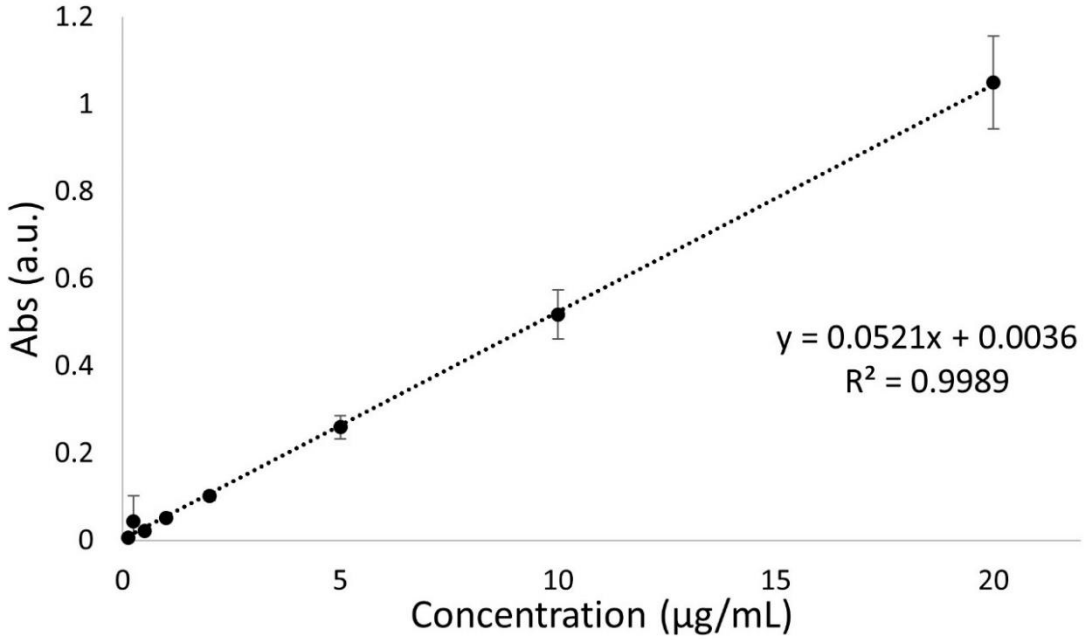

Figure A1.5: Mean absorbance (±SD) of ibuprofen API at concentrations of 0.125 µg/mL to 20 µg/mL in pH 6.8 PB 0.05% w/v Tween 20 at 222 nm (n = 3).

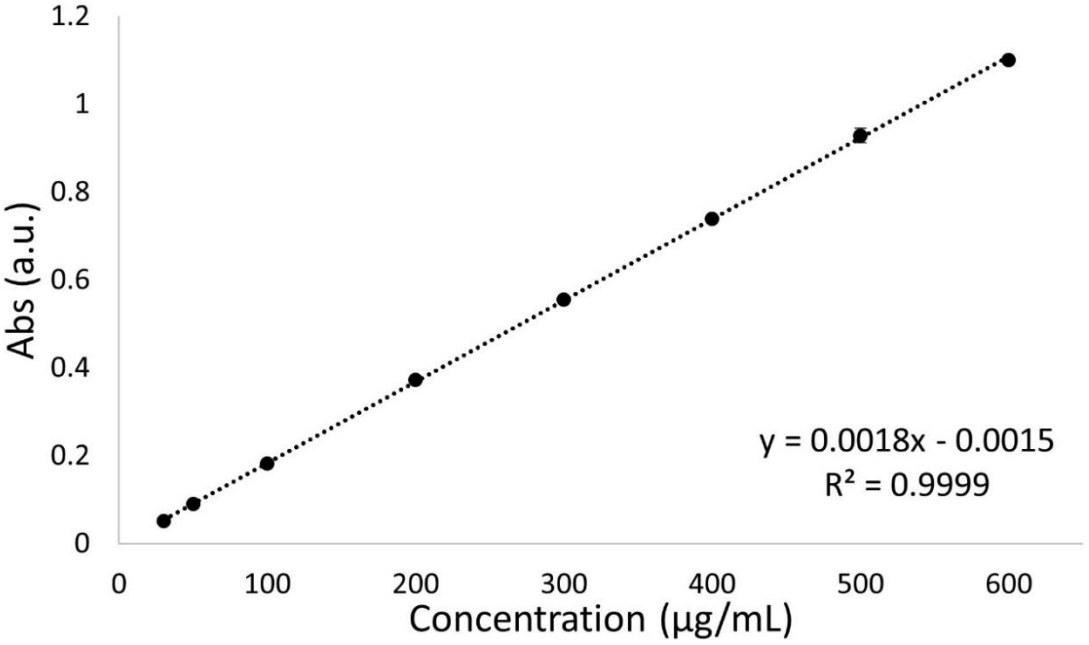

Figure A1.6: Mean absorbance (±SD) of ibuprofen API at concentrations of 30 µg/mL to 600 µg/mL in pH 6.8 PB 0% w/v Tween 20 at 264 nm (n = 3).

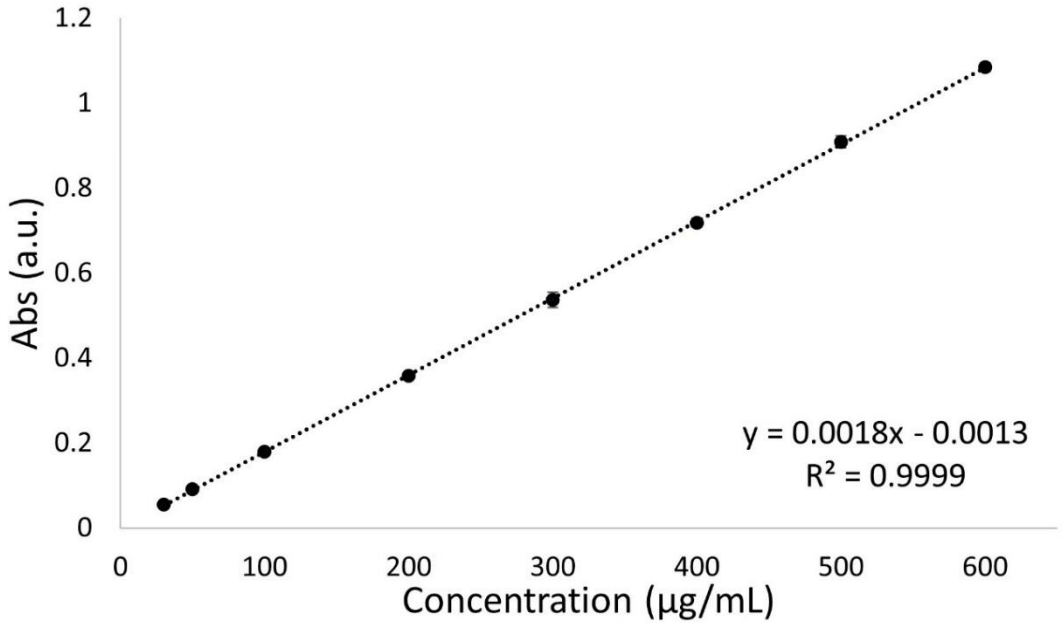

Figure A1.7: Mean absorbance (±SD) of ibuprofen API at concentrations of 30 µg/mL to 600 µg/mL in pH 6.8 PB 0.003% w/v Tween 20 at 264 nm (n = 3).

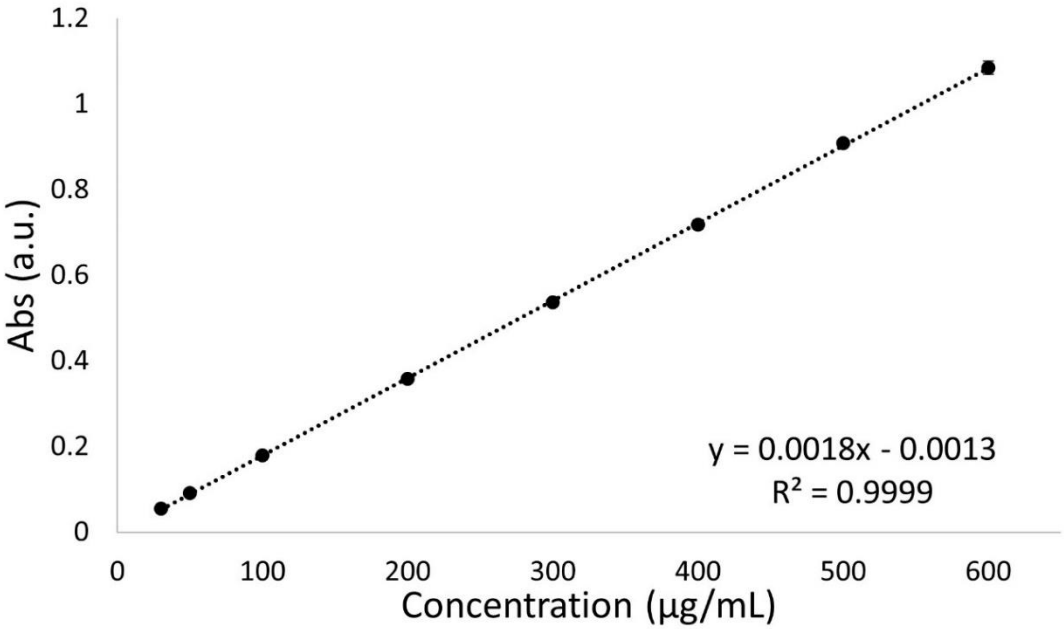

Figure A1.8: Mean absorbance (±SD) of ibuprofen API at concentrations of 30 µg/mL to 600 µg/mL in pH 6.8 PB 0.01% w/v Tween 20 at 264 nm (n = 3).

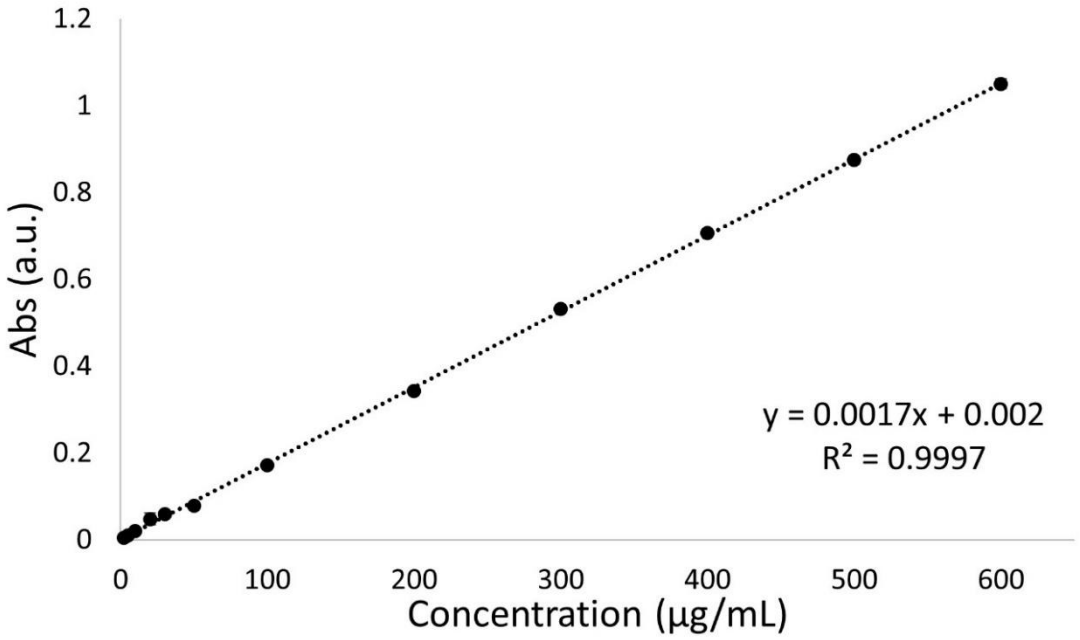

Figure A1.9: Mean absorbance (±SD) of ibuprofen API at concentrations of 2 µg/mL to 600 µg/mL in pH 6.8 PB 0.005% w/v Tween 20 at 264 nm (n = 3).

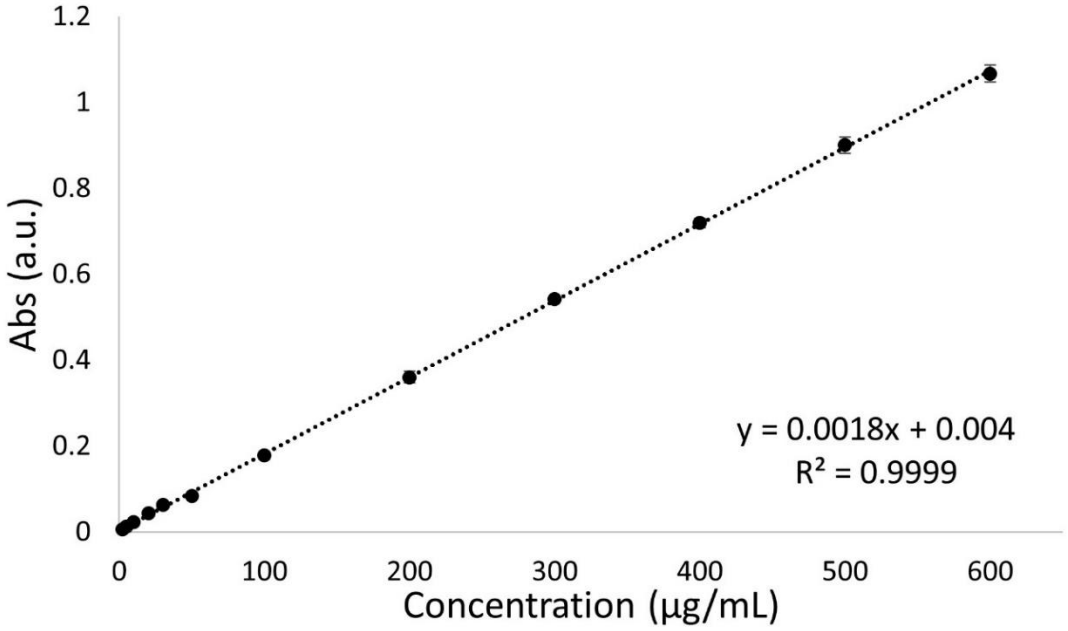

Figure A1.10: Mean absorbance (±SD) of ibuprofen API at concentrations of 2 µg/mL to 600 µg/mL in pH 6.8 PB 0.05% w/v Tween 20 at 264 nm (n = 3).

Ibuprofen calibration curves in the high-performance liquid chromatography (HPLC) used for the dissolution tests of the ibuprofen-containing oral suspensions Brupro and Nurofen presented in Chapter 5.

A calibration curve for the dissolution tests of ibuprofen-containing oral suspensions were carried out by preparing dilutions of ibuprofen powder (Ibu-nd) in PB, pH 6.8 (Figure A1.11). No surfactant was added to the medium for these studies.

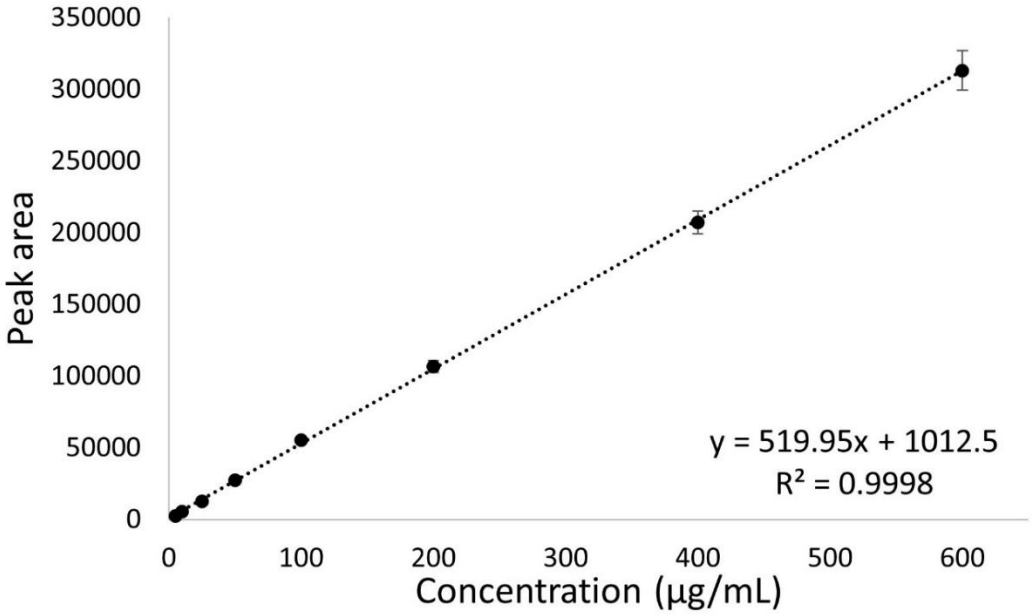

Figure A1.11: Mean absorbance (±SD) of ibuprofen API at concentrations of 5 µg/mL to 600 µg/mL in PB pH 6.8 at 254 nm (n = 3).

Appendix 2

Dissolution profiles of Ibu-nd, Ibu-nd-S and Ibu-pl-S from the dissolution tests performed in the USP 4 FTA CE1 used for SGI analysis presented in Chapter 3 (Figure A2.1 to Figure A2.7).

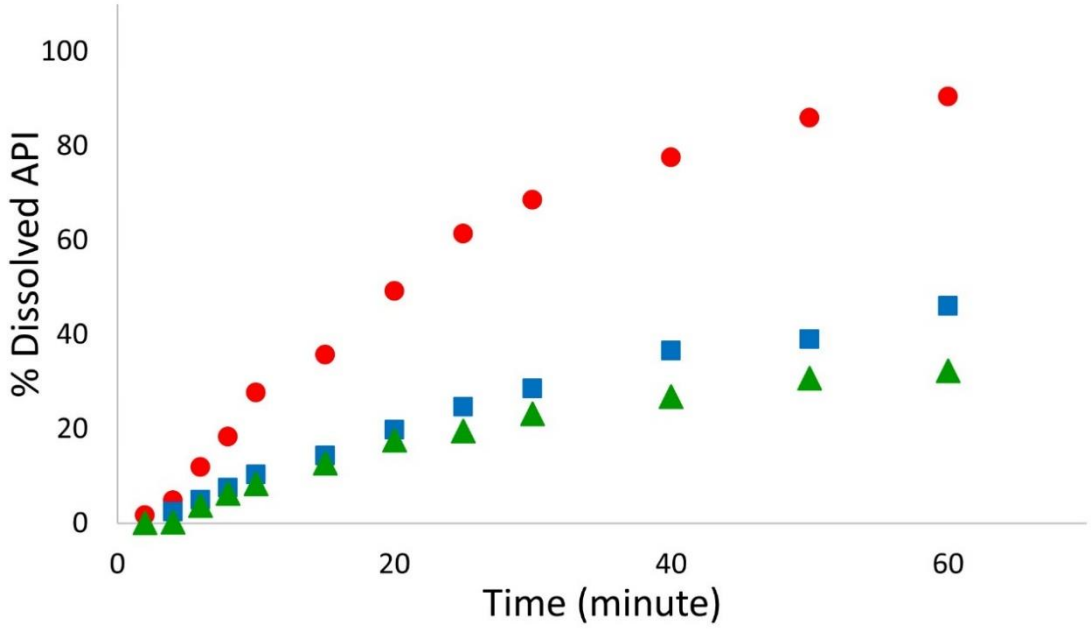

Figure A2.1: Dissolution profiles of 4 mg (red circle), 20 mg (blue square) and 100 mg (green triangle) Ibu-nd powder in phosphate buffer pH 6.8 with 0% w/v Tween 20 at FR 8 mL/min in the FTA CE1 22.6 mm diameter cell.

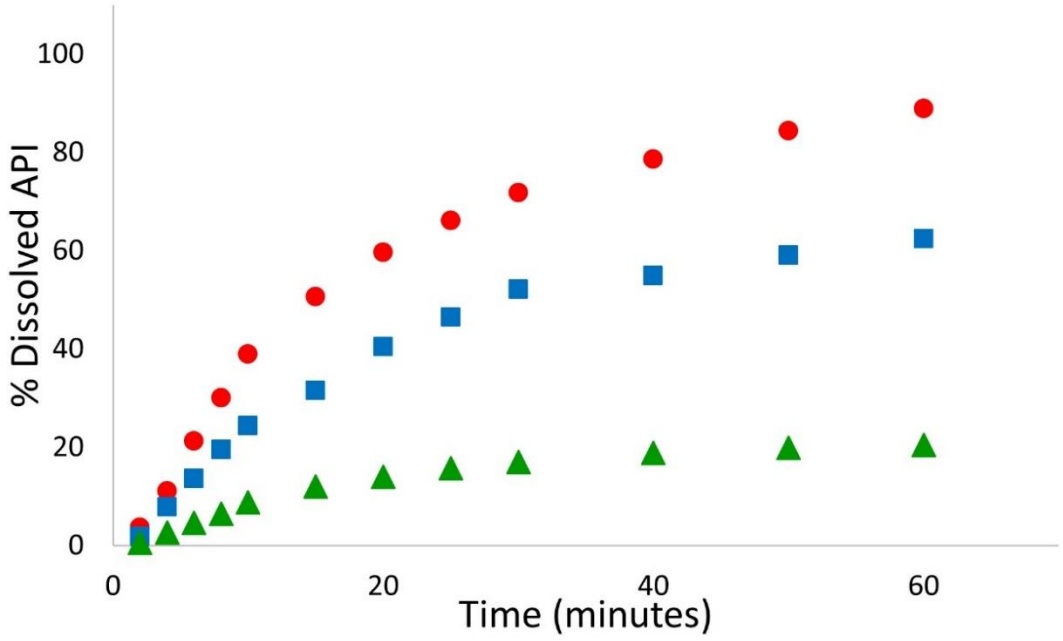

Figure A2.2: Dissolution profiles of 4 mg (red circle), 20 mg (blue square) and 100 mg (green triangle) Ibu-nd powder in phosphate buffer pH 6.8 with 0% w/v Tween 20 at 16 mL/min in the FTA CE1 22.6 mm diameter cell.

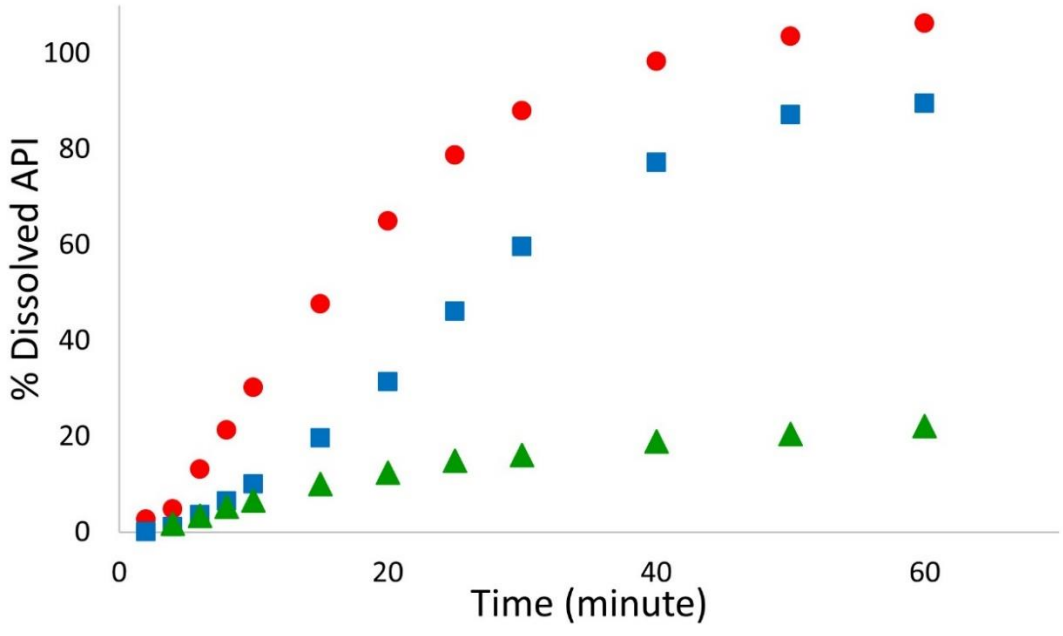

Figure A2.3: Dissolution profiles of 4 mg (red circle), 20 mg (blue square) and 100 mg (green triangle) Ibu-nd powder in phosphate buffer pH 6.8 with 0.005% w/v Tween 20 at FR 8 mL/min in the FTA CE1 22.6 mm diameter cell.

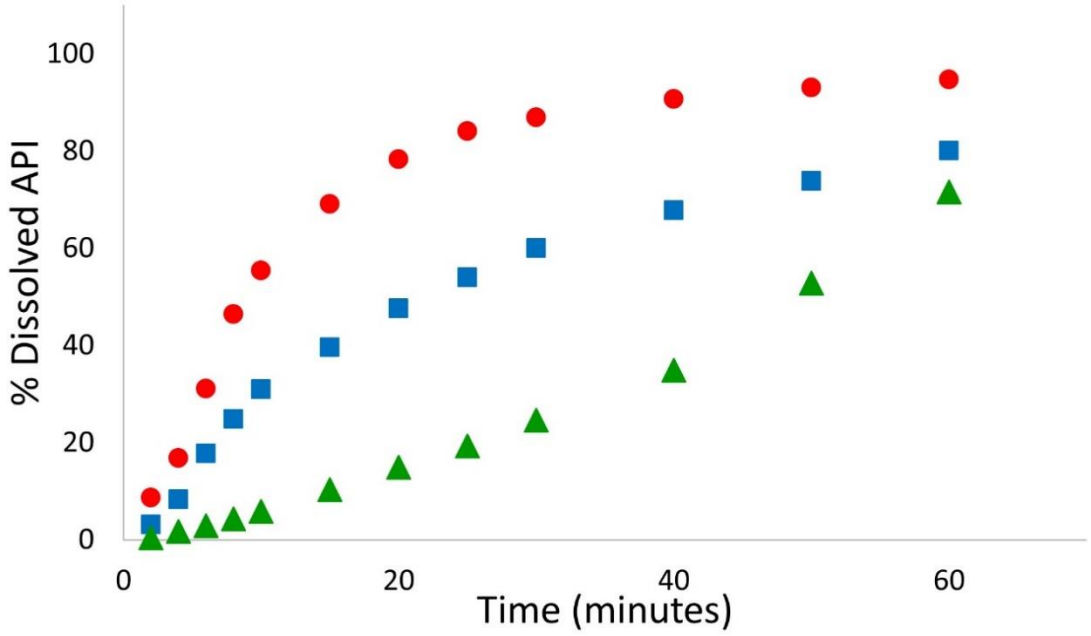

Figure A2.4: Dissolution profiles of 4 mg (red circle), 20 mg (blue square) and 100 mg (green triangle) Ibu-nd powder in phosphate buffer pH 6.8 with 0.005% w/v Tween 20 at 16 mL/min in the FTA CE1 22.6 mm diameter cell.

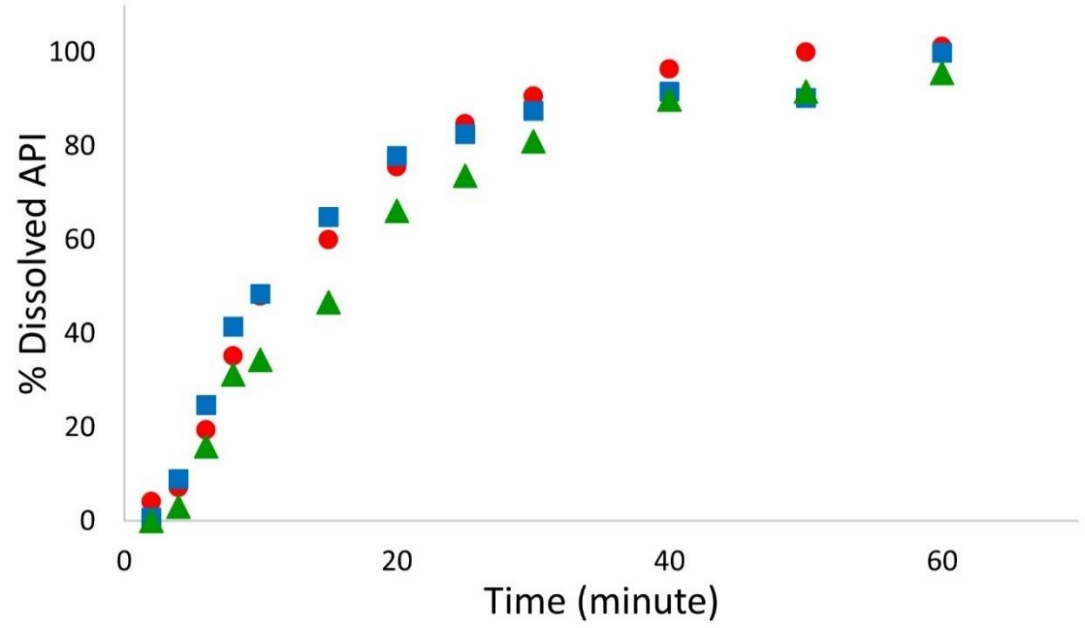

Figure A2.5: Dissolution profiles of 4 mg (red circle), 20 mg (blue square) and 100 mg (green triangle) Ibu-nd powder in phosphate buffer pH 6.8 with 0.05% w/v Tween 20 at FR 8 mL/min in the FTA CE1 22.6 mm diameter cell.

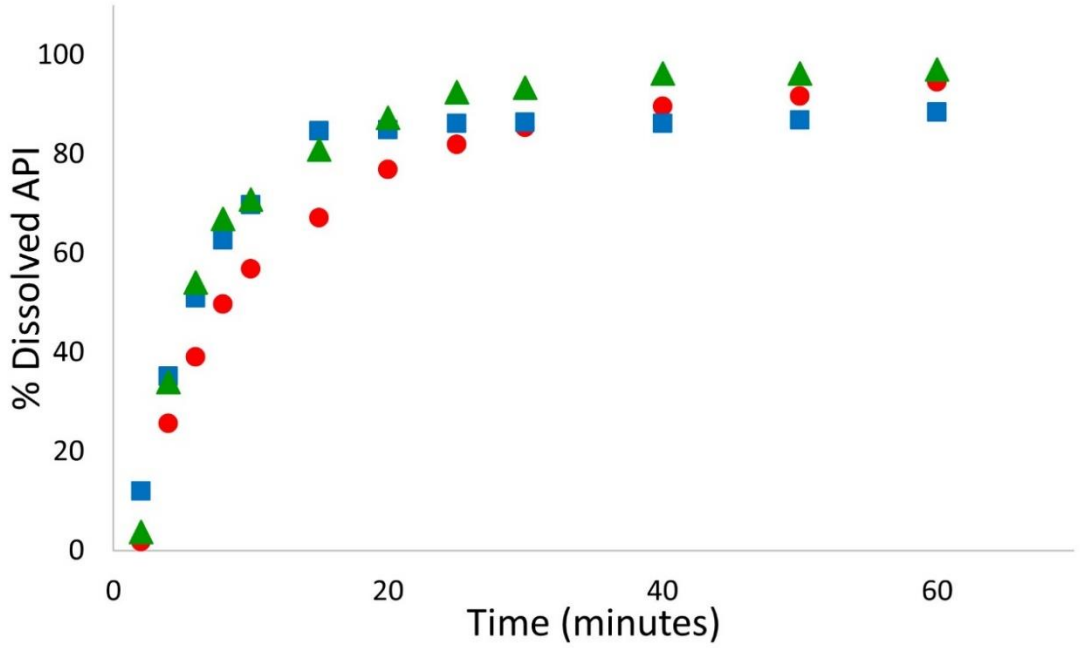

Figure A2.6: Dissolution profiles of 4 mg (red circle), 20 mg (blue square) and 100 mg (green triangle) Ibu-nd powder in phosphate buffer pH 6.8 with 0.05% w/v Tween 20 at 16 mL/min in the FTA CE1 22.6 mm diameter cell.

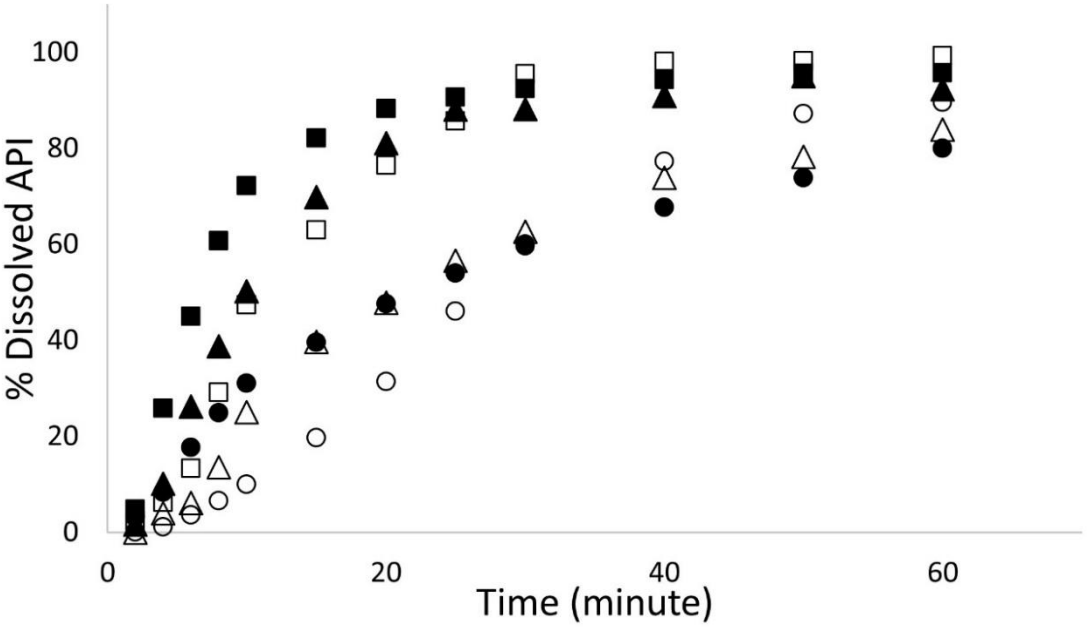

Figure A2.7: Dissolution profiles of Ibu-pl-S (squares, □), Ibu-nd-S (triangles, Δ) and Ibu-nd (circles, ○) in the FTA CE1, test cell 22.6 mm diameter at FR 8 (white) and 16 (black) mL/min. Medium: phosphate buffer with 0.005% Tween 20, pH 6.8.

Appendix 3

1. SGI Quantity & Dispersion code

```
%Clear all old graphics and the workspace
clear all; clf;

%Read .xlsx files
[files,path]=uigetfile('*.xlsx','multiselect','on');
num_of_files = length(files);
for i=1:num_of_files

data{i} = readtable(fullfile(path,files{i}));

end

% Particles diameter per minutes of the dissolution

len_data = length(data);                                    %Creates
variables.
Davg = [];
Median = [];
AR_avg = [];
solidity_avg = [];
Area_avg = [];
n = [];
Pr10 = [];
Pr90 = [];
Small = [];
Big = [];
Solid = [];


%Repetitive cycle for collecting information from the .xlsx files
for i=1:len_data                          %Number of files to open
from 1 to No.x
```

```
T_cell = data{1,i}(:,2);                    %Excel table; read all rows (:); column (2) diameter (mm).
T_double = table2array(T_cell);             %Changing matrix to numerical array.
names = strsplit(files{i},'_');             %Creates names of time points.
xvalue = str2num(cell2mat(names(1)));
x = xvalue.*ones(1,length(T_double));
average_diam = mean(T_double);              %Calculate the average diameter of the particles. Remove ";" to see the result in the comand window.
Davg(i) = average_diam;
SD = std (T_double);                        %Calculate the standard deviation of the diameter for each time point. Remove ";" to see the result in the comand window.
M = median (T_double);
Median(i) = M;
AR_cell = data{1,i}(:,6);                   %Excel table; read all rows (:); column (6)aspect ratio.
AR = table2array(AR_cell);                  %Changing matrix to numerical array.
average_ratio = mean(AR);                   %Calculate the average aspect ratio of the particles. Remove ";" to see the result in the comand window.
AR_avg(i) = average_ratio;
SD_R = std (AR);                            %Calculate the standard deviation of the diameter for each time point. Remove ";" to see the result in the comand window.
SD_AR(i) = SD_R;
solidity_cell = data{1,i}(:,10);            %Excel table; read all rows (:); column (6)aspect ratio.
solidity = table2array(solidity_cell);      %Changing matrix to numerical array.
solidity_mean = mean(solidity);             %Calculate the average aspect ratio of the particles. Remove ";" to see the result in the comand window.
solidity_avg(i) = solidity_mean;
SD_solidity = std (solidity);               %Calculate the standard deviation of the diameter for each time point. Remove ";" to see the result in the comand window.
```

```
45. SD_solidity(i) = SD_solidity;
46. Area_cell = data{1,i}(:,3);                 %Excel table; read all
    rows (:); column (3)area (mm).
47. Area = table2array(Area_cell);              %Changing matrix to
    numerical array.
48. average_area = mean(Area);                  %Calculate the average
    area of the particles. Remove ";" to see the result in the comand
    window.
49. Area_avg(i) = average_area;
50. SD_A = std (Area);                          %Calculate the standard
    deviation of the diameter for each time point. Remove ";" to see the
    result in the comand window.
51. SD_Area(i) = SD_A;
52. Pr10 = prctile(AR, 10);                     %Calculate the 10th
    percentile of the particle ARs. Remove ";" to see the result in the
    comand window.
53. Pr90 = prctile(AR, 90);                     %Calculate the 90th
    percentile of the particle ARs. Remove ";" to see the result in the
    comand window.
54. Small = [Small length(find(table2array(T_cell)<=0.106))];
55. Big = [Big length(find(table2array(T_cell)>0.4))];
56. Solid = [Solid length(find(table2array(solidity_cell)<=0.85))];
57. n(i) = numel(T_double);                     %Counts No. of detected
    particles.
58. n(n==0) = NaN;                              %Sign as NaN when the
    result is = 0. Like this the result is hidden from the graph.
59. scatter(x,T_double,'o','k')                 %Results in a graph with
    particles diam. dispercion.
60. hold on                                     %Holds previous results
    from the loop and apply the next on the same graph.

61. end

62. % axis limits                               %%Left axis
63. xlim ([0 70])
64. ylim([0 1])


65. % % Create legend
66. % xlabel("Time (min)");                     %x axis name
```

```
% ylabel("Particle diameter (mm)");           %y axis name
% title("Dissolution of 50 mg B100 in PB, FR 16 mL/min, large cell");
  %Graph title

% Create Average diameter plot
xavg = [2 4 6 8 10 15 20 25 30 40 50 60];     %x axis lables. Change
  them if different or delete if less then 15. The number of positions
  must match the number of files/avg. diam.
scatter(xavg,Davg,'g','*')                    %Plot average diameter
  on the graph above.
hold on
% a = errorbar(xavg,solidity_avg,SD_solidity);
% set (a,'Color','b','Marker','^','linestyle','-')          %Set
  graphic markers, size, shape and colour.
% ylim ([0 1])
% hold on

yyaxis right                                  %Creates a right axis on
  the graph above.

s = plot(xavg,n);                             %Plot number of detected
  paticles in log scale.
set (s,'Color','r','Marker','.','MarkerSize',48,'linestyle','-')
  %Set graphic markers, size, shape and colour.
set(gca,'yscale','log','yColor','r','ylim', [1E0 1E5])
  %Set scale type, colour, limits.


%ylabel ("No. Particles")                     %y axis name


% %Creates a graph of the aspect ratio and the particle area.
% %Shows average surface area and aspect ratio of particles in a
  single
% %timepoin of the test.
%
% f2 = figure;
% xavg = [2 4 6 8 10 15 20 25 30 40 50 60 80 100 120];        %x axis
  lables. Change them if different or delete if less then 15. The number
  of positions must match the number of files/avg. diam.
```

```
% a = errorbar(xavg,Area_avg,SD_Area)
% set (a,'Color','k','Marker','*','linestyle','-')            %Set graphic markers, size, shape and colour.
% ylim ([0 1])
% hold on
%
% % Create legend
% xlabel("Time (min)");                                        %x axis name
% ylabel("Particle area (mm)");                                %y axis name
% title("Ibuprofen hexane 20mg in PBT 0.005%, pH 6.8, flow rate 16ml/min");  %Graph title
%
%
% yyaxis right
%Creates a right axis on the graph above.
      %
      % b = errorbar(xavg,AR_avg,SD_AR)
      % set (b,'Color','b','Marker','o','linestyle','-')
%Set graphic markers, size, shape and colour.
      % set(gca,'yColor',[0,0,1],'ylim', [0 1], 'xlim', [0 130])
%Set scale type, colour, limits.
      % ylabel("Particle aspect ratio")
%y axis name


      %Creates a graph of the number of particles above/below certain size.
      %Detects particles with pre-defined limits. If one looks for agglomerates,
      %distribution or else.

      % f3=figure;
      % xavg = [2 4 6 8 10 15 20 25 30 40 50 60 80 100 120];      %x axis lables. Change them if different or delete if less then 15. The number of positions must match the number of files/avg. diam.
      % bar (xavg,n)
%plot all detected particles
      % hold on
```

```
112.      % bar (xavg,Small)
   %plot particles smaller than 106 um
113.      % hold on
114.      % bar (xavg,Big)
   %plot particles graeter than 300 um
115.      % hold on
116.      %
117.      % % Create legend
118.      % xlabel("Time (min)");                                    %x
   axis name
119.      % ylabel("Number of particles");                           %y
   axis name
120.      % title("Ibuprofen 250mg in PBT 0.005%, pH 6.8, 50 prm");
   %Graph title
121.      % legend('particles','small','big');
   %legend titles
122.      %
123.      %
124.      % %Creates a histogram of the number of particles above certain
   size and solidity below certain value.
125.      % %Detects particles above the limit and solidity below the
   limit. If both
126.      % %apear in the same time point - check the video for
   agglomerates.
127.      %
128.      % f4=figure;
129.      % xavg = [2 4 6 8 10 15 20 25 30 40 50 60 80 100 120];      %x
   axis lables. Change them if different or delete if less then 15. The
   number of positions must match the number of files/avg. diam.
130.      % bar (xavg,n)
   %plot all detected particles
131.      % hold on
132.      % bar (xavg,Solid,'FaceColor','[0.4940 0.1840 0.5560]')
   %plot particles smaller than 106 um
133.      % hold on
134.      % bar (xavg,Big,'FaceColor','c')
   %plot particles graeter than 300 um
135.      % hold on
136.      % % Create legend
```

```
137.      % xlabel("Time (min)");                                    %x
   axis name
138.      % ylabel("Number of particles detection/Size/Solidity");    %y
   axis name
139.      % title("Ibuprofen 250mg in PBT 0.005%, pH 6.8, 50 prm");
   %Graph title
140.      % legend('particles','solidity','big');
141.      %legend titles
```

2. AIM code

```
%Clear all old graphics and the workspace
clear all; clf;

%Read .xlsx files
[files,path]=uigetfile('*.xlsx','multiselect','on');
num_of_files = length(files);


data = readtable(fullfile(path,files));


%Repetitive cycle for collecting information from the .xlsx files
PrD75 = [];
PrD80 = [];
PrD90 = [];
PrS75 = [];
PrS30 = [];
PrS10 = [];
Avg = [];
Fp = [];

Time_cell = data(:,1);                                  %Excel
   table; read all rows (:); column (1) time (s).
Diameter_cell = data(:,2);                              %Excel
   table; read all rows (:); column (2) diameter (mm).
Solidity_cell = data(:,10);                             %Excel
   table; read all rows (:); column (10)solidity.
Time = table2array(Time_cell);
Diameter = table2array(Diameter_cell);
Avg = mean(Diameter);
PrD75 = prctile(Diameter, 75);
PrD80 = prctile(Diameter, 80);                          %PrDn is n-
   th Percentil of the diameter.
PrD90 = prctile(Diameter, 90);
Solidity = table2array(Solidity_cell);                  %Changing
   matrix to numerical array.
```

```
PrS75 = prctile(Solidity, 75);
PrS30 = prctile(Solidity, 30);                              %PrSn is n-th Percentil of the solidity.
PrS10 = prctile(Solidity, 10);
%flag1 = (Solidity < 0.96) & (Diameter > Avg);              %flag 1 can be set to be based on exact value or percentil (choose between flag1 versions - uncomment)
%flag1 = (Solidity < 0.85) & (Diameter > 0.300);
flag1 = (Solidity < PrS75) & (Diameter > PrD75);
flag2 = zeros(size(flag1));                                 % criterion result based on having similar hits in adjacent frames
Fp = nnz(flag1==1);                                         % counts positive flags = numbers of detections that hit the criteria


%plot(Time(Diameter>0.3),Diameter(Diameter>0.3),'o')      % plots only diameters > 0.3
plot(Time(Diameter>PrD75),Diameter(Diameter>PrD75),'o','Color','b','MarkerSize',7)      % plots only diameters > Pr80
hold on
plot(Time,Diameter,'.','Color','k', 'MarkerSize',10)
% plots all particles
hold on
plot(Time(Solidity<PrS75),Solidity(Solidity<PrS75),'v','Color','r')
% plots only solidity < PrS10
hold on
%plot(Time,Solidity,'.')                                    % plots all solidity values
hold on
scatter(Time,flag1,'p')
%set (f,'Color',[0.47,0.67,0.19])
xlim ([0 15])
ylim([0 1])
grid on
xlabel("Time (s)",'Fontsize',28);
ylabel("Diameter (mm)/Solidity",'Fontsize',28);
%title("Unprocessed 20mg in PB 0.005%, flow rate 16ml/min, 40min")
```

3. Image re-sizing code

```
Video = VideoReader('0_2023-04-03-132517-0000.avi')
numFrames = Video.NumberOfFrames;
n=numFrames;
for i = 1:n
frameOGSize = read(Video,i);
frameRightSize = imresize(frameOGSize, [225 225]);
imwrite(frameRightSize,['C:\Users\tasevaa\OneDrive - Trinity College
Dublin\Matlab\resizedImages\N200\Small cell, FR 16, PB 0%\0 min\'
int2str(i) '_frame0', '.jpg']);
end
```